Investigation of the pressure dependency of phase equilibria in colloidal model systems

Inaugural-Dissertation
zur
Erlangung des Doktorgrades der
Mathematisch-Naturwissenschaftlichen Fakultät
der Heinrich-Heine-Universität Düsseldorf

vorgelegt von

Karolina Tomczyk

aus Zgierz

May 2011

Aus dem Institut für
der Heinrich-Heine-Universität Düsseldorf

Gedruckt mit der Genehmigung der
Mathematisch-Naturwissenschaftlichen Fakultät der
Heinrich-Heine-Universität Düsseldorf

Referent: Prof. Dr. J. K. G. Dhont
Koreferent: Prof. Dr. S. U. Egelhaaf
Tag der mündlichen Prüfung: 29.06.2011

Summary

In this thesis the experimental studies of pressure jumps effect on several systems, representing a cross-section of soft matter materials. The phase behaviour of colloidal dispersions and polymeric micellar solutions using temperature and pressure as variables are presented in the first part. The second part addresses the correlation between temperature dependency of polymer viscosity and the diffusion time of a nanoscopic probe dissolved in this polymer.

As the first subject-matter, the interplay between percolation and phase separation effect appearing in an adhesive hard sphere (AHS) system, represented by octadecyl coated silica particles dissolved in toluene, is discussed. The transitions to the percolated and the biphasic states are obtained and they are in agreement with theoretical predictions. For concentrations higher than around 12-14vol%, the increase of the forward scattering intensity is found to be governed by the proximity of the spinodal line. But it is the percolation effect that controls the time scale at which the forward scattering intensity increases. For lower concentrations two approaches to determine spinodal line were proposed. Depending on the way of spinodal determination the system is expected to undergo phase separation either through nucleation or spinodal decomposition process. In the first scenario the sample starts to reveal the non-ergodic behaviour while forming nuclei (the denser phase), and the spinodal lies below the percolation line in the phase diagram. In the latter scenario the spinodal is expected to lie between binodal and percolation lines, and while system is decomposing, the sample volume spanning network is formed, which gives rise to non-ergodic behaviour attributed to the percolated state. This is the first study of competition between percolation and phase separation addressed with time-resolved measurement.

In the next chapter the temperature- and pressure-dependent behaviour of the water and water-DMF solutions of polymeric micelles composed of poly(ethylene-*co*-propylene-*b*-(ethylene oxide)) (PEP-PEO) block copolymer is described. It is found that the micellar radius of gyration for the water solution decreases while approaching the lower critical solution temperature (LCST), which is obtained by increasing temperature and pressure. However, in water-DMF dispersion there is no change in micellar radius

until the phase separation sets in. In the first case applying pressure has similar effect as increasing temperature (although there is no simple linear *dP/dT* relation), and in the latter case it acts as lowering of temperature.

In the last part the temperature dependence of diffusion of rubrene in the poly(ethylene-*co*-propylene) (PEP) polymer melt is investigated by fluorescence correlation spectroscopy. Its correlation with temperature dependence of polymer viscosity is found. This is a proof that the changes in rubrene diffusion while varying temperature are solely due to temperature variation of PEP viscosity.

Zusammenfassung

Diese Arbeit befasst sich mit der experimentellen Untersuchung der Effekte von Drucksprüngen in verschiedenen Systemen aus Materialien die der weichen Materie zuzuordnen sind. Im ersten Teil werden Phasenübergängen Kolloidaler Dispersionen sowie Lösungen von Polymermizellen untersucht, wobei Temperatur und Druck als Kontrollparameter dienen. Im zweiten Teil werden Korrelationen zwischen temperaturabhängiger Viskosität von Polymerlschmelzen und der Diffusion darin suspendierter, nanoskopischer Testpartikel untersucht.

Die erste Teil der Untersuchung befasst sich mit dem Zusammenspiel zwischen Perkolation und Phasentrennung von adhäsiven harten Kugeln, hier repräsentiert durch Octadecyl-beschichtete, in Toluene gelöste Silica Partikel. Die gemessenen Übergänge in den perkolierten und im zweiphasigen Zustand sind in Übereinstimmung mit theoretischen Vorhersagen. Für Konzentrationen von mehr als 12-14vol% bestimmt die Entfernung zur Spinodalen die Zunahme der vorwärts gestreuten Intensität. Die Zeitskala der zeitlichen Zunahme wird durch den Perkolationseffekt bestimmt. Für geringere Konzentrationen wurden zwei unterschiedliche Wege zur Bestimmung der Spinodalen vorgeschlagen. Je nach Methode der Herleitung ist eine Phasentrennung durch Keimbildung oder spinodale Entmischung zu erwarten. Im ersten Fall wird das System bei der Bildung von Keimen der dichteren Phase nicht-ergodisch, und die Spinodale befindet sich im Phasendiagramm unter der Perkolationslinie. Im Gegensatz dazu liegt die Spinodale im zweiten Fall zwischen der Binodalen und der Perkolationslinie, und bei der Phasentrennung bildet sich ein das Systemvolumen übergreifendes Netzwerk, welches die Nichtergodizität des perkolierten Zustands verursacht.

Im nächsten Kapitel wird das Temperatur- und Druckabhängige Verhalten von Lösungen aus Poly(Ethylen-*co*-Propylen-*b*-(Ethylen Oxid)) (PEP-PEO) Block-Copolymeren in Wasser und Wasser-DMF Mischungen beschrieben. Bei Annäherung an die untere kritische Lösungstemperatur durch Erhöhung von Druck und Temperatur wird im Fall der wässrigen Lösung eine Abnahme des Gyrationsradius der Mizellen beobachtet. Dahingegen ist der Gyrationsradius der Mizellen in Wasser-DMF Dispersionen unverändert bis zum Einsetzen der Phasentrennung. Im ersten Fall ist der

Effekt einer Druckerhöhung ähnlich dem einer Temperaturerhöhung (obwohl es keine einfache *dP/dT*-Relation gilt), während im zweiten Fall die Druckerhöhung einer Verringerung der Temperatur ähnlich ist.

Im letzten Teil der Arbeit wird mittels Fluoreszenzkorrelations-spektroskopie die Temperaturabhängigkeit der Diffusion von Rubrene in Poly(Ethylen-*co*-Propylen) (PEP) Polymerschmelzen untersucht. Es zeigt sich eine Korrelation der Diffusion mit der Polymerviskosität. Dadurch wird belegt, dass Änderungen in der Diffusion von Rubrene bei Temperaturänderung allein durch Variation der Viskosität von PEP mit der Temperatur zustande kommen.

Contents

1. Introduction

The soft matter systems are extensively studied since the beginning of the 19th century. Soft matter is a general term describing a very large class of materials whose common feature is that they are composed of particles with typical sizes between 1nm and 1μm dispersed in a solvent whose molecules are much smaller in size, among which the most important categories are colloids, polymers and amphiphilic systems [1]. In this thesis, studies of systems representing the two first groups will be described. In the last two decades, with the evolution of soft condensed matter physics the manipulation of materials properties has emerged as a subject of scientific and technological importance [2]. The final goal is the rational design of materials with desired properties for particular applications.

Colloids are inorganic particles of a size much bigger than the size of solvent molecule (about 1nm), which thus can be considered as continuum, but still small enough to exhibit Brownian motion (tens of microns) [3]. The term "colloid" comes from the Greek words *κόλλα* (glue) and *είδος* (kind). Because colloidal particles exhibit thermal motion, they can be described quantitatively using classical statistical mechanics [4,[5]. The interaction potential between molecules in colloidal dispersion can be tuned from long-ranged repulsive to very short-ranged attractive in many ways: by covering colloidal particle surface with polymer chains [6] or charged groups: by external means like changing temperature, application of pressure, adding or removing salt from the solvent, changing refractive index of the solvent to modify the strength of van der Waals interactions; or by adding free polymer to the solvent to enhance depletion interactions [7]. These possibilities of modifying interactions between mesoscopic particles give rise to an unprecedented richness in phase behaviour [8]. The ability to tune interactions and detect on experimentally easy accessible time- and length scales make colloidal dispersions ideal working horses for fundamental studies. On the other hand the importance of studying colloidal dispersions comes from their presence in our everyday experience, as for example: paints, ink, glue, milk, or in a wider sense blood and the cytoplasm within cell also belong to this class of systems. Their study is of great industrial, biological and medical relevance.

Polymers are long, chain molecules, which are built from a repeat unit, called a monomer, bound together by covalent bonds. The polymer architecture can be linear, star-shaped, H-shaped, bottle-brush like, etc. [1]. Many of their properties can be tailored by the use of different monomers in the polymerization process or by variation of polymer architecture. Even more interesting are block copolymers, which self-assemble into supramolecular structures called micelles, while dispersing in a selective solvent for one block [9]. Depending on the block copolymer composition, the micelles can also have different architecture. The softness of micelles and therefore their properties and phase behaviour depends on the structure of micelle, i.e. the relative size of the corona to the core [2]. This has the advantage of micelles tunability, which can be obtained by variation of temperature, concentration, pH strength, amount of added salt or choice of the solvent. Tuning the core/corona ratio the character of the system can be changed from polymeric, which is assigned to the softer corona, to colloidal, which is typically attributed to the hard core [2].

One control parameter has not been mentioned so far, namely the pressure. In almost all studies it is taken to be the ambient pressure. Although there are many ways how pressure could influence the phase behaviour of soft matter systems, it has not been a popular tool, mainly because of the experimental difficulties that are involved doing pressure experiments. First and foremost it is the mechanical stability of the pressure cell that complicates observations, e.g. because thick observation windows need to be used.

In most cases pressure will have exactly the same effect as temperature. The solvent quality of polymers, for example, can be equally well tuned by temperature and pressure. Often a pressure-temperature relation can be found [17]. The reason why pressure could be helpful and preferable above temperature as control parameter is that it can be applied almost instantenously and equilibration of the full sample takes place within fractions of seconds. Temperature changes, on the other hand, take much longer to propagate and homogenously distribute. Thus, when for example the time dependence of processes is investigated, pressure would be the tunable parameter of choice.

In the first and major part of this thesis the temperature- and pressure-dependent phase behaviour of two types of soft matter systems is studied: a colloidal dispersion and polymeric micelles.

In chapter 2 the experimentally obtained phase diagram of colloid dispersions of adhesive hard spheres (AHS) is presented. Octadecyl coated silica particles in toluene are used, as toluene is a marginal solvent for the grafted polymer and passage from hard sphere to sticky behaviour can be induced by variation of temperature and/or pressure. AHS systems reveal complex phase behaviour with gas-liquid phase separation and percolation [10-[17], which intersects the coexistence line. This and similar systems have obtained considerable attention [19,[27,[29] because there are two competing mechanisms at hand. The system can phase separate at sufficiently high attraction between particles or it can form a percolated network and gel, thus preventing phase separation towards the state of lowest energy. The use of pressure is the right tool to characterize this competition as it allows overcoming phase boundaries quickly, much faster than through a temperature variation. Since phase transitions caused by application of pressure correspond linearly to lowering of temperature, pressure can be used as a fast and reliable way to change the interactions and study kinetics. As is discussed in chapter 2, for concentrations below the intersection of binodal and percolation lines two approaches of spinodal determination are proposed and depending on it two scenarios of phase separation processes are described. In the first one during demixing through formation of nuclei (the denser phase), the sample starts to reveal a non-ergodic behaviour, and the spinodal lies below the percolation line in the phase diagram. On the other hand, in the latter scenario the spinodal is expected to lie between binodal and percolation lines, which means that while the system is decomposing, a sample-volume spanning network is formed, which gives rise to non-ergodic behaviour attributed to the percolated state. For higher concentrations only the first approach to determine the spinodal temperature was used. In this case it was found that the observed increase of the forward scattering intensity for higher pressures is governed by the proximity to the spinodal line and it is due to the evolution of a critical structure which was proved to follow a mean field type of scattering behaviour [17].

Chapter 3 contains an experimental study on the temperature- and pressure-dependent behaviour of polymeric micelles composed of poly(ethylene-*co*-propylene-*b*-(ethylene oxide)) (PEP-PEO) block copolymer in water and water-DMF solutions. The interest here is the comparison of influence of pressure on micellar radius of gyration for these two solutions and determination of the form factor from the single particle study before going into more complex case of more concentrated solution, and also to study later phase kinetics of soft spheres. The temperature- and pressure-dependent behaviour of these polymeric micelles is governed mainly by the PEO response to changes in solvent quality. That is the reason why the highly asymmetric block copolymer with majority of PEO was chosen. Pressure was used as a variable in this experiment because of its short application time. It is found that while approaching the lower critical solution temperature (LCST), which is obtained by increasing temperature and pressure, the decrease in micellar radius of gyration is observed for the water solution. However, in water-DMF dispersion there is no change in micellar radius until the phase separation sets in. In the first case applying pressure has a similar effect as increasing temperature (although there is no simple linear dP/dT relation), and in the latter case it acts as lowering of temperature. For the PEP-PEO micelles in water-DMF solution the temperature ranges, in which the system is stable, meta-stable and unstable at ambient pressure conditions, and the time required for the system to phase separate after lowering its temperature is also studied.

The division into first and second part is made because in the second part of this thesis no temperature- and pressure-induced phase behaviour is studied. Here the temperature dependence of diffusion of rubrene in solution of poly(ethylene-*co*-propylene) (PEP) polymer is studied by fluorescence correlation spectroscopy. Its correlation with the temperature dependence of polymer viscosity is found, which proves that the changes in rubrene diffusion while varying temperature are solely due to temperature variation of PEP viscosity.

PART I

2. Phase diagram of an adhesive hard sphere (AHS) system and the interplay between demixing and percolation effects

2.1. Introduction

The phase behaviour of the polydisperse adhesive hard sphere (AHS) system, consisting of octadecyl grafted silica particles in toluene, will be presented in this part.

AHS systems [10[17,[26,[27,[29] are known to display a complex phase behavior as they may exhibit a gas-liquid phase separation and also a percolation or gel line depending on concentration and on temperature or pressure. Well known systems that show this kind of behaviour are highly concentrated hard spheres with added depletion interactions [18], biological systems like globular protein lysozyme [19] or network of rods [20]. In the phase behaviour of the system of sticky hard colloidal spheres phase separation competes with arrested states like gels or glasses [21] and in its phase diagram the percolation line intersects the coexistence line.

Here, the dispersion of silica particles grafted with octadecyl chains in toluene at different volume fractions was used because its phase behaviour can be easily tuned varying temperature and/or pressure. The molecular background of this interaction was found by Roke *et al.* [22,[23]. Firstly, while lowering temperature the system can undergo a phase transition into two fluid phases – a less dense gas and a more concentrated liquid. Secondly, the system can percolate when colloidal particles suspended in a liquid medium connect to each other and tend to aggregate into amorphous macroscopic structures, and then eventually, they built a network spanning the whole sample volume. Depending on the aggregation mechanism, gel formation can occur even at very low volume fractions. Due to the small (submicron) size, colloidal particles do not sediment, but undergo Brownian motion, and the thermal energy overcomes gravitational forces. As they move randomly, collisions of particles are inevitable. In presence of attractive inter-particle interactions, such as due to long-range van der Waals or hydrophobic forces, particles would stick together and aggregate to bigger clusters. Such a suspension would be unstable and all particles would sediment down with time. In case of lyophobic colloids, like in- and organic particles (such as titanium oxide or polystyrene), which are thermodynamically unstable, particles have to be stabilized by repulsive interactions in order to obtain a stable suspension. There are two main mechanisms to avoid aggregation: charge- and steric stabilization. The first one is based on using charged particles, which will repel each other due to the Coulomb interactions. The latter one is used in the investigated system. It is based on adsorbing polymers at the particle surface. Polymers form a "hairy" layer around a particle and repel other "hairy" particles because a penetration of the polymer layers constrains the number of possible polymer configurations. This leads to a rise of the entropy and therefore to a repulsion of the particles. However, in a moderate solvent, lowering temperature yields very strong attraction with a range much smaller than a typical colloidal size.

The system of silica spheres grafted with octadecyl chains was used also because it can be described theoretically using the Baxter model [24], which is based on the Percus-Yevick approximation of hard spheres with a square well attractive potential (sketched schematically in Fig.2.1.a) with the infinitesimal width and infinite depth which is superimposed on a hard core repulsion. Taking this limit makes the second virial coefficient remaining finite. This model maps the interactions between colloidal particles as long as the interaction range is small compared to the particle size. The pair-interaction potential between colloidal particles has the form:

$$V_B(r) = \lim_{\Delta \to 0} \begin{cases} \infty & r<2R, \\ k_B T \ln\left[12\tau_B\left(\dfrac{\Delta}{2R+\Delta}\right)\right] \text{ for } & 2R \le r \le 2R+\Delta, \\ 0 & r>2R+\Delta, \end{cases} \qquad \text{(Eq.2.1.)}$$

where R is the hard core radius of the colloidal particle, Δ is the length of the grafted polymer chains and simultaneously the width of the square well interaction potential, τ_B is the stickiness parameter, often referred to a dimensionless quasitemperature. The stickiness parameter describes the change from hard sphere behaviour (large τ_B) to sticky behaviour (small τ_B) and is a function of both, temperature and pressure. For small values of Δ, the scattering behaviour depends only on the stickiness parameter. The stickiness parameter is related to the real temperature and to the particle size (R and Δ) via:

$$\frac{1}{\tau_B} = \frac{12\Delta}{2R+\Delta} \exp\left[L\left(\frac{\Theta(P)}{T} - 1 \right) \right], \qquad \text{(Eq.2.2.)}$$

which was obtained using the model from Flory-Krigbaum. This model assumes that the depth of the square well potential depends linearly on the parameter L, which in turn depends on the overlap volume of the two spheres and the difference between the Θ-temperature and temperature T. The Θ-temperature in this model is a measure of the enthalpic and entropic interactions between solute and solvent and is assumed in first approximation to vary linearly with pressure according to:

$$\Theta(P) = \Theta_0 + \frac{d\Theta}{dP}\left(P - P_0\right), \qquad \text{(Eq.2.3.)}$$

where the term $d\Theta/dP$=const and it is proportional to the compressibility.

The other parameter, apart from the stickiness parameter, that needs to be taken into account in order to make the link to the experiments is the polydispersity, for which a numerical algorithm for the structure factor within the Percus-Yevick approximation was developed, called the Robertus model [25].

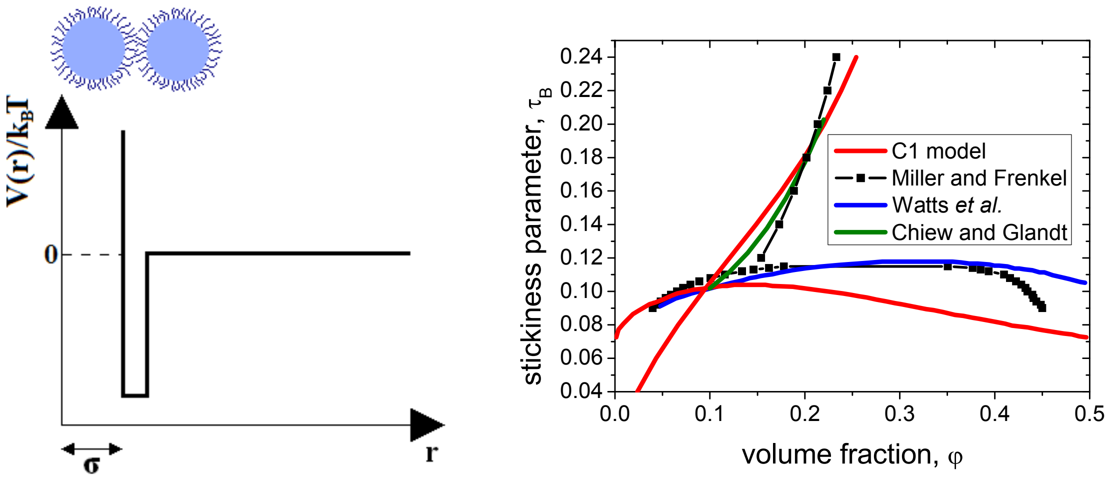

(a) (b)

Fig.2.1. (a) Schematic sketch of the pair interaction potential *V(r)* between two adhesive hard spheres with core diameter σ, and a square well width Δ and depth ε. (b) Theoretical phase diagram of an adhesive hard sphere system taken from literature [10,[16,[26].

As it was said before, the adhesive hard sphere system shows a complex phase behaviour, which was obtained not only experimentally but also theoretically by Watts *et al.* [10], Miller and Frenkel [16] or Fantoni *et al.* [26], among others. Using Percus-Yevick approximation, Watts *et al.* [10] obtained the equation of state of AHS system from the energy equation and they found out that the resulting thermodynamic properties show typical van der Waals behaviour, though, the critical temperature and density values were considerably higher than the ones received from the compressibility equation. The results of Monte Carlo (MC) simulations done by Miller and Frenkel [16] shows better agreement with the energy route of Percus-Yevick theory than the compressibility results, at least as far as the phase coexistence curve is concerned. Fantoni *et al.* [26] used modified mean spherical approximation (mMSA), in which only the energy equation of state gives rise to a critical behaviour, and they assumed a relation among polydispersity in size and polydispersity in stickiness. This is marked as C1 (red line) in Fig.2.1.b. Eventually, they received the critical point for lower volume fraction than previous two works. The phase diagram of the AHS system from numerical calculations of mentioned above authors is given in figure 2.1.b. The coexistence line (in the language of the phase separation: the binodal line) is rather flat within the investigated volume fraction range. The theoretical predictions of the position of the critical point in the phase diagram are given in the table below.

Table 2.1. Theoretical estimations of the critical point.

φ_c	$\tau_{B,c}$	method	reference
0.32	0.1185	Percus-Yevick approximation (energy equation)	Watts *et al.* [10]
0.266	0.1133	Monte Carlo (MC) simulations	Miller and Frenkel [16]
0.14	0.1043	1st order correction of the modified mean spherical approximation (mMSA) – C1	Fantoni *et al.* [26]

Moreover, it is known theoretically [11] and it was confirmed by simulations and experiments [13,[14,[26,[27] that in AHS systems percolation occurs also beneath the liquid-liquid phase transition. The theoretically expected positions of the percolation threshold in the phase diagram are given in table 2.2.

Table 2.2. Theoretical estimations of the percolation threshold.

percolation threshold	method	reference
$\tau_{B,perc} = \dfrac{19\varphi^2 - 2\varphi + 1}{12\left(1-\varphi\right)^2}$	Percus-Yevick approximation	Chiew and Glandt [11]
$\varphi_{perc} = \dfrac{-10.09 + 182.4\tau_B + 606.9\tau_B^2 + 15.31\tau_B^3}{1 + 507.9\tau_B + 548.9\tau_B^2}\dfrac{\pi}{6}$	MC simulations	Miller and Frenkel [16]
$\varphi_{perc} = \dfrac{2\left(-3\tau_B^2 + \sqrt{3\tau_B^3\left(1 - 9\tau_B + 30\tau_B^2\right)}\right)}{1 - 12\tau_B + 30\tau_B^2}$	1st order correction of mMSA	Fantoni *et al.* [26]

It is an important issue to know the location in the phase diagram of the percolation and the coexistence lines and their intersection, as the main motivation of this work is to find a possible difference in scattering behaviour, while varying temperature and pressure, at different concentrations where different responses could be expected. On one hand, for the very low concentrations, while lowering temperature (applying pressure) the binodal line would be crossed first, and on the other hand, for higher concentrations, the percolation line would be approached first. This could be helpful to understand whether scattering behaviour is governed by which phenomenon. The physical interpretation of the region in the phase diagram between the spinodal and the percolation lines is under debate, since some authors [19,[21,[28-[30] claim that here the nucleation is hindered or frustrated, and in a sense the differentiation between percolation and nucleation is difficult to make experimentally.

The concept of the experiment is shown schematically in figure below. The arrows represent the direction in variation of temperature (obtained through application of pressure).

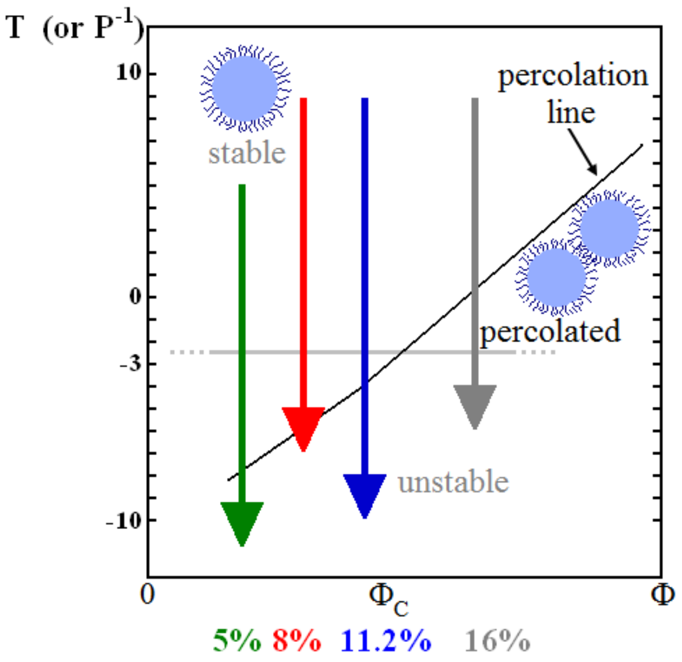

Fig.2.2. Schematic representation of the main concept of the experiment.

The time-dependent experiments, using scattering techniques: diffusive wave spectroscopy (DWS) and small-angle neutron scattering (SANS), were performed for the dispersion of octadecyl grafted silica in toluene dispersions at the volume fractions of φ=5%, 8%, 11.2% and 16%. The choice of these particular concentrations comes from the interest in interplay between phase separation and percolation effects. As the phase diagram of this system shows an intersection of the coexistence and the percolation line for the volume fraction of around 12%, it is important to investigate not only the temperature (pressure) dependent behaviour of the sample of this particular concentration but also samples of lower and higher volume fractions. It is crucial for the comparison of possible differences in the scattering behaviour while varying temperature (pressure) for both situations: when the binodal line is crossed first or the percolation. As pressurizing correspond linearly $\left(dP/dT = -77.5\ bar/K\right)$ to lowering temperature (which was found by Vavrin *et al.* [17]), pressure was used as a main variable in described experiments due to possibility of reaching desired points in phase space faster than while changing temperature, which enables to access the kinetics of phase separation or percolation. Firstly, using the diffusive-wave spectroscopy (DWS) it is possible to define the transition from ergodic to non-ergodic state, which is identified with crossing the percolation line. Secondly, from the turbidity (transmission) measurement the position of the coexistence (binodal) line is determined. Finally, for the 16% sample the small angle neutron scattering (SANS) was used to obtain the information about the spinodal line (the set of number densities and temperatures where the system becomes unstable), which is defined by: $d\Pi/d\varphi = 0$. The structure factor at zero wave-vector, *S(q=0)* is connected to thermodynamics of the system by:

$$\frac{1}{k_B T}\left(\frac{\partial \Pi}{\partial \varphi}\right)_T = \frac{1}{S(q=0)} \propto \frac{1}{I(q=0)} \qquad \text{(Eq.2.4.)}$$

(where Π is the osmotic pressure and k_B is the Boltzmann constant), and it diverges as the spinodal is approached. As the measureable physical quantity like forward scattering intensity *I(q=0)* is proportional to *S(q=0)*, the analysis of its divergence would give the spinodal line. This analysis can be easily done plotting inverse forward scattering intensity versus temperature or pressure, extrapolating it to zero would give then the values of spinodal temperature or pressure, respectively. The spinodal can be determined as well by introducing the critical scaling law. As it is well known in the physics of critical phenomena [31], the forward scattering intensity diverges upon approaching to the critical point by variation of temperature (or pressure) as:

$$I(q=0) \propto \varepsilon^{-\gamma}, \qquad \text{(Eq.2.5.)}$$

where γ is the critical exponent for the susceptibility, and the reduced variable, ε, can be expressed in both ways, as the reduced temperature $\frac{|T-T_c|}{T_c}$ or pressure $\frac{|P-P_c|}{P_c}$. The value of the critical exponent for the mean field type of behaviour is equal to -1. For the lower (than 16%) volume fraction of the investigated system both ways to determine the spinodal temperatures (or pressures) are unreliable due considerable uncertainty. The position of the spinodal line for samples of concentration 5%-11.2% was attributed to the conditions at which the peak in the time dependency of transmission and forward scattering intensity appears. The more detailed explanation of this approach will be given in subchapter 2.3.3.

2.2. Experimental Section

2.2.1. Materials

Silica core particles prepared according to Stöber *et al.* [32] with the composition of $(SiO_2)_6H_2O$ [33], and grafted with stearyl alcohol following a procedure described by van Helden *et al.* [34] to obtain octadecyl chains chemically bound onto the core surface were used in these experiments. As it was found by Kohlbrecher *et al.* [35], the silica particles contain in their cores the amount of 15.6% by volume of alkyl chains (remaining after either their synthesis or the beginning of the grafting procedure), which gives the density of 2.0g/ml and the scattering length density $\rho_{silica} = 2.4 \cdot 10^{10} cm^{-2}$, and they have the core of radius of 34.2nm, and 2.3nm thick shell composed of octadecane, which scattering length density is $-0.234 \cdot 10^{10} cm^{-2}$. All the samples of different volume fractions were prepared from two concentrated colloidal dispersions of the particles in: fully protonated and fully deuterated toluene. The scattering length densities of the solvent for each sample were: $\rho = 2.9 \cdot 10^{10} cm^{-2}$ for sample of volume fraction φ=5%, $\rho = 2.7 \cdot 10^{10} cm^{-2}$ for samples of 8% and 11.2%, and $\rho = 2.6 \cdot 10^{10} cm^{-2}$ for the sample of 16% volume fraction. These particular compositions were chosen in order to reduce multiple scattering, and in fact transmission of all samples was around 95%.

2.2.2. Experimental techniques and set-ups

Scattering experiments are widely used in characterizing the structure as well as determination of the dynamics of matter. In soft condensed matter, the most commonly used scattering techniques are X-ray, neutron and light scattering [36]. Measuring the scattered intensity can give the information of different properties. On the one hand, in static scattering experiment, the time averaged intensity obtained as a function of the scattered angle gives the insight into the structure as the information about: the radius of gyration, the form factor and the structure factor, can be extracted from it. The form factor describes the shape of an individual particle and its internal mass distribution, and the structure factor – the spatial correlations between the particles. On the other hand, in the dynamic scattering, the time dependent fluctuations of scattered intensity give the information about the motion of the particles, their dynamics.

In order to describe scattering experiments quantitatively, several assumptions and limitations have to be made [5]. First of all, the scattering process is supposed to be quasi-elastic, which means that the magnitude of the scattered wave-vector is equal to that of the incident wave-vector, and so the interaction of the radiation with the sample is such that the wavelength is not (sufficiently) affected. In other words, any absorption of the radiation by the matter and/or inelastic scattering with significant energy transfer are neglected. Moreover, the incident beam is not distorted by the medium. The incident beam is also supposed to be a monochromatic plane wave. Furthermore, the scattering centers in the medium are meant to be small compared to the wavelength of the scattered beam. And finally, the distance between the source of the radiation and the sample as well as the distance between scattering centers and the detector should be sufficiently large, which corresponds to the far-field (Fraunhofer) approximation.

As the small angle neutron scattering (SANS) and diffusive wave spectroscopy (DWS) were used in the experiment, these techniques will be described briefly below.

2.2.2.1. Small Angle Neutron Scattering (SANS)

The basic principles of neutron scattering are the same as for light scattering, which are described in chapter 3.2.2.1. The fundamental difference between these two is that neutrons are scattered at the nuclei of atoms whereas photons scatter due to the local fluctuations in the dielectric constant of the medium. Small angle neutron scattering has proven to be particularly fruitful technique because of its several unique properties. Firstly, neutrons interact weakly with matter, therefore problems with multiple scattering are less important. Secondly, in neutron scattering experiments it is possible to highlight selectively structural units of interest using contrast matching. In contrary to light scattering, the contrast variation can be achieved relatively easy by simple isotope exchange. Chemically identical isotopes can be mixed or replaced without affecting the sample characteristics, but by choosing their appropriate mixture the contrast between for example particles and solvent or between different parts of particles can be enhanced or diminished. In particular exchange of hydrogen and deuterium, due to the big difference in their bound coherent scattering lengths ($b_H = -3.74 \cdot 10^{-15} m$ for hydrogen and $b_D = 6.67 \cdot 10^{-15} m$ for deuterium), makes this technique an ideal tool to study systems in soft condensed matter. Additionally, SANS has an extended spatial resolution capability, roughly in the region of 1000 to 10Å.

The property obtained in SANS experiment is the macroscopic differential scattering cross-section, and it is given by:

$$\frac{d\Sigma}{d\Omega}(\vec{q}) = \frac{\langle b \rangle^2}{V_s} \sum_{j,k=1}^{N} \left\langle \exp\left(i\vec{q} \cdot \vec{r}_{jk}\right) \right\rangle + \frac{N}{V_s}\left(\left\langle b^2 \right\rangle - \langle b \rangle^2\right), \qquad \text{(Eq.2.6.)}$$

where the first ($\vec{q}$-dependent) term represents the coherent scattering part and carries information about structure of particles and their spatial arrangement. The second ($\vec{q}$-independent) term is the incoherent scattering and comes from scattering from single atoms which subsequently superimpose without interference. In SANS experiment this term represents a q-independent background. The macroscopic differential scattering cross-section is related to physical properties of the investigated system via [37]:

$$I(q) = \frac{d\Sigma}{d\Omega}(q) = c\frac{N_A}{M_w}\left(b - V\rho_0\right)^2 \left\langle f^2(q) \right\rangle S(q), \qquad \text{(Eq.2.7.)}$$

where $c = \frac{NM_w}{V_{tot} N_A}$ is the particle concentration (given in g/cm^3), with N being the number of particles in the illuminated volume, M_w – the molar mass, V_{tot} – the illuminated sample volume and N_A – the Avogadro number. Further, b is the bound coherent scattering length of the colloid particles, V – their volume, and ρ_0 is the scattering length density of the solvent. The size averaged squared form amplitude, $\left\langle f^2(q) \right\rangle$, commonly known as the form factor *P(q)*, is normalized to 1 for q=0. The static structure factor, *S(q)*, has been calculated according to Robertus *et al.* [25] and takes into account the inter-particle correlations. For sufficiently diluted solutions *S(q)*=1 for all q values.

All of the neutron scattering experiments were performed at the SANS-I device at the SINQ spallation source at the Paul Scherrer Insitute in Villigen, Switzerland [38].

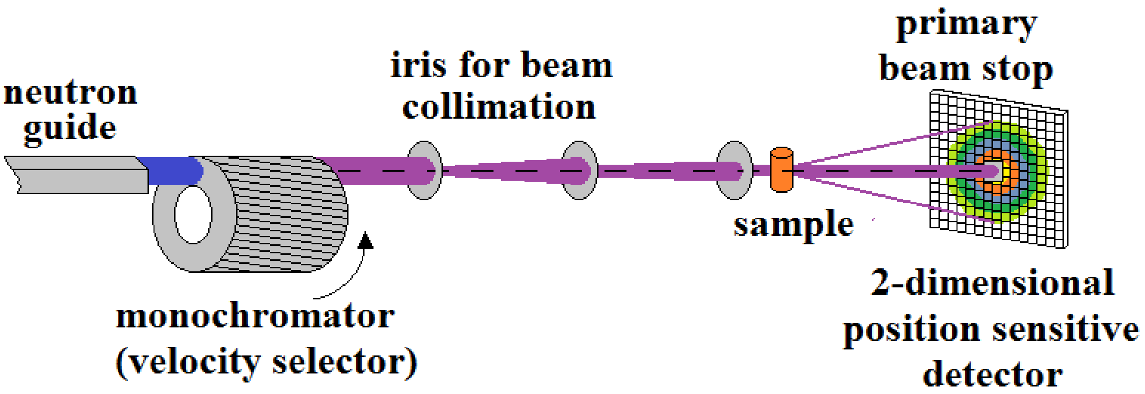

Fig.2.3. Scheme of the small angle neutron scattering (SANS) set-up.

The cold neutrons from a spallation source coming from a neutron guide pass a monochromator (a helical slot velocity selector), which selects the neutron wavelength in the range of 4.5Å<λ<40Å with a wavelength spread $\Delta\lambda/\lambda$ of about 0.1. Then the beam is collimated to the sample (which is situated in the pressure cell described elsewhere [39]) by a collimator of variable length between 1m and 18m. Scattered neutrons enter a vacuum tank in which a two-dimentional ^{3}He detector can be driven to distances between 1m and 20m. The detector is composed of a matrix of 128×128 detectors, each with a size of 7.5×7.5mm^2. The accessible q-range is $0.6\cdot10^{-3}$Å^{-1}<q<1.05Å^{-1}. The data analysis can be performed using BerSANS software package [40] which takes into account all necessary corrections due to background, transmission, sample thickness, etc. The pressure generator and thermostat were connected to the pressure cell in order to apply and keep constant pressure and temperature while running the measurement. The pressure generator was set in such way that it was automatically re-pumping the hydraulic oil into the cell when the actual pressure was at least 30bar off from the desired value.

2.2.2.2. Diffusive Wave Spectroscopy (DWS)

Diffusive wave spectroscopy [41] extends the dynamic light scattering (DLS) technique to turbid media, as it depends on high amount of scattering events experienced by photon passing through the sample (as it is schematically represented in figure 2.4.a). In contrary to single scattering experiments, such as classical static and dynamic light scattering techniques, the photon path is completely randomized in a case of multiple scattering. That is why DWS measurement is not q-dependent anymore and there are only two experimental geometries: backscattering and transmission. Here, the latter was used.

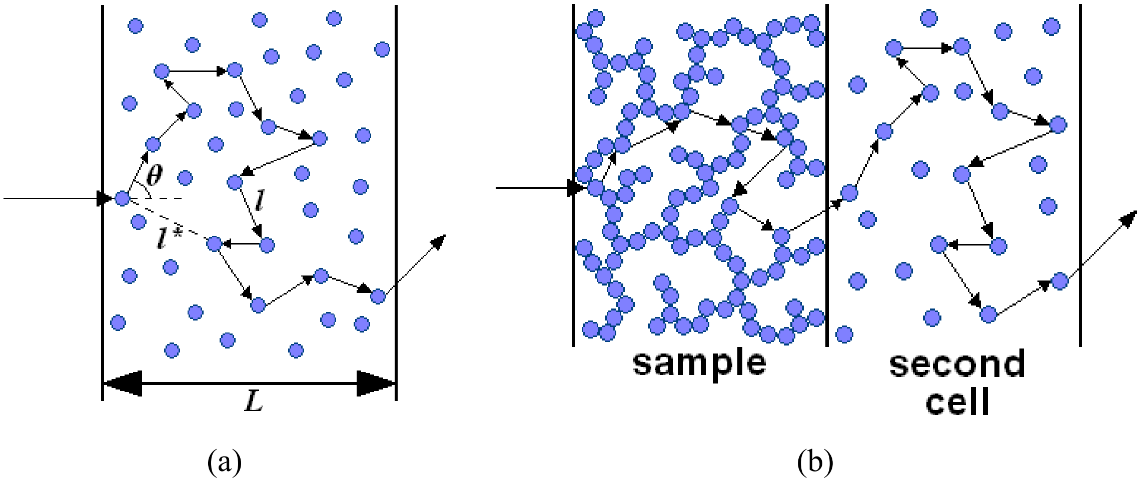

(a) (b)

Fig. 2.4. (a) Schematic representation of a photon path in the DWS measurement. L is the sample thickness, l – the scattering mean free path and l^* – the transport mean free path. (b) Schematic representation of a photon path in the double-cell technique.

In DWS, as well as in traditional DLS, the temporal intensity fluctuations of a single speckle spot of the scattered light are measured. In both techniques these fluctuations reflect the dynamics of the scattering medium and are characterized by their temporal autocorrelation function, which analysis provides a characteristic time-scale for the intensity fluctuations. The difference between both techniques is that the temporal scattered intensity fluctuations in traditional DLS reflects the differences in the path lengths, $\Delta\vec{r}$, between pairs of moving particles, whereas in DWS they come from changes in the relationship between all the phases of different pairs of light paths (each consisting of many scattering events), which changes while particles move. In traditional DLS the characteristic decay time of the correlation function is related to the dynamics of the medium in the length scale set by the inverse of the scattering wave-vector, q^{-1}. In other words, in order to obtain meaningful information about the dynamics of the medium from the characteristic time-scale of the intensity fluctuations, the knowledge of the length scale set by $1/q$ is required. This limits strictly the application of traditional DLS to single scattering case, which means that the mean free path l of a photon, defined as the average length between two scattering events, should be longer than the sample thickness ($l > L$). On the other hand, in DWS, as the light undergoes such a large number of intermediate scattering events, the diffusion approximation to describe propagation of light is used and therefore the scattering wave-vector has no relevance to the resultant correlation functions. Here, the transport mean free path l^*, which specifies the length scale at which a photon will loose any information about its initial direction, is the characteristic length scale for diffuse propagation of light.

Double-cell technique

In non-ergodic systems (for example solid-like samples such as glasses or gels) – unlike ergodic systems, where particles (and clusters) undergo free diffusion – the time average differs from ensemble average. In this case, when clusters connect to a space filling network, particles cannot escape from their position and do not explore the whole phase space anymore. This way their positions are correlated and the field correlation function does not decay to zero but decorrelates to a plateau. Moreover, as particles are trapped, each observed speckle represents the intensity fluctuation of an individual photon path through the particular network configuration of the system, and the time averaged scattered intensity differs from the ensemble averaged. Furthermore, as the non-fluctuating part of the intensity contributes only to the background, and all time averaged correlation functions decay to zero, they cannot be used to measure the plateau. In order to obtain an ensemble averaged correlation function, one has to make additional efforts, for example translating or rotating the sample slowly while taking measurements. Among others the double-cell technique seems to be the most elegant and simple. It was presented by Romer *et al.* [42] and Scheffold *et al.* [43]. The name comes from use of additional cell containing an ergodic turbid medium attached to the cell with an investigated sample, which is schematically shown in figure 2.4.b. At first laser beam goes through the investigated non-ergodic medium (which features a faster decay that stops at a certain plateau height) and then passes through the ergodic sample, which is chosen to have dynamics at least one order of magnitude slower comparing to the first one. The second cell induces then a full (ensemble) averaged decorrelation at higher lag times. It has been shown by Scheffold *et al.* [43] that in case of: independent scattering in both cells (which means no loop-like photon paths between both cells), weak absorption and $L \gg l^*$, the resulting correlation function $g_{2\,total}$ is given by a simple multiplication rule:

$$g_{2\,total} - 1 = \left(g_{2sample} - 1\right)\cdot\left(g_{2second\,cell} - 1\right). \qquad \text{(Eq.2.8.)}$$

Dividing the normalized to one total field correlation function, $g_{2\,total}$, by separately measured field correlation function of the second cell, $g_{2second\,cell}$, the real ensemble averaged field correlation function of the sample, $g_{2sample}$, remains.

The scheme and the picture of the set-up are shown in figure 2.5. Here, the pressure cell used in all SANS and DWS experiments can be seen.

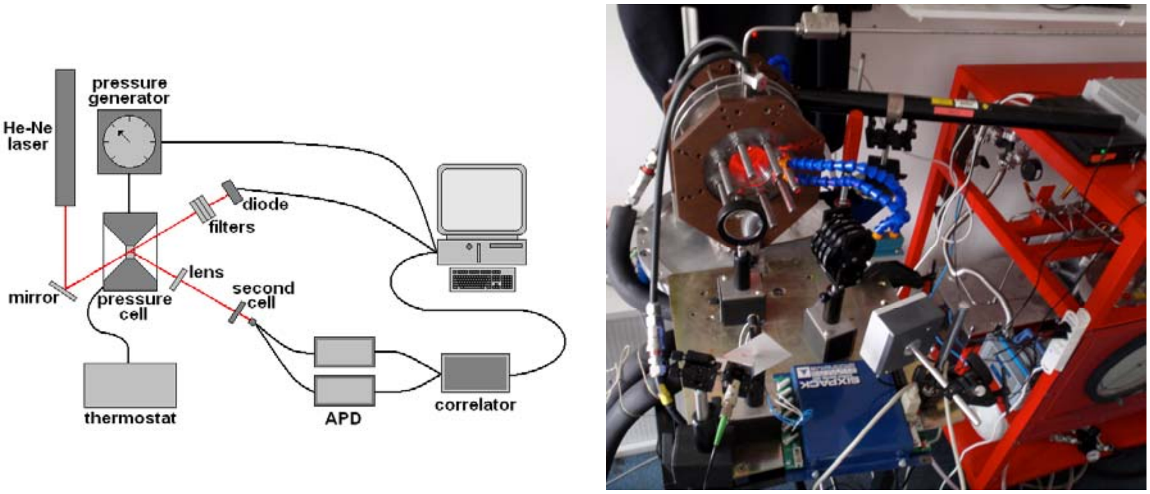

(a) (b)

Fig. 2.5. The set-up for DWS measurements: (a) scheme, (b) photo.

The light of wavelength λ=632.8nm emitted by the He-Ne laser (Melles Griot, 25-LHP-925-230, 17mW) hits the window of the pressure cell (where the pill containing the sample is placed) at a certain angle in order to reduce the reflected light. The scattered light, after passing a lens, which focuses the scattered light, goes through the rotational second cell, a piece of glass depolished by sandblasting rotated by a high resolution step motor (MAE HS200-2216-0100-AX08). Finally the scattered light is coupled with a collimator (Schäfter+Kirchhoff 60FC-0-M8-33) into a single mode fiber (Schäfter+Kirchhoff FSB-630-4), which the second mode fiber is connected to in the way that the light is splitted between them equally. Each fiber goes to the Avalanche Photo Diode (ADP, Perkin Elmer SPCM-AQR-13FC). Signals coming from both detectors are further cross correlated with an external USB correlator (Flex990EMd-12). The transmitted light after passing the density filters is collected by the photodiode.

2.3. Results

2.3.1. Determination of the percolation line

As it was said in subsection 2.2.2.2., using the double-cell DWS technique allows distinguishing the non-ergodic from the ergodic state. In figure 2.6.a the normalized raw data for the sample at volume fraction φ=11.2% and at the temperature T=2.7°C is presented with the correlation function of the second cell, which was measured separately by replacing the sample with a static scatterer such as piece of paper. In figure 2.6.b, on the other hand, there are shown the correlation functions of only the sample, which were calculated using Eq.2.8. As it can be easily seen, with increasing pressure, the measured correlation functions decay at larger lag times and eventually start building up a plateau, which is characteristic for non-ergodic behaviour. The decorrelation to zero, which is observed after applying lower pressures (in this case: up to 400bar) is a sign of ergodicity.

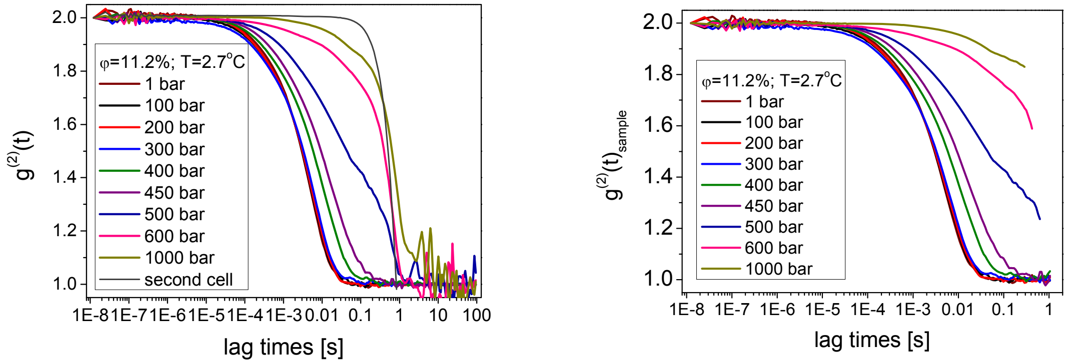

(a) (b)

Fig.2.6. (a) Normalized raw data of the two-cell DWS setup for the sample of a volume fraction of φ=11.2% at temperature 2.7°C; (b) the same data corrected for the decay of the second cell. With the increase of pressure, the correlation functions decay at larger lag times values and eventually they build up a plateau, which is a sign of a non-ergodic (gel) state.

In the performed measurements, the pressure was applied always from 1bar to the desired value and just in the moment of reaching it the measurement was started. The application of pressure itself was lasting from few seconds up to a few minutes (the higher the pressure value was set, the longer it took to reach it). Moreover, the measurements, which were lasting up to 200 minutes, were done in a so-called time slicing mode with the time interval of 2 minutes, which was set as a compromise between obtaining possibly the most detailed information about time-dependent processes in the sample and receiving the appropriate statistics of the scattered light in order to get trustworthy correlation functions. If there is any process lasting less than 2 minutes, there would not be a chance to resolve it because of the low intensity and wrong averaging reasons. After each measurement pressure was released and the new measurement was started only after at least half an hour. Within this time the sample equilibrated and came back to its previous stable state.

In figure below the exemplary correlation functions (already corrected for the decay of the second cell according to the Eq.2.8.) for the sample at volume fraction φ=11.2% and at the temperature T=2.7°C are shown for pressures: 450, 500 and 600bar. In each figure the correlation function of the sample measured at ambient pressure was added (the red curve) in order to see the increase in the decay times at higher pressures. In the first graph, for the pressure *P*=450bar (as well as for the lower pressures at this temperature), one can observe the decorrelation to zero in the whole time-frame of the measurement, which is a clear proof for ergodic behaviour. On the other hand, in the last graph, at pressure *P*=600bar, the plateau in the correlation function is built from the very first measurement, which means that after applying this (and higher) pressure at *T*=2.7°C, the system gets immediately non-ergodic. The interesting situation happens at *P*=500bar, where the plateau starts to build up at around 58th minute of the measurement, so the system at these conditions is at first ergodic, and then evolve with the time into the non-ergodic state.

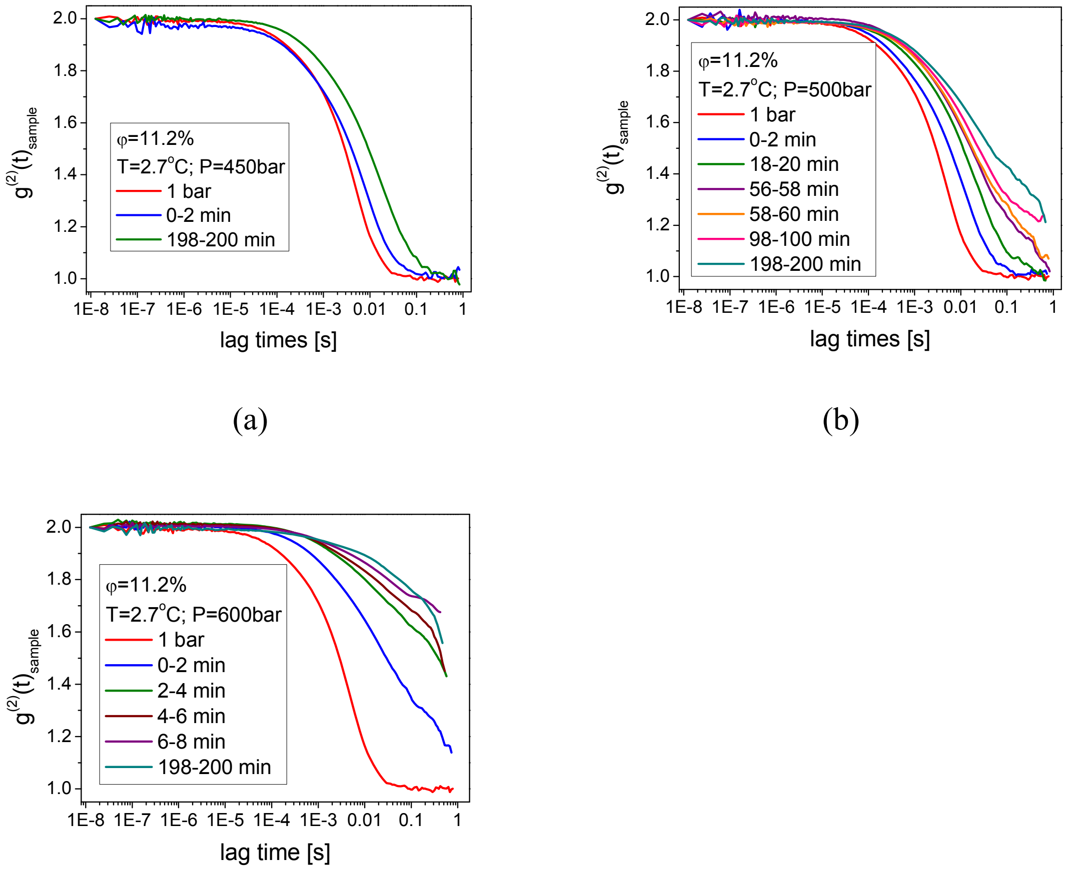

(a)

(b)

(c)

Fig.2.7. The examples of the correlation functions for the sample of a volume fraction of *φ*=11.2% at temperature 2.7°C at: (a) 450bar, (b) 500bar, and (c) 600bar.

For the investigated concentrations of the sample in the experimental time frame the passage from ergodic to non-ergodic state appears: for the φ=5% at 4°C between 650 and 800bar; for the φ=8% at 5°C between 700 and 750bar, and at 9°C – between 1050 and 1100bar; for φ=11.2% at 2.7°C at 500bar, and at 8°C – between 900 and 1000bar. These pressure values correspond (according to the *dP/dT* relation obtained by Vavrin *et al.* [17]) to the temperatures of: between -6°C and -4°C for φ=5%, between -5°C and -4°C for φ=8% and 11.2% samples.

2.3.2. Determination of the binodal line

From this light scattering experiment the information about the turbidity of the sample was obtained as well. The results of the measurements of the transmitted light are presented in figure 2.8. Here, the ergodic state is distinguished from the non-ergodic one by using filled and hollow symbols, respectively. As it can be clearly seen, applying pressure (which corresponds to the lowering of the temperature) makes the sample more turbid. The decrease of the transmission (the increase of the turbidity) is becoming more rapid after passing the binodal. This is shown in figures below (Fig.2.8.b,d,f,h,j), where the end transmission values are plotted versus pressure and temperature. The transmission values for the end of each measurement (for each applied pressure) are taken as the final states have to be taken to determine the binodal. Loci of intersection of two linear fits are indicated with arrows, which also point the values of the binodal pressure and temperature. Clearly, for the sample at small volume fractions of 5% and 8% the good agreement was obtained between the results of binodal pressures and temperatures from crossing of the linear fits and these predicted from the *dP/dT* relation. For the 5% sample values of binodal temperature $T_{binodal}$=-2.4°C and binodal pressure $P_{binodal}$=504bar received from intersection of two linear fits are very close to predicted values of $T_{binodal}$= -2.5°C and $P_{binodal}$=494bar. For the 8% sample values of binodal temperature -2.7°C (measurement at T=5°C) and -2.6°C (measurement at T=9°C) were obtained from intersection of two linear fits. Values of binodal pressure $P_{binodal}$=606bar (measurement at

T=5°C) and 894bar (measurement at *T*=9°C) are also very close to predicted values of 581bar and 891bar, respectively. The situation gets slightly worse for the 11.2% sample. The difference between the values obtained from the intersection of the linear fits and the values calculated from the *dP/dT* relation in determination of the binodal temperature is 0.7°C and around 50bar for the binodal pressures. As the same thermometer was used in all experiments, the possibility of getting bigger error in the temperature determination in only one case, can be excluded. However, the determination of dP/dT_{trans} , described by *R. Vavrin et al.* [17], gives the values of the binodal temperature with the error of 0.75°C, so the values obtained from linear fits are still in the agreement with these predicted from dP/dT_{trans} within its uncertainty.

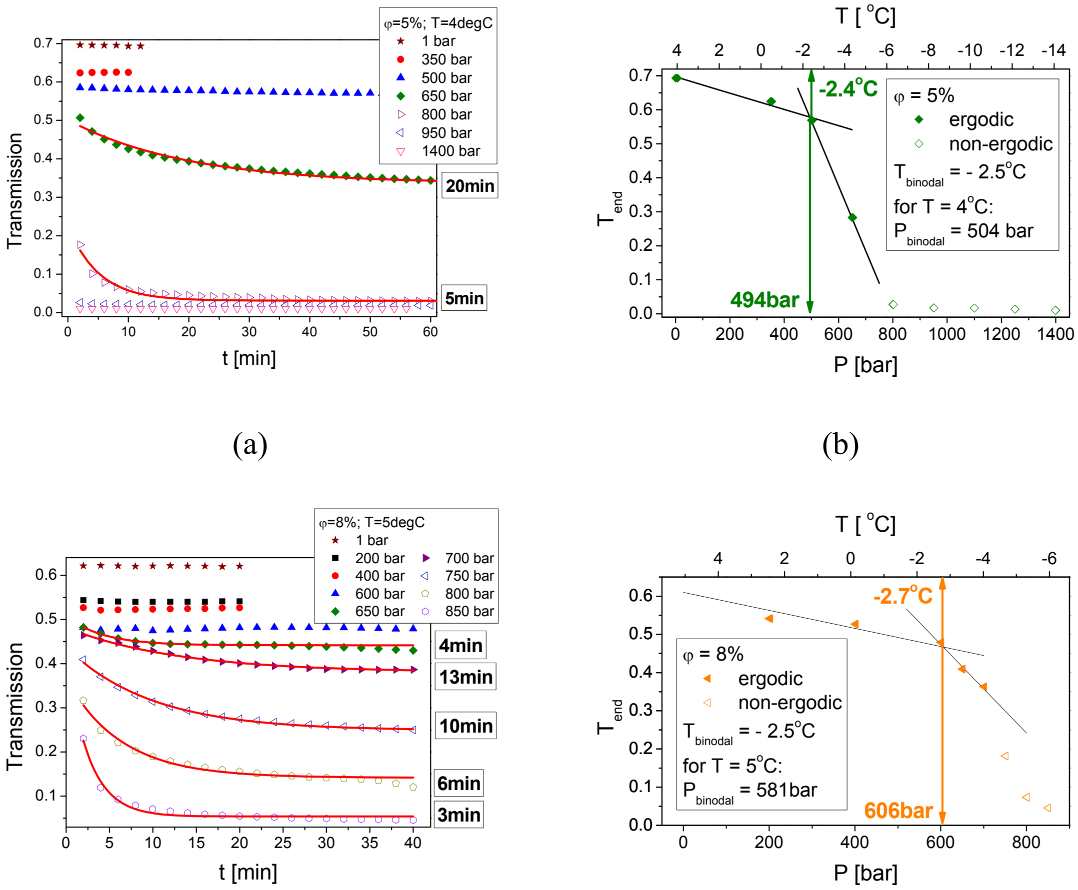

(a) (b)

(c) (d)

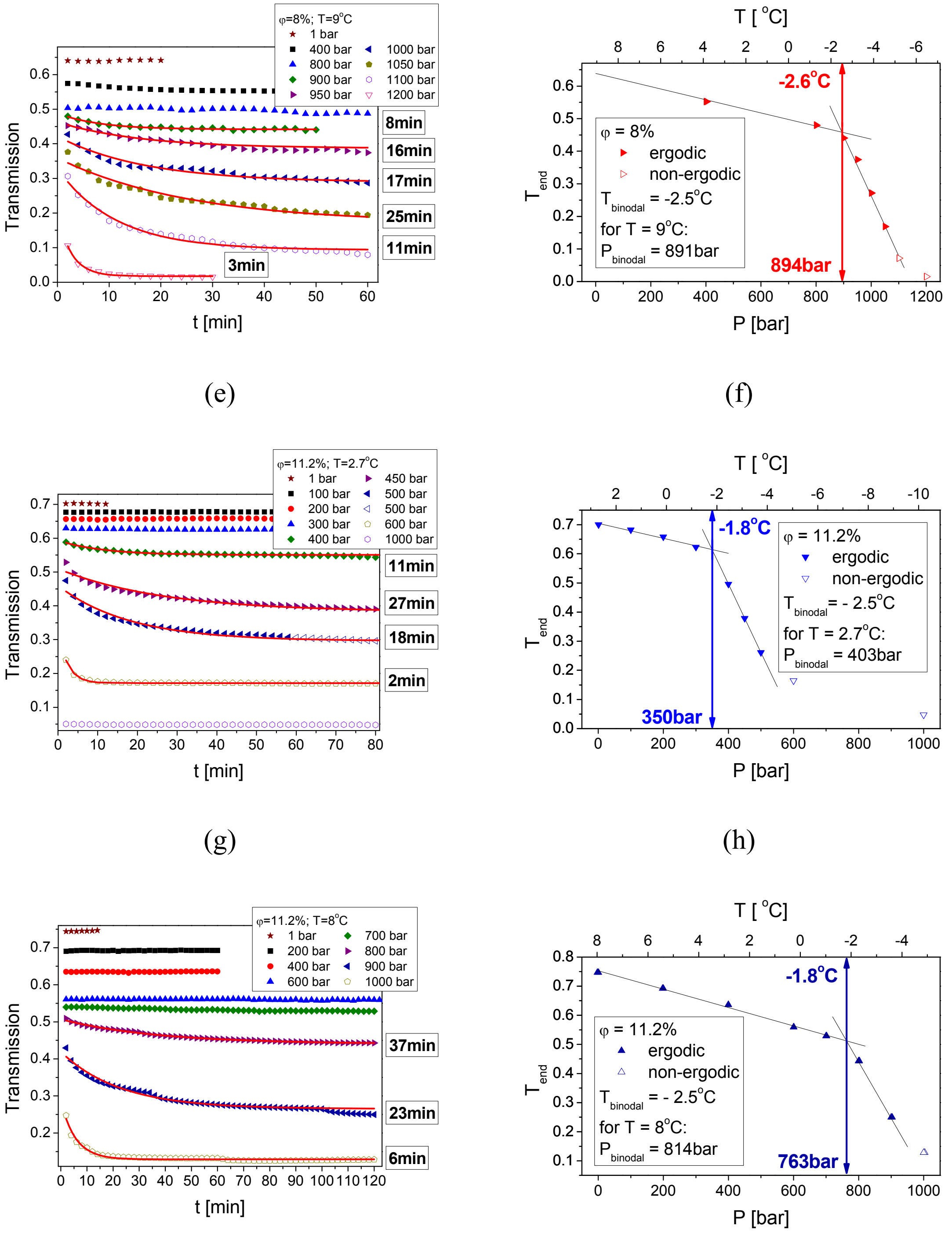

(e) (f)

(g) (h)

(i) (j)

Fig.2.8. Results of the time-dependent transmission measurement for the sample of the volume fraction of: (a) φ=5% at T=4ºC, (c) φ=8% at T=5ºC, (e) φ=8% at T=9ºC, (g) φ=11.2% at T=2.7ºC, (h) φ=11.2% at T=8ºC. The filled and hollow symbols stand for the ergodic and non-ergodic state, respectively. The red lines are the fits done using Eq.2.10. (which is discussed in subchapter 2.3.4.), and the results of the

characteristic times are given as well. The end transmission values versus pressure and temperature for the: (b) 5%, (d) and (f) 8%, (h) and (i) 11.2% sample. The pressure values were calculated to temperature according to the *dP/dT* relation. Black lines represent the linear fits, and the loci of their intersections correspond to the binodal, which is indicated by an arrow. The predicted values of binodal pressures and temperatures are given.

The time dependency of the transmission, which is presented in figure 2.8.a,c,e,g,i will be discussed further in subsection 2.3.4.

2.3.3. Analysis of forward scattering intensity and first approach to determine the spinodal line

In the time-resolved SANS measurements, similarly to the ones done using the DWS technique, the pressure was applied always from 1bar to the desired value and just in the moment of reaching it the measurement was started. The difference was the time interval, which for the neutron scattering experiment had to be higher, due to the lower intensity of the neutron beam comparing to the light, and it was set to be 5min. Any process lasting less than 5 minutes would not be resolved because of the low intensity and wrong averaging reasons.

As an example, there are a few scattering curves for the sample of volume fraction of 11.2% at T=3°C and at P=500bar plotted in figure 2.9., and in the inset the magnification of the small q region is given.

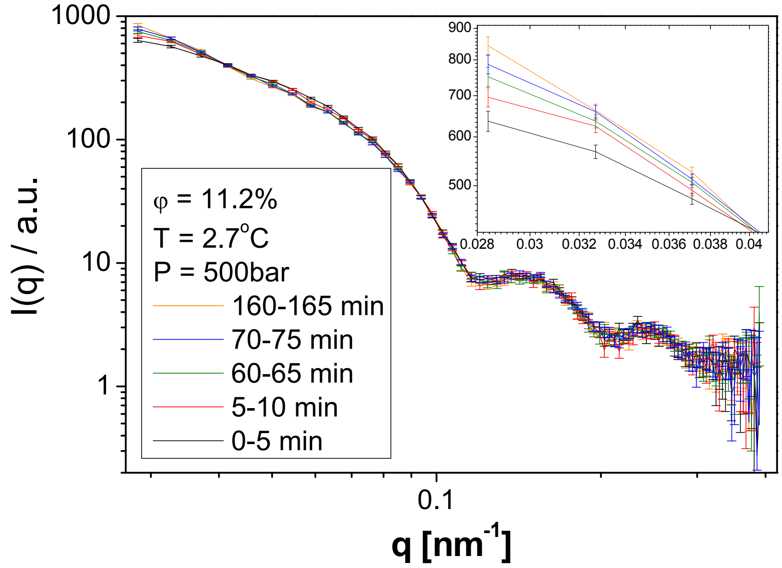

Fig.2.9. The exemplary scattering curves for the sample of the volume fraction φ=11.2% at temperature T=2.7ºC and pressure P=500bar. Inset: magnification for the small q range.

The shape of the curves remains the same in time after applying pressure, only the increase in the forward scattering can be observed. It means that the silica particles do not change their size but they tend to form aggregates. The incompressibility of the silica particles was proved before by Kohlbrecher *et al.* [35]. In order to study the time-dependent development of the forward scattering, the Guinier approximation:

$$\ln I(q) \simeq \ln I\left(q=0\right) - \frac{R_g^2 q^2}{3} \qquad \text{(Eq.2.9.)}$$

was used. Here, R_g denotes the radius of gyration of a colloidal particle.

The calibration to the absolute scattering intensities could not be done as the transmission was not measured during the experiment. In the time-slicing experiment it is not convenient to perform any measurement in between as each transmission measurement takes a few minutes and it would cause gaps in the time frame of the experiment. That is why the intensity values had to be corrected for the compressibility of the solvent (mixture of the hydrogenated and deuterated toluene) with pressure, in other words: the change of its scattering length density with pressure has to be taken into account. The relative change in the intensity due to change in the scattering length density of the solvent caused by application of pressure was calculated and the result is shown in figure below for three different compositions of the solvent, which were used to prepare the samples.

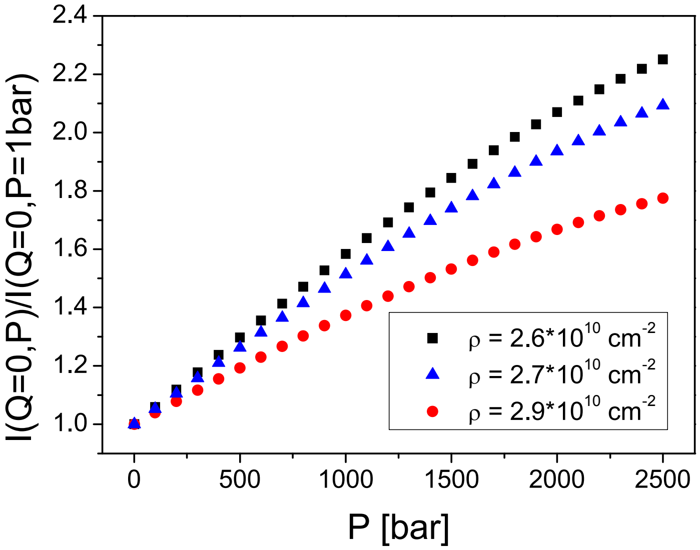

Fig.2.10. The relative change in the scattered intensity versus pressure for three different compositions of hydrogenated and deuterated toluene used in sample preparation.

Obtained from the Guinier analysis (Eq.2.9.) the intensity at q=0 for each concentration of the sample at each temperature and pressure was then divided by an appropriate factor (from Fig.2.10.). This way only the change in the scattered intensity coming from the formation of gel and/or phase separation in the sample will be taken into account and the contribution of solvent compressibility will be excluded.

Corrected this way intensities at q=0 for different pressures for all samples were then plotted versus time, which is shown in figure 2.11.

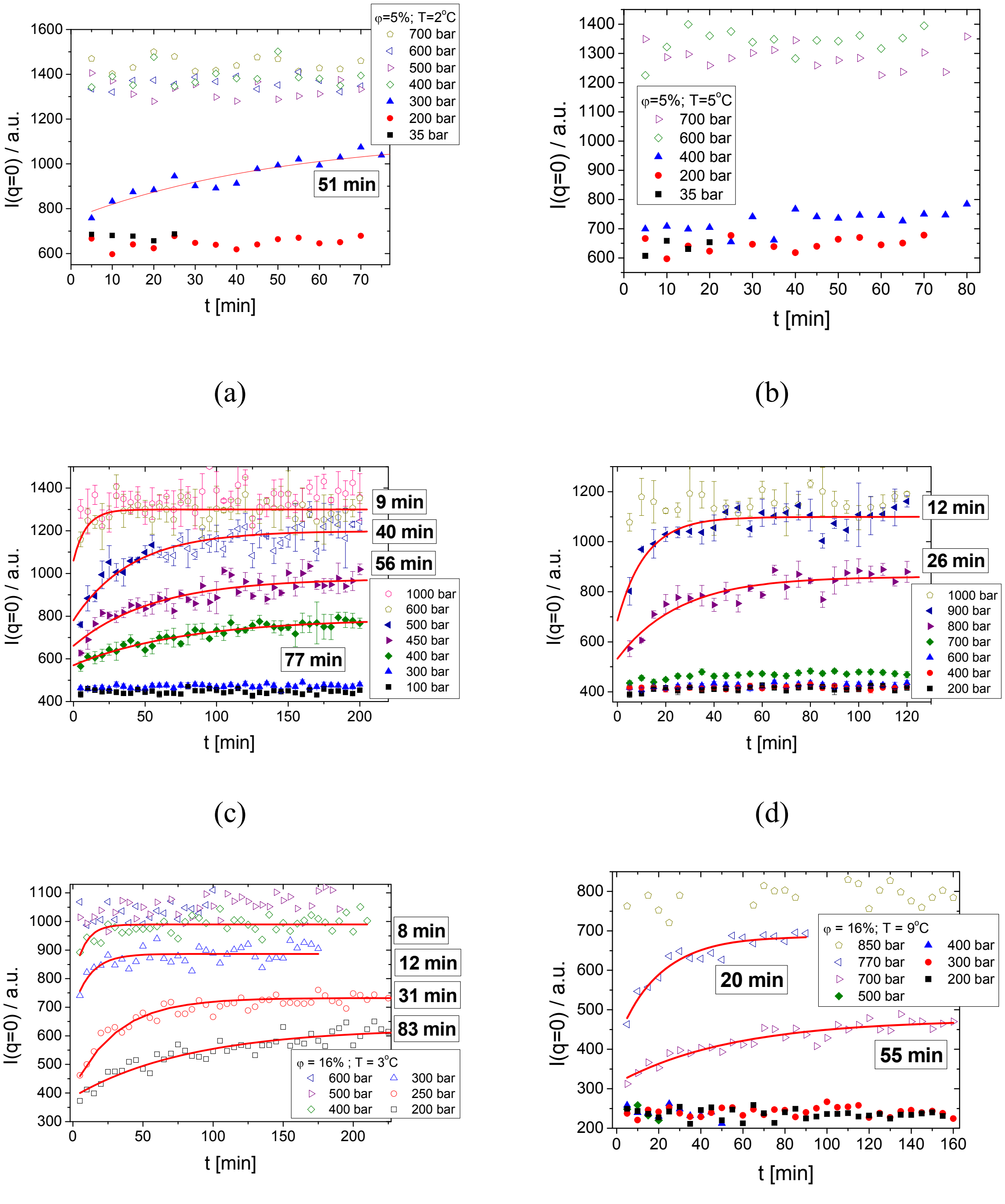

(a) (b)

(c) (d)

(e) (f)

Fig. 2. 11. *I(q=0)* versus time for the sample: (a) φ=5% at T=2°C; (b) φ=5% at T=5°C; (c) 11.2% at T=2.7°C; (d) 11.2% at T=8°C; (e) φ=16% at T=3°C; (f) φ=16% at T=9°C. The filled and hollow symbols stand for the ergodic and non-ergodic state, respectively. The red lines are the fits done using Eq.2.11. (which will be discussed in subchapter 2.3.4.), the results of the characteristic times are given as well.

As it can be clearly seen, applying small pressures does not change the forward scattering intensity. For example for the 11.2% sample at T=2.7°C the forward intensity stays constant up to pressure of 300bar and at T=8°C – up to pressure of 600bar (one can observe a slight increase of its value at P=700bar), see figure 2.11.c and d. Also for the sample of the volume fraction φ=16% at temperature T=9°C, in figure 2.11.f, no change in the value of the forward scattering intensity for the applied pressures up to 500bar was observed. Moreover, in these temperature and pressure conditions all of the samples were proved by DWS measurement to be ergodic. This indicates that the solution is homogenous, in other words – it is in the stable (one-phase) region in the phase diagram. Further application of higher pressures causes an increase in the forward scattering intensity. This can be observed for the sample of φ=11.2% at T=2.7°C in the pressure range from 400-600bar, at T=8°C from 800 to 900bar, and for the sample of φ=16% at T=3°C in the pressure range of 200-400bar. For the 11.2% sample this change is observed while the solution is still ergodic, whereas for the 16% sample, the increase of the forward scattering intensity happens when the dispersion turns non-ergodic (it crosses the percolation line). This increase in the forward scattering would be an indication of the formation of larger structures (forming clusters or network by the dispersed colloidal particles). However, for even higher applied pressures, the forward scattering intensity values level off. This can be seen for example for the 5% sample at T=2°C, where the intensity values stay constant in the range of around 1300-1500a.u. for pressures of 400-700bar (Fig.2.11.a), or for the 16% sample at T=3°C, where the intensity values stay constant in the range of around 1000-1100a.u. for pressures of 500-600bar (Fig.2.11.e). The system is non-ergodic in these temperature and pressure conditions. This means that certain structure (the sample volume filling network) was formed and its size will not change anymore while increasing pressure, at least not in the time-frame of the experiment. The time-dependency of the forward scattering intensity will be discussed later on in subsection 2.3.4.

In the figure below, the inverse intensity values are plotted versus pressure and temperature for the 16% sample. The extrapolation to zero of the time-dependent data, indicated with black arrows, points the values of the spinodal pressure (and the equivalent values of temperature according to the *dP/dT* relation from Vavrin *et al.* [17]). Here, in figure 2.12.c, the previous results of G. Meier, J. Kohlbrecher, J. Buitenhuis, A. Wilk from light scattering experiment are also presented.

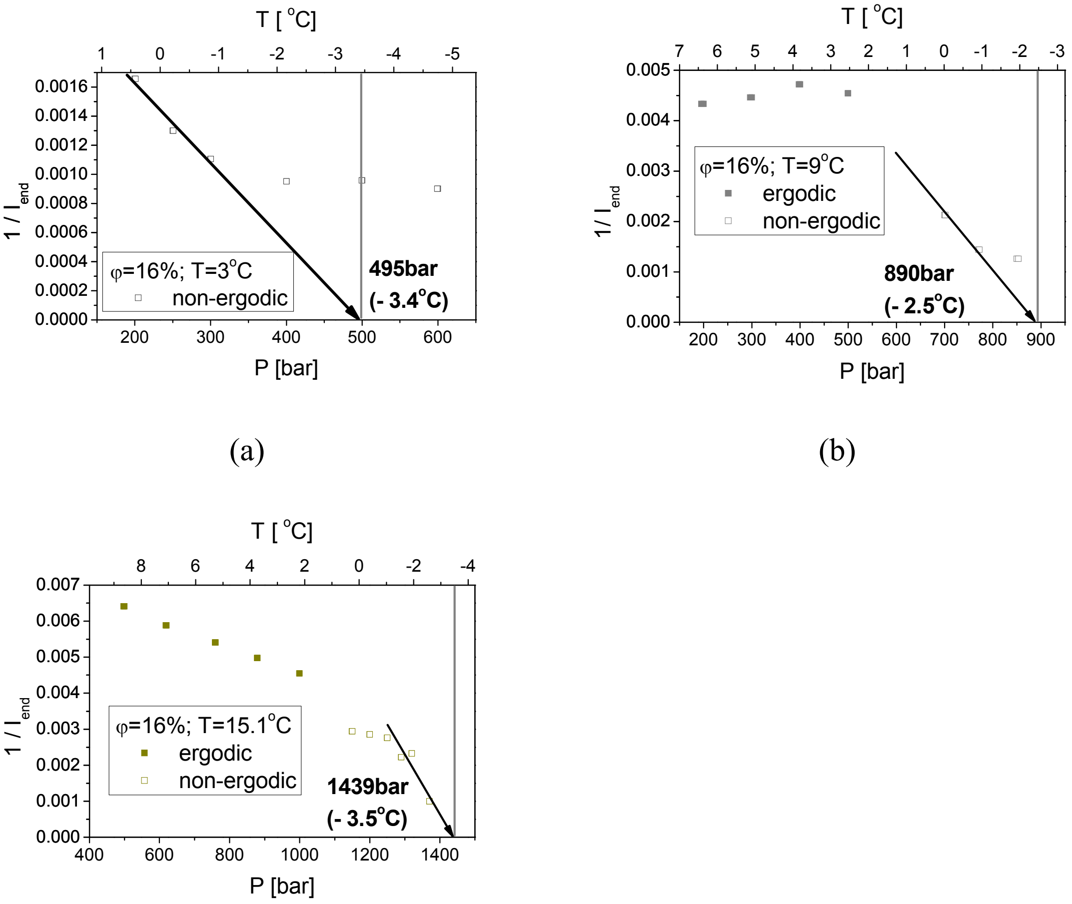

(a)

(b)

(c)

Fig.2.12. The inverse scattered intensity values versus pressure and temperature for the 16% sample at: (a) *T*=3°C; (d) *T*=9°C; (e) *T*=15.1°C. The full and hollow symbols stand for ergodic and non-ergodic state, respectively. The black lines represent the linear fits, and the loci of their extrapolation to zero correspond to the spinodal, which is indicated by the black arrows; gray lines match the spinodal pressure values with the spinodal temperatures according to the *dP/dT* relation from Vavrin *et al.* [17]. The scattering intensity in figures (a) and (b) is taken from the SANS experiment, whereas in figure (c) – from light scattering.

As it was already said in subsection 2.1 (see Eq.2.4. and its comment), from the forward scattering intensity one can obtain the information about the spinodal line. In case of the 16% sample, applying certain pressure (which correspond to lowering temperature to certain value) drives the system first to the percolation. As forming of the network by colloidal particles takes some time, one has to wait until the structure will be formed, which will be indicated by leveling off of the scattering intensity (this happens in times between 30min, after applying *P*=400bar at *T*=1.7°C, and 2 hours, after applying *P*=200bar at the same temperature). Therefore, the final values of the intensity, $I(q=0,t\to\infty)$, were taken for the 16% sample because then the percolation effects are assumed to be no longer important. As it can be seen from figure above, the spinodal occurs at temperature around -3°C for this sample.

In case of the 11.2% sample (and even smaller concentrations), while pressurizing (lowering temperature), the coexistence line is crossed first; in other words – the phase separation takes place first. That is why the initial values of the forward scattering intensity, $I(q=0,t=0)$, should be taken to estimate the spinodal. Here, the experimental limit due to the slicing time of 5 minutes causes problems in analysis of the data. The access to the forward scattering intensity values at *t*=0 is possible only through fitting the *I(q=0)* vs time data, as it is shown in Fig.2.11. Naturally, then arise the question of the accuracy of the fit and therefore some doubts about the resulting values appear. The value of spinodal temperature of around -8°C was obtained this way for the 11.2% sample, which results in around 6 degrees difference between binodal and spinodal lines. In the phase diagram of the same system dissolved in benzene obtained by Verduin and Dhont [27] the difference between binodal and spinodal lines at the same concentration was only about one degree. That is why the presented here way of determination of the spinodal temperature (pressure) for 11.2% sample seems to be incorrect due to the experimental limits.

As it was said in subchapter 2.1 (see Eq.2.5. and its comment), the other way to determine the position of the spinodal line is introducing the critical scaling law. Here as well, the initial intensity values, $I(q=0,t=0)$, were taken for the sample of φ=11.2%, and the final values of the intensity, $I(q=0,t\to\infty)$, were taken for the sample of φ=16%. In figure below, the logarithm of these intensity values is plotted versus logarithm of reduced pressure, $\varepsilon=\frac{|P-P_c|}{P_c}$. Here, the critical pressure values, for which the critical exponent is $\gamma = -1$, were found. They are given in the figure below. Obtained this way values correspond to the results from the linear extrapolation of $1/I(q=0)$. Again, the values of spinodal temperature (pressures) for the 11.2% sample obtained from the scaling procedure can be questioned as the forward intensity values at t=0 are weighted with considerable uncertainty.

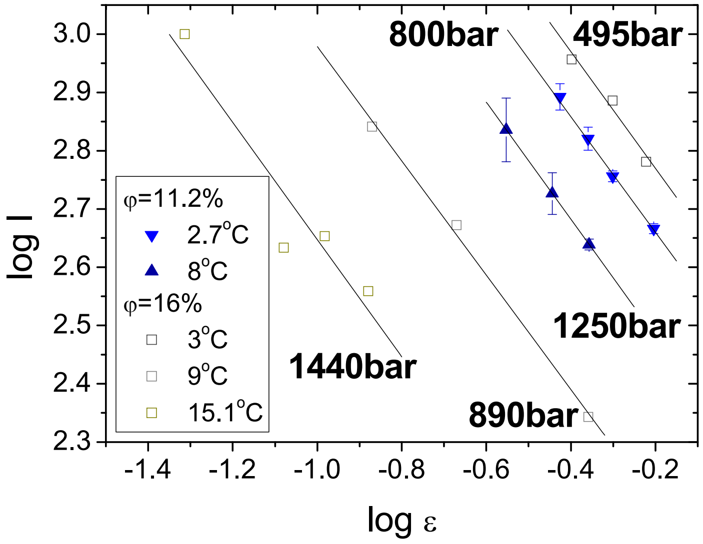

Fig.2.13. Results of the critical scaling law – logarithm of scattered intensity versus reduced pressure according to Eq.2.5. The values of P_c, for which γ=-1, are given next to the linear fit lines. Again, full and hollow symbols stand for ergodic and non-ergodic state, respectively.

In table 2.3 the results of the determination of the binodal, spinodal and percolation lines are summarized. Here, all the pressure values, corresponding to each transition, were recalculated into temperatures according to the *dP/dT* relation given by Vavrin *et al.* [17]. From the same article, the percolation threshold for the 16% sample was taken. The values for spinodal obtained in both ways, doing extrapolation and using the scaling law, are included.

Table 2.3. Summary of determination of binodal, spinodal and percolation lines.

φ [%]	T [°C]	binodal			percolation	
		$P_{binodal}$ [bar]	$T_{binodal}$ [°C]	$T_{binodal}$ [°C] from [17]	$P_{percolation}$ [bar]	$T_{percolation}$ [°C]
5	4	494	-2.39 ± 0.01	-2.5 ± 0.75	800 ± 150	-6.32 ± 1.93
8	5	606	-2.73 ± 0.09		750 ± 50	-4.68 ± 0.65
	9	894	-2.57 ± 0.05		1100 ± 50	-5.19 ± 0.65
11.2	2.7	350	-1.81 ± 0.01		500	-3.75
	8	763	-1.84 ± 0.02		1000 ± 100	-4.90 ± 1.29
16	14	-	-		1113 ± 48 from [17]	-0.36 ± 0.62

φ [%]	T [°C]	spinodal			
		extrapolation		scaling	
		$P_{spinodal}$ [bar]	$T_{spinodal}$ [°C]	$P_{spinodal}$ [bar]	$T_{spinodal}$ [°C]
11.2	2.7	798 ± 73	-7.62 ± 0.66	800	-7.6
	8	1249 ± 292	-8.10 ± 1.67	1250	-8.1
16	3	496 ± 94	-3.40 ± 0.58	495	-3.5
	9	889 ± 45	-2.48 ± 1.20	890	-2.55
	15.1	1439 ± 947	-3.48 ± 1.96	1440	-3.5

In the following chapter the time dependent behaviour of turbidity (transmission) and forward scattering intensity will be discussed and the spinodal line for low concentrations will be assumed from it. Then in the discussion, the experimentally obtained phase diagram of the investigated AHS system will be compared with the theoretical one.

2.3.4. Time dependency and second approach to determine the spinodal line

Apart from the increase in the turbidity and the forward scattering intensity, the other feature that appears is the time dependency. In the transmission measurement evolution with time starts at around the binodal point and can be analyzed with a simple exponential time behaviour:

$$T(t) = T_{end} + \left(T_0 - T_{end}\right)\exp\left(-\frac{t}{\tau}\right). \qquad \text{(Eq.2.10.)}$$

Here, T_0 and T_{end} denote the transmission values at the beginning and at the end of the experiment, respectively, and τ is the characteristic time of the decay.

The time evolution of the forward scattering intensity from the SANS experiment, on the other hand, can be analyzed with:

$$I(t) = I_0 + A\left(1 - \exp\left(-\frac{t}{\tau}\right)\right), \qquad \text{(Eq.2.11.)}$$

where I_0 is the intensity at t=0, and amplitude is $A = I_{end} - I_0$.

In figure 2.14 the values of characteristic time, obtained from using equations 2.10 and 2.11, are plotted versus pressure. The values of binodal and spinodal pressures obtained from the analysis described in previous subsections (2.3.2 and 2.3.3) are indicated with gray lines. The differentiation between ergodic and non-ergodic state is again indicated by using full and hollow symbols, respectively. There was no SANS measurement performed for 8% sample, and for the 5% sample there were no (or not enough) time-dependent data to determine the position of the spinodal line. Therefore, in order to mark possible conditions at which the phase transition to unstable state appears for these two concentrations, the result obtained for the 11.2% sample was taken. It will then indicate the highest possible position of the spinodal line in the T(or P^{-1})-φ plane for these concentrations, as it is known that the critical point for this system is positioned at volume fraction higher than 11.2% and the shape of the spinodal line is convex. That is why the spinodal temperature for concentrations lower than 11.2% cannot be higher than the spinodal temperature for this concentration. The error bars for the characteristic times are coming from the fitting, and the error bars for temperature and pressure correspond to the ranges, in which the experiments were held. The temperature in the cell has been constantly checked while running measurements, and it showed variation of ±0.5°C from the set temperature. Moreover, the pressure generator was automatically re-pumping the hydraulic oil into the cell when the actual pressure was more 30bar off from the desired value.

For the samples of the volume fraction 5%, 8% and 11.2% in the stable state (for pressures lower than $P_{binodal}$) no time dependency neither in transmission nor in the forward scattering was observed (see Fig.2.8.a,c,e,g,i and Fig.2.11). Also for the 16% sample measured at *T*=9°C, the time dependency of the forward scattering intensity starts only after applying pressures higher than 500bar. For the same sample investigated at *T*=3°C the measurements at pressures lower than 200bar would be needed to see the same tendency. It can be concluded, that small temperature/pressure changes (after which the dispersion is still in the stable state) do not cause any time dependent behaviour of the turbidity and/or forward scattering intensity of the sample. Therefore, data points for these temperature and pressure conditions will not be given in figures below.

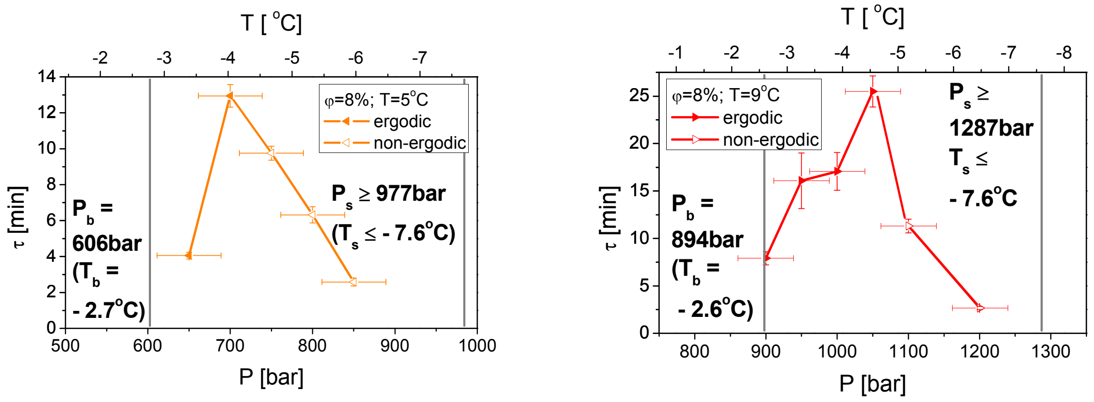

(a) (b)

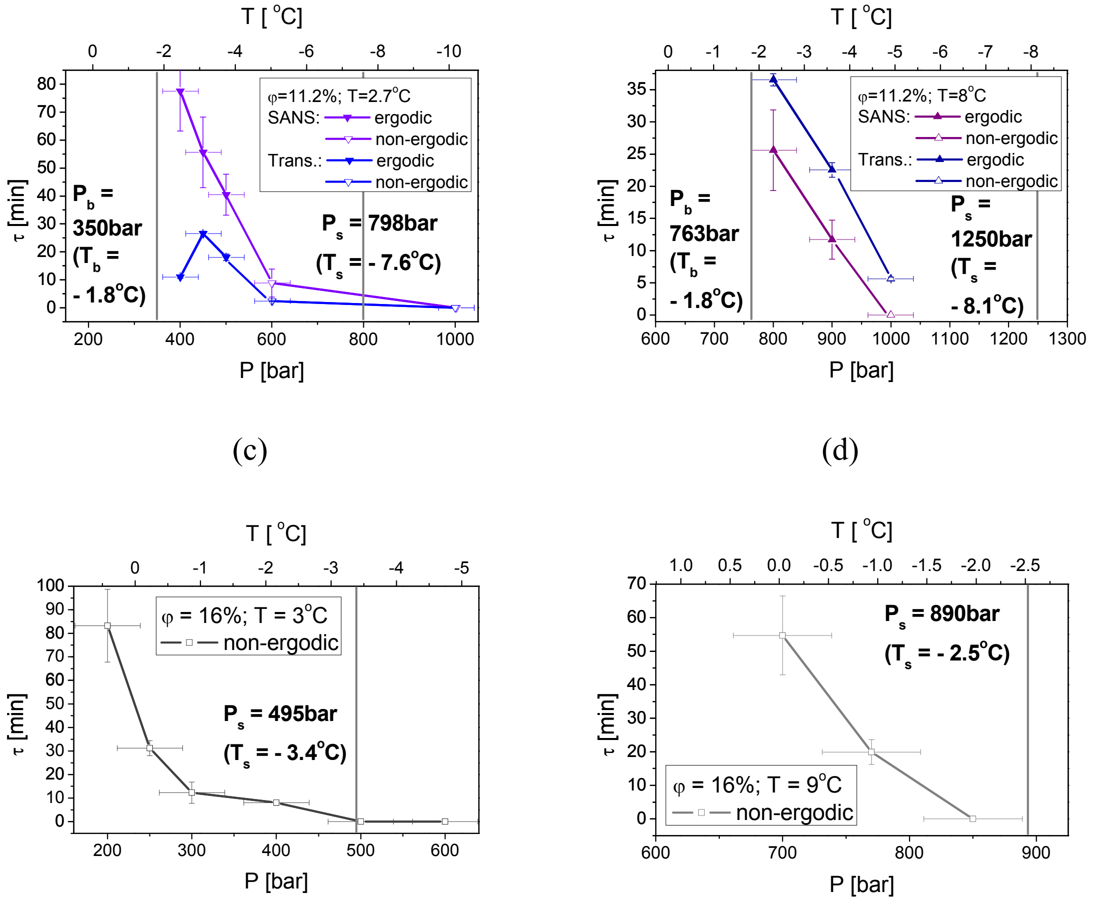

(c) (d)

(e) (f)

Fig. 2.14. Characteristic times versus pressure for: (a) *φ*=8% at *T*=5ºC, (b) *φ*=8% at *T*=9ºC, (c) *φ*=11.2% at *T*=2.7ºC, (d) *φ*=11.2% at *T*=8ºC, (e) *φ*=16% at *T*=3ºC, (f) *φ*=16% at *T*=9ºC. The characteristic times for 8% sample come from transmission measurement, for 16% sample – from SANS measurement, and for 11.2% sample – from both techniques. As before, ergodic state is marked with full symbols and non-ergodic with hollow symbols. Additionally, values of binodal and spinodal pressures are indicated with gray lines.

The most detailed measurement was carried for the 8% sample (Fig.2.14.a and b). Here, it is clearly seen that the time dependency starts after passing the binodal line, at the beginning the characteristic time is small – system reaches the equilibrium state fast, then it increases (it takes longer for the system to equilibrate) until the transition to the non-ergodic state appears and after passing the percolation line one can observe the tendency: the deeper the quench is, the faster it gets for the system to reach its final state.

For the sample of volume fraction of 11.2%, which is shown in Fig.2.14.c and d, after the pressure jump of around binodal pressure value, the time evolution started as in the case of 8%. However, for this sample, and especially in the measurement taken at T=8°C (Fig.2.14.d), one can observe the tendency that the higher the pressure was applied, the faster system reaches its final state even before passing percolation line, unlike for the 8% sample. But, naturally, one can claim that a measurement for pressure between 700 and 800bar would be needed to state firmly if that is actually the case or if, simply, the additional measurement would reveal the same tendency observed for the 8% sample. Especially, that the transmission results for the 11.2% sample measured at T=2.7°C show the similar tendency as the sample of φ=8%.

It is even more difficult to make any statement about the 5% sample as there are not enough results. Although here, one can observe that after applying very high pressures (from 950 to 1400bar), the system is brought immediately to its final state – no time-dependency is observed anymore (see Fig.2.8.a and b).

For the 16% sample the situation is different. Here, the time dependency starts after passing the percolation line and it shows the tendency that the bigger the quench (pressure jump) is, the shorter time is needed for the sample to reach its final state. After passing the spinodal line, no time-dependency is observed any more.

As it was said in the previous subchapter, the values of spinodal temperature (pressures) for the 11.2% sample obtained from the extrapolation of inverse forward scattering intensities at t=0 and from the scaling procedure are weighted with considerable uncertainty. That is why other approach to determine the spinodal line is proposed. Bringing the system by quenching (changing temperature and/or applying pressure) into unstable state, the phase separation will proceed through the spinodal decomposition mechanism. In this case any (even small amplitude) density fluctuations decrease the Helmholtz free energy and lead to decomposition. Performing deeper quench into the unstable state will cause larger inhomogeneities and the demixed state will be reached faster, which one can attribute to the decrease in characteristic time τ. Therefore, at these temperature and pressure conditions, where τ decreases, the transition to the unstable state (passing spinodal line) can be expected. The pressure values, at which the maximum in characteristic time was observed, are summed up in table 2.4.

Table 2.4. Summary of the spinodal line determination from the characteristic times of transmission and forward scattering intensity time dependency.

φ [%]	T [°C]	$P_{spinodal}$ [bar]	$T_{spinodal}$ [°C]
5	4	650 ± 150	-4.39 ± 1.93
8	5	700 ± 50	-4.03 ± 0.64
	9	1150 ± 50	-5.84 ± 0.64
11.2	2.7	450 ± 100	-3.11 ± 1.29
	8	800 ± 100	-2.32 ± 1.29

The values of spinodal temperatures for each concentration given in the last column in the table above were calculated using *dP/dT* relation.

2.4. Discussion

Finally, in figure 2.15 the experimentally obtained binodal, spinodal and percolation lines are plotted on the theoretical phase diagram. The positions of the spinodal line from both approaches, from analysis of forward scattering intensity (extrapolation and scaling) and from maximum in characteristic times, are marked with solid and dashed blue lines, respectively. The experimental results concerning the position of the percolation threshold for samples of volume fractions 1% and 39.2% and binodal line for 1% sample from Vavrin *et al.* [17] are added in the figure. The stickiness parameter, in which the theoretical phase diagram calculated by Miller and Frenkel [16] and by Fantoni *et al.* [26] (C1 model) was expressed, was re-calculated into temperature in Celsius scale using:

$$T = \frac{\Theta_0 L}{L - \ln\left(\frac{12\Delta\tau_B}{2R+\Delta}\right)} - 273. \qquad \text{(Eq.2.12.)}$$

The radius of the colloidal particles were determined as *R*=34.2nm by Kohlbrecher *et al.* [35], and the values of Δ=0.5nm, Θ_0=282K and *L*=107 were taken from Vavrin *et al.* [17].

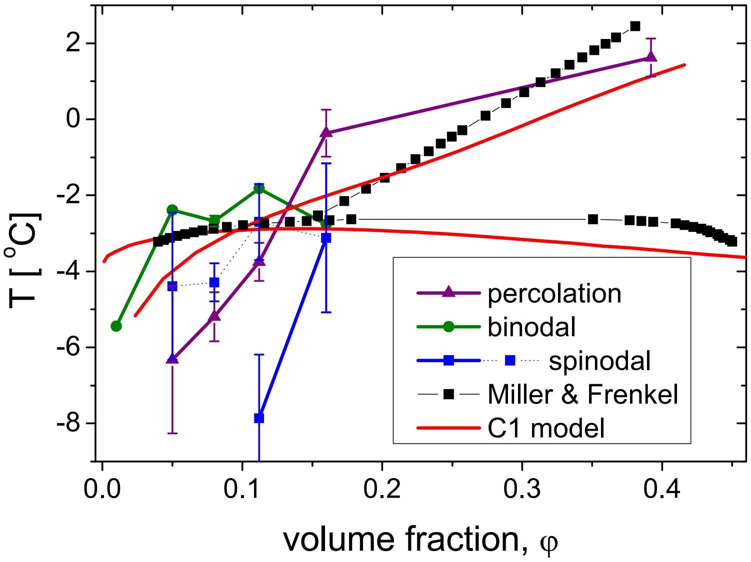

Fig.2.15. The phase diagram of AHS system – comparison of theory with experimental results.

Depending on the location of the spinodal line for low concentrations, two possible scenarios can be given. The first one will describe the situation, where the spinodal line (determined from the analysis of the forward scattering intensity) lies much lower than the coexistence line. In this case phase separation will be realized via nucleation mechanism. The second scenario relates to the situation, where the spinodal line (determined from the maximum in the characteristic time) is placed close to the binodal line and the phase separation by spinodal decomposition mechanism is possible. Regardless the method of determining the spinodal line for low concentrations, the results for 16% sample can be easily explained, as its behaviour is grossly affected by percolation effects and this case will be discussed firstly. Then both of the scenarios of phase behaviour for lower concentrations will be given.

2.4.1. Phase behaviour of 16% sample

What differs the sample of volume fraction φ=16% from those of lower volume fractions, is that here while pressurizing (lowering temperature), the transition from ergodic to non-ergodic state is observed first. Only after decreasing temperature even more, the phase separation starts. The position of percolation threshold was already determined by Vavrin *et al.* [17] for the measurement done at T=14°C. The non-ergodic behaviour appeared after applying pressure of 1113bar, which corresponds to lowering temperature to: $T_{perc} \approx 14°C - \frac{1113bar}{77.5} \approx -0.4°C$. It can be also seen from the SANS data taken at T=9°C that applying pressures lower than 700bar (which corresponds to lowering temperature to around 0°C) does not cause any transition – the dispersion stays in the stable state (see Fig.2.11.f). This is reflected in the lack of the time dependency of the forward scattering intensity. For higher pressures, in other words – for lower temperatures, the system percolates. This is reflected not only in the increase of the forward scattering intensity but also in its evolution with time. Formation of a percolating network is a process that takes some time, moreover, one can see the tendency that the deeper the quench is (the higher the pressure jump amplitude), the faster it takes for the system to reach its final state. The final state is reflected by a time-independent forward scattering intensity value. The systems gels faster because the interactions are stronger, the stickiness parameter gets smaller. At some point, after lowering temperature significantly enough (for example by applying pressure of 850bar, which corresponds to: $T \approx 9°C - \frac{850bar}{77.5} \approx -2°C$), system reaches its final state immediately. This, on the other hand, is the location of the coexistence line, which is known from the theoretically predicted phase diagram (see Fig.2.15). Moreover, for the sample of this volume fraction, the spinodal line is expected to be located near the binodal line – around one degree lower, which is in the range of the experimental uncertainty. The fact that the intensity is becoming time-independent at large pressure amplitudes means simply that here a so called gelation assisted by phase separation is taking place. This mechanism was already proposed by Verduin and Dhont [27] and by Verhaegh *et al.* [15]. To sum up, the increase of the forward scattering intensity for higher pressures is governed by the proximity to the spinodal line but the percolation effect controls the time scale. The growth of the scattering intensity is due to the evolution of a critical structure which was proved to follow a mean field type of scattering behaviour [17].

2.4.2. First scenario of phase behaviour of low concentrated samples – phase separation through nucleation process

The transient behaviour for the 5% and 8% samples can be seen in the results of the light transmission measurement, see figure 2.8.a,c,e. The experimentally obtained temperature and pressure conditions at which binodal line appears are in the agreement with the previous predictions of Vavrin *et al.* [17] (see Fig.2.8.b,d,f). Also the position of the percolation line was determined from the DWS experiment.

On the other hand, the SANS data for the 5% sample are the only ones characterized by the difficulty to observe time dependency. The only trace of it appears at T=2°C and P=300bar, see figure 2.11.a. The increase of the forward scattering intensity can be observed between 300bar and 400bar in the measurement done at T=2°C, and between 400 and 600bar in the measurement done at T=5°C. In these temperature and pressure ranges the transition from a stable into a two-phase state is expected, as – according to *dP/dT* relation and binodal temperature obtained previously by Vavrin *et al.* [17] – at T=2°C the pressure value of around $P_{binodal} \approx (2+2.5)\cdot 77.5 \approx 350 bar$ should be applied to reach the phase separation, and at T=5°C: $P_{binodal} \approx (5+2.5)\cdot 77.5 \approx 580 bar$. Inspecting figure 2.11.a and b more closely one also notices no further increase of $I(q=0)$ with pressure, from 400bar to 700bar at T=2°C, where the scattered intensity stays in the range of 1300-1500a.u. (see Fig.2.11.a), and from 600bar to 700bar at T=5°C, where it stays in the range of 1200-1400a.u. (see Fig.2.11.b). In the SANS experiment, the 5% sample was brought from the stable state (T=2°C, ambient pressure) to percolated state by applying pressure of 700bar, which correspond to lowering temperature of about 9°C. In the light of the results of the spinodal temperature determination from analysis of

I(q=0) for other concentrations, the 5% sample at temperature of around $T \approx -7°C$ is expected to be in the meta-stable region in the phase diagram, therefore it is expected to decompose via nucleation process. However, due to the presence of the percolation line (that appears possibly even at around -3°C or -4°C), the demixing process is restricted by the percolation effect. The colloid-rich phase is characterized by a percolated state giving rise to a non-ergodic scattering behaviour.

In the DWS and turbidity measurements this sample was brought, by applying pressure of 1400bar, from stable state at T=4°C and ambient pressure to (probably) unstable state at $T \approx -14$ °C. The time dependence of the transmitted light can be still seen at P=800bar (which correspond to $T \approx -6°C$), where the system is already non-ergodic but not yet unstable. It vanishes at around P=950bar (which correspond to $T \approx -8°C$). Any change in the transmission was not observed for pressures 950-1400bar, at least not within the accuracy of the photodiode used in the experiment. In the meta-stable region the time dependency of transmitted light can be observed, which can be explained with increasing turbidity of the sample whilst formation and growth of the droplets of the colloid-rich phase. On the other hand, no time dependency in the forward scattering intensity could come from the fact that the position of the spinodal is at much lower temperatures, and in the investigated temperature and pressure range the system is far away from this transition.

At the volume fraction of 8%, as for the 5% sample, the binodal is crossed first upon pressurizing, after which the time dependency of the transmitted light starts. This transient behaviour has a distinct maximum in the characteristic time τ, which was derived from equation 2.11, and it is shown in figure 2.15.a and b. At the beginning, characteristic times exhibit increasing tendency with pressure until a point, where the percolation effects come into play, and then they decrease. For phase separation many processes over a variety of time- and length-scales are involved, like initial structure formation, mass transport via diffusion and droplet coalescence. Therefore, the point at which time dependence sets in is associated with location of the phase separation. Initial increase in characteristic time while applying higher pressures reflects the fact that higher density gradients build up and the system needs longer time to reach its equilibrium state. This slow evolution of the turbidity takes place in the pressure range of 650-750bar at

T=5°C, and 900-1050bar at *T*=9°C. But this trend is abruptly broken at somewhat higher pressures for both temperatures. Specifically, the system becomes non-ergodic as deduced from DWS measurements just after maximum in τ was reached. In other words, phase separation via nucleation and growth is a fully ergodic process. But when the percolation transition is crossed, the higher pressure is applied, the faster it takes for the system to reach its final state. Eventually, for high enough pressures the system gels immediately. One has to keep in mind that each time the pressure quench (which correspond linearly to lowering temperature) was done from ambient to the desired value within seconds up to a few minutes, depending on the depth of the quench, which means that the system was driven very fast from the stable to the biphasic or percolated state.

To sum up, for these both low concentrations the percolation line was observed at lower temperatures than the coexistence line, the difference is roughly about 2°C. The location of the percolation line below the binodal line is in agreement with previous theoretical and experimental findings [11,[13,[14,[27]. The phase separation already starts in a temperature range, where no percolation was observed, and its kinetics changes as soon as the percolation line is crossed. The spinodal line lies below the percolation line and the unstable state of the system is characterized by vanishing of time dependency in turbidity of the sample.

The 11.2% sample was characterized using SANS and DWS combined with turbidity measurements. In this case, for both, forward scattering intensity and transmitted light, the time dependency could be observed. The temperature and pressure conditions at which binodal line appears, obtained from the turbidity measurement, are in the agreement with the predictions of Vavrin *et al.* [17] within the uncertainty coming from the *dP/dT* relation (see Fig.2.8.h and j). The results of the DWS experiment for this particular concentration are especially interesting because they reveal that the percolation effect sets in some time (around 1 hour in this case) after applying pressure (see Fig.2.11c for 500bar). On this basis one can expect to observe similar behaviour for the lower pressure values (400bar and 450bar at *T*=2.7°C) after times longer than the time-frame of the experiment. Both DWS measurements, at *T*=2.7°C and at *T*=8°C, give the percolation threshold for this concentration at temperature of around -4°C (within the experimental error), which is about 1.5 degrees lower than the binodal line. The position of spinodal was determined from the analysis of the forward scattering intensity from SANS experiment: on one hand from extrapolation of the inverse intensity versus pressure (temperature), and on the other – using critical scaling law. Both approaches gave similar result and the transition to unstable state is expected to appear at around -8°C, which is 4 degrees lower than the percolation threshold. The sample stays stable when pressures up to 300bar at T=2.7°C and pressures up to 700bar at T=8°C are applied. This corresponds to lowering temperature to around -1°C, where the system is still in the stable state. The time dependent behaviour of the turbidity of the sample as well as the of time dependent behaviour the forward scattering starts after passing the coexistence (binodal) line (see Fig.2.15c and d). The passage from stable to biphasic region appears at temperature of around -2°C. In principle the tendency: the bigger pressure applied, the faster it gets for the system to reach its final state, is observed. At temperature of around -4°C the transition from ergodic to non-ergodic appears, and bringing the dispersion into even lower temperatures (pressurizing more) causes vanishing of time dependency. The percolation is immediate. Then, at temperature of around -8°C the transition to unstable state is expected.

To conclude, this scenario of phase behaviour of the investigated AHS system explains why time dependency in $I(q=0)$ in SANS experiment for very low concentration (5%) was not observed. It is due to the location of the spinodal at much lower temperatures, and in the investigated temperature and pressure range the system is far away from this transition. Thus, phase separation for low concentrations of the sample proceeds through nucleation mechanism, which is a fully ergodic process. However, such temperature difference between the position of binodal and spinodal lines is rather unexpected. This rather big difference shows discrepancy with the findings of Verduin and Dhont [27] for the same AHS system consisting of silica spheres grafted with stearyl alcohol dispersed in benzene (which, as well as toluene, is a marginal solvent for the octadecyl chains). There, the spinodal lies of around 2 degrees lower than the coexistence line at volume fraction of 5% and around 1 degree at 10%. The gel line found in this work was obtained using DLS and visual observation of the scattered speckle pattern and pertains to static percolation, whereas the theoretical predictions give presumably dynamic percolation, i.e. a case of an infinite cluster at each instant of time with configuration changing in time. Using DWS technique determine rather the dynamic percolation threshold, therefore presented here results are in agreement with theoretical phase diagram, unlike Verduin and Dhont findings [27].

2.4.3. Second scenario of phase behaviour of low concentrated samples – phase separation through spinodal decomposition process

This case differs from the previously described in the way of determination and thus the location of the spinodal line. As it was proposed in chapter 2.3.4, passing of the system into unstable state is attributed to the maximum in the characteristic times of turbidity and forward scattering intensity time dependency. The location of coexistence and percolation lines stays the same as in the first scenario.

Here, the phase separation takes place mainly through spinodal decomposition process, as the spinodal lies closer to binodal line than in the previous case. For the 8% sample the gap between coexistence and spinodal line is of around 100bar (which corresponds to 1.3 degrees) for the measurement taken at T=5°C, and of around 150bar (1.9 degrees) for the measurement at T=9°C. For the 11.2% sample this gap is of about 50bar (which corresponds to 0.6 degrees) for the measurement taken at T=2.7°C, and about 100bar (1.3 degrees) for the measurement at T=8°C. These results follows the expected tendency that while lowering concentration, the distance between coexistence and binodal line should increase, as for the volume fractions below the critical point the shape of the spinodal line is convex. Obtaining relatively small temperature difference between coexistence and spinodal lines (comparing to the estimation given in the first scenario) is in agreement with the findings of Verduin and Dhont [27] for the same system dissolved in benzene. Taking results for 8% sample, in this gap the time-dependent increase of turbidity (equivalent to the decrease of transmission) goes slower after applying higher pressure, see Fig.2.14.a,b. This can be attributed to the formation of droplets, as in this small temperature range phase transition would be realized through nucleation mechanism. After crossing the spinodal line, a decrease in characteristic time can be observed. Within this process percolation sets in, which can be seen especially in the results of turbidity measurement for 11.2% sample at T=2.7°C, where around one hour after applying pressure of 500bar the system becomes non-ergodic. Eventually after applying sufficiently high pressures, the final state is achieved immediately by the system (time dependency neither in turbidity not in forward scattering intensity is observed any longer). In this scenario, the percolation appears immediately (within additional 50bar, which corresponds to 0.6 degrees) after transition to unstable state for 8% sample. For 11.2% sample the gap between these two is of around 100bar (1.3 degrees) for the measurement at T=2.7°C, and about 200bar (which corresponds to 2.6 degrees) at T=8°C. Inspecting experimental phase diagram presented in Fig.2.15, one can see that the difference between percolation and spinodal line is within the error bar. This is in agreement with findings of Lu *et al.* [29], which says that not only demixing proceeds through the spinodal decomposition, but also it initiates the gelation of particles, which is a direct consequence of equilibrium liquid-gas phase separation. The formation of density fluctuations, caused by thermodynamic instability (spinodal decomposition), leads to spanning clusters that dynamically arrest to form a gel. The authors also claim that it is independent from microscopic system, and should be applied to any particle system with short-range attractions.

2.5. Conclusions

The transition of the investigated AHS system to the percolated state was unambiguously determined using the double-cell DWS technique and the results are in agreement with the theoretical predictions. Also the position of the coexistence (binodal) line, obtained from the transmission (turbidity) measurement, corresponds to the one given theoretically. Two approaches of spinodal line determination were proposed for the low concentrated (5%-11.2%) samples: one based on analysis of the forward scattering intensity and later related to time-dependent behaviour of the turbidity and the forward scattering of the sample. For the high concentrated sample (16%), only the first approach was used to assign the transition to unstable state. The first method gives the difference of around 6 degrees between binodal and spinodal temperatures for the 11.2% sample (see blue solid line in Fig.2.15). For lower concentrations it is expected to be even bigger. Moreover, in this scenario the spinodal line lies below the percolation line, which means that the gelation occurs before the phase separation takes place. The other approach results in much smaller difference between binodal and spinodal temperatures in the investigated concentration range (up to around 2 degrees, see blue dotted line in Fig.2.15), and in this case the spinodal line lies above the percolation line, which means that gelation is preceded by the spinodal decomposition process. At this point, it is hard to judge which one (or if any of them) is correct. Nevertheless, from the results for 11.2% sample one can see that transition from ergodic to non-ergodic state sets in when the system is phase separating and moreover, it can happen after some time after quenching (see Fig.2.7.b). This means that the difference between phase separation and percolation can be distinguished. For 16% sample the observed increase of the forward scattering intensity for higher pressures is governed by the proximity to the spinodal line and it is due to the evolution of a critical structure which was proved to follow a mean field type of scattering behaviour [17]. The percolation effect controls the time scale of the increase of the forward scattering intensity.

In order to solve the problem of determination of spinodal line the small angle light scattering measurement could be performed, as it has advantage over SANS technique because it gives access to smaller *q*-range and, due to the higher flux, the shorter measurements can be taken, which gives more detailed information about kinetics of the processes that the system undergoes. However, the difficulty that has to be solved first is the turbidity of the sample, which spoils the classical light scattering experiments. The pressure cell for SALS is similar to the one used in SANS experiments [39] and the sample is placed in a pill of 2mm thickness. The preliminary attempts were already made to diminish the optical path length through reducing the sample thickness to 1mm by using glass window with thickening in its centre but this turned out not to be sufficient.

3. Temperature- and pressure-dependent behaviour of PEP-PEO polymeric micelles in water and water-DMF solutions

3.1. Introduction

The study of the deformation and phase behaviour of soft particles, such as proteins, (micro)gels or polymers, induced by pressure has attracted a lot of interest not only for the understanding of mechanisms that govern the phenomenon but also because of the whole range of technical applications. For example, some bacteria can live under extremely high pressure and low temperatures in the deep ocean [44], therefore study of behaviour of proteins under pressure is of biological relevance, as proteins structure and dynamics determine their biological functions [45-[48]. Also polymers are used under high pressure: in lubrication, where fluid pressure can reach values up to 40kbar [49], or as viscosifiers to enhanced oil recovery fluids, where pressures of a few thousand atmospheres are encountered [50], to mention only a few examples of industrial application. Moreover, pressure as an experimental variable has a twofold advantage. Changing of pressure can be performed much faster than varying of temperature. Also using temperature jumps one has to wait longer until the whole sample will be equally heated or cooled down.

Among other polymers, poly(ethylene oxide) (PEO) has attracted a lot of interest. Due to its unique properties [51-[60], it has been extensively studied for understanding the behaviour of polymer solutions and also for its broad range of technical applications [61-[63]. It readily adsorbs at particle interfaces [64], confers steric stability [65,[66], acts as good retention aid, surfactant and drag reducing agent in industrial process [67-[69]. It has been investigated as well as for its biological applications [70], as it is biocompatible and inhibits protein adsorption [71,[72]. Unlike its lower and higher homologues, PEO is soluble not only in large number of organic solvents but also in water up to around 100ºC. The solubility of PEO is due to hydrogen bonding between the oxygen on the polymer chain and the water molecules. An increase in temperature causes the reduction of hydrogen bonds, which decreases the solvent quality and leads to phase separation. There is much experimental [51-[57] and theoretical [58-[60] research on the phase behavior of PEO/water systems, also concerning pressure dependence. PEO in water exhibits a lower critical solution temperature (LCST), above which there is a two-phase region. Cook *et al.* [55] showed, in addition, that application pressure of around 4kbar dramatically lowers the LCST of PEO in water to room temperature. On the other hand, also below room temperature the solvent quality is reduced and the pressure required to induce a phase separation can be lower. The worsening of the solvent quality below room temperature may be due to the van der Waals attraction between them or the formation of the water tetrahedral network with less liable hydrogen bonds, which frustrates the fit between PEO and the water network [59].

Even more interesting systems are polymeric micelles due to their more complex structure. Block copolymers poly(ethylene-*co*-propylene-*b*-(ethylene oxide)) (PEP-PEO) form micelles in water, as PEP is hydrophobic and forms a compact core surrounded by a shell of hydrophilic PEO. Self-assembling into well defined micelle with segregated core-shell structure is attributed to the high incompatibility of PEP and water which results in a large interfacial tension between the two components [73]. Moreover, from the high incompatibility of PEP with PEO a sharp core-shell interface is expected [74]. Phase behaviour of these block copolymer micelles in water will depend on PEO solubility, especially in the case of highly asymmetric structure, where PEO chains are much longer than PEP. Therefore phase separation of PEP-PEO micelles and PEO is expected at the same temperature and pressure conditions.

Another way to tune the solvent quality for PEP-PEO micelles is addition of DMF. It results in a significant decrease of the interfacial tension between PEP and the solvent (from $\gamma=46 mN/m$ in pure water to $\gamma=8.6 mN/m$ in pure DMF [73]), which entails reduction of the aggregation number as compared to that in pure water. It was found for highly asymmetric micelles PEP1-PEO20 (where numbers stand for the approximated molecular weight in kg/mol) that in the extreme case of dissolving these block-copolymers in pure DMF only unimers exist [73]. On the other hand, addition of DMF reduces the solvent quality for PEO, which leads to shrinkage of the micellar corona [73]. Influence of DMF on both, PEP and PEO, causes formation of smaller micelles than in pure water both, in terms of aggregation number and corona diameter. Moreover, it was found that for polymers in good solvents the radius of gyration shows no consistent trend with pressure since it may either increase or decrease with increasing pressure [75].

The pressure-dependent behaviour of polymers, gels and surfactants has attracted a lot of interest. Also behaviour of proteins (especially casein) under pressure has been investigated extensively due to its applications in food processing [76]. However, the effect of pressure on polymeric micelles was not extensively investigated so far [77,[78]. Therefore the aim of the present work was to study the influence of pressure on micellar system, as a model example of a simple structural soft matter system, represented in our case by the PEP-PEO diblock copolymer dissolved in water and in water-DMF mixture. This is the first pressure-dependent experiment on this particular micellar system. For each solvent there is a different scenario of what is happening with the system under action of pressure: in water solution a size (radius of gyration) change can be observed and in water-DMF solution – a phase separation induced by pressure. Both scenarios are sketched schematically in Fig.3.1.

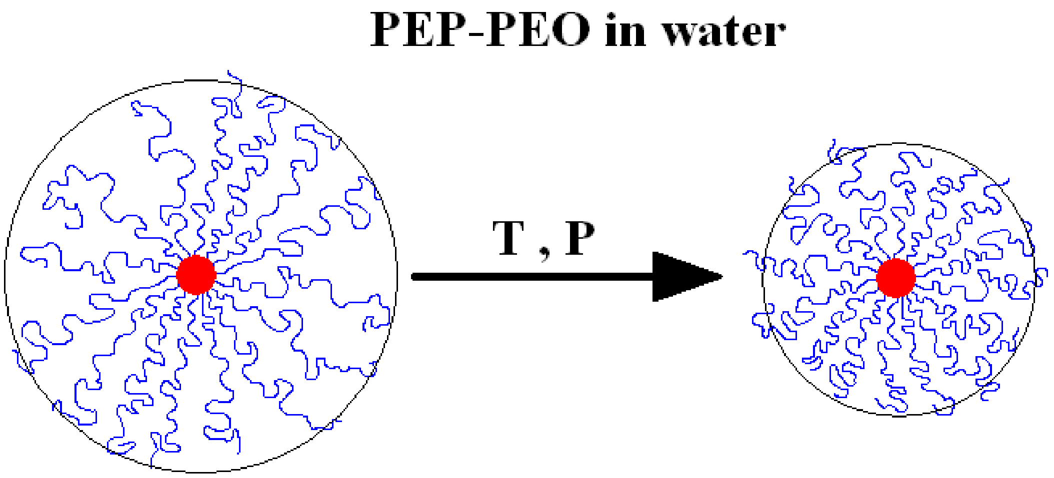

(a)

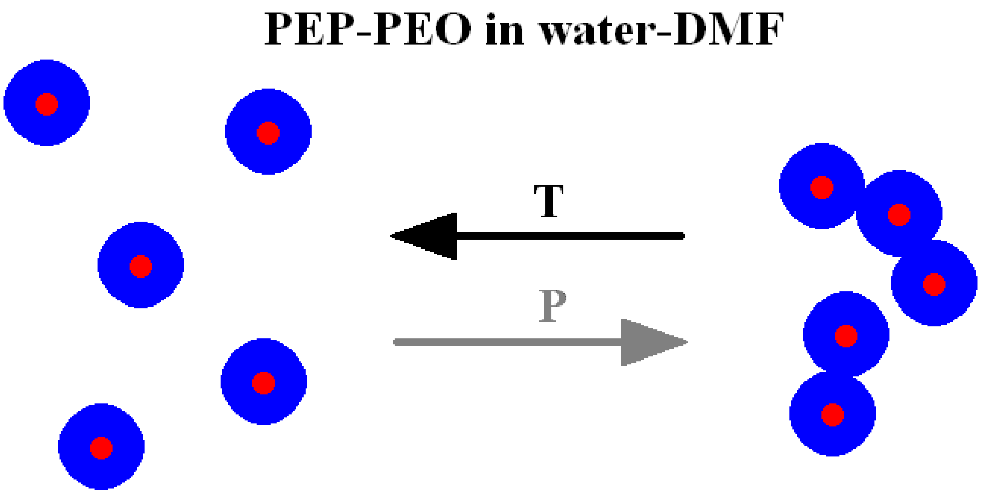

(b)

Fig.3.1. Schematic representation of the concept of the experiment: (a) investigation of pressure influence on the size of the PEP-PEO micelles in water solution, (b) investigation of phase separation induced by pressure.

These two solvents were chosen because of the difference in the quality for PEO and because of the change in the interfacial tension between PEP and the solvent, as described above. Therefore bigger micelles are expected to be formed in water than in water-DMF solution. Here, we would like to compare the influence of pressure on the same copolymer, which in different solvents will self-assemble into micelles of different sizes. In the case of PEP-PEO micelles in water, the measurements were taken in such a temperature and pressure range that the system was always in the single-phase region, as we wanted to study the influence of pressure on the micellar radius of gyration. The importance of this experiment comes from the need to determine the form factor from the single particle study before going into more complex case of more concentrated solution and also to study later phase kinetics of soft spheres. On the other hand, for the same system in water-DMF solution a macroscopic phase separation induced by pressure could be observed. The goal is to probe the phase transition induced by pressure (temperature and pressure conditions at which it appears, its reversibility). This system is more susceptible for changes in the environment than water dispersion because DMF is worse solvent for PEO than water. The highly asymmetric block copolymer was chosen because it was expected to see more pronounced reply to change of temperature and pressure than the micelles with much smaller corona.

This chapter is organized as follows: experimental section consists of two subunits describing materials, where information about the properties of both solvents as a function of temperature and pressure is described, and experimental techniques and setups, where the description of light scattering techniques and theory about fitting functions used in the analysis of SANS data is given. Results are presented in subchapters 3.3. and 3.4., which are subdivided, according to the investigated system and used technique. This is followed by the discussion and all is concluded in the last subchapter.

3.2. Experimental section

3.2.1. Materials

The poly(ethylene-propylene)-poly(ethylene oxide) diblock copolymer dhPEP5-hPEO120 and the homopolymer poly(ethylene oxide) hPEO150, provided by Jürgen Allgaier, was used. Here, the letters d and h stand for deuterated and protonated, respectively, and numbers denote approximated molecular weight in kg/mol. The details of the synthesis procedure as well as the characterization of the diblock copolymer were published elsewhere [79]. The gel permeation chromatography (GPC) measurement revealed the molecular weight M_w=117995g/mol and the polydispersity index PD=1.06 for the block copolymer dhPEP5-hPEO120, and M_w=129686g/mol and PD=1.05 for the homopolymer hPEO150. Two solutions of the diblock copolymer were prepared: one in D_2O and the other one in the mixture of D_2O-dDMF of mole fraction x_{dDMF}=0.5, both at a volume fraction of Φ=0.33%. Also a solution of the hPEO150 homopolymer in the mixture of D_2O-dDMF was prepared, where x_{dDMF} was also 0.5, at a concentration of c=2.64mg/ml (which corresponds to volume fraction of Φ=0.23%). The concentration was chosen to be around half of the overlap concentration, $c*$. Using the expression for the radius of gyration for PEO in water proposed by Devanand and Selser [80]:

$R_g = 0.215 M_w^{0.583\pm0.031}$ Å, the overlap concentration estimated from $c^* = \frac{M_w}{N_A} \Big/ \left(\frac{4\pi}{3} R_g^3 \right)$ gives c^*=5.89mg/ml.

As the homopolymer and block copolymer are fully or partially protonated, the deuterated solvents were used in order to obtain a good contrast in the SANS experiment. The same mixtures were measured also with light scattering techniques. The parameters concerning molecular weights, densities and scattering length densities of used polymers presented in the table below were taken from the PhD thesis of Andreas Poppe [81].

Table 3.1. Properties of the dhPEP5-hPEO120 diblock copolymer.

molecular weight of the copolymer	M	$[g/mol]$	128000±6500 (GPC – 117995)
molecular weight of the brush polymer (hPEO120)	$M_{hPEO120}$	$[g/mol]$	123060±6200
molecular weight of the core polymer (dhPEP5)	M_{dhPEP5}	$[g/mol]$	4940±250
molecular weight of the PEO monomer	M_{PEO}	$[g/mol]$	44.0
molecular weight of the PEP monomer	M_{PEP}	$[g/mol]$	75.8
density of PEO (at ambient conditions)	d_{PEO}	$[g/cm^3]$	1.125
density of PEP (at ambient conditions)	d_{PEP}	$[g/cm^3]$	0.924
volume of the brush polymer (hPEO120)	$V_{hPEO120}$	$[Å^3]$	8877.98
volume of the core polymer (dhPEP5)	V_{dhPEP5}	$[Å^3]$	181645.08
density of copolymer (at ambient conditions)	d	$[g/cm^3]$	1.1156
scattering length density of the brush polymer (hPEO120)	ρ_{hPEO}	$[cm^{-2}]$	6.37×10^9
scattering length density of the core polymer (dhPEP5)	ρ_{dhPEP}	$[cm^{-2}]$	4.1×10^{10}
volume fraction	Φ	-	0.0033

Table 3.2. Properties of the homopolymer hPEO150.

molecular weight	M	$\left[g/mol\right]$	129686
density (at ambient conditions)	d	$\left[g/cm^3\right]$	1.125
scattering length density of the polymer (hPEO150k)	η_{hPEO}	$\left[cm^{-2}\right]$	6.37×10^{9}
scattering length density of the solvent (dDMF/D$_2$O)	η_{dDMF/D_2O}	$\left[cm^{-2}\right]$	6.33756×10^{10}
concentration	c	$\left[g/ml\right]$	2.64×10^{-3}

D_2O (Aldrich, Deuterium oxide 99.9% D) and DMF-d$_7$ (Chemotrade, Leipzig, Germany, N,N-Dimethylformamid-d7 99.5% D; further called dDMF) for the DLS measurements were purified using the 0.2μm filters. For the SANS experiment no further purification was performed. The characterization of both solvents is given in table 3.3.

Table 3.3. Solvents – parameters.

molecular weight of D_2O	M_{D2O}	$\left[g/mol\right]$	20.04
molecular weight of dDMF	M_{dDMF}	$\left[g/mol\right]$	80.15
bound coherent scattering length of ^{2}H	b_c	[*fm*]	6.671
bound coherent scattering length of ^{16}O	b_c	[*fm*]	5.803
bound coherent scattering length of ^{12}C	b_c	[*fm*]	6.6511
bound coherent scattering length of ^{14}N	b_c	[*fm*]	9.37

In order to analyze the data from DLS and SANS experiments properly, it is important to estimate how the density (*d*), refractive index (*n*), viscosity (*η*) and scattering length density (ρ) of the solvents are varying with changing temperature and pressure. Pressure dependence of refractive index can be determined using the Lorentz-Lorenz equation (which is an extension of the Claussius-Mossotti equation to the region of optical frequencies): $\frac{n^2-1}{n^2+2}=\frac{4\pi\alpha}{3M_wN_A}d$, where α is the electric polarizability, as it is discussed by Vedam and Limsuwan [82]. The pressure-dependent values of the refractive index at given temperature are then easily calculated (knowing the density in function of temperature and pressure, and the refractive index as a function of temperature) from the ratio:

$$\frac{n^2(P)}{n^2(1bar)}=\frac{1+2Cd(P)}{1+2Cd(1bar)}\cdot\frac{1-Cd(1bar)}{1-Cd(P)}, \qquad \text{(Eq.3.1.)}$$

where the constant C is given by $C=\frac{1}{d(1bar)}\left(\frac{n^2(1bar)-1}{n^2(1bar)+2}\right)$, as it is described elsewhere [83].

From the temperature and pressure dependent values of density, the scattering length density can be calculated using the formula:

$$\rho(T,P)=\frac{\sum_{i=1}^{n}b_{c_i}}{V_m(T,P)}, \qquad \text{(Eq.3.2.)}$$

where: b_{c_i} is the bound coherent scattering length of i^{th} of n atoms in a molecule, $V_m(P)=\frac{M}{d(T,P)\cdot N_A}$ – molecular volume at certain temperature T and pressure P.

The density and the refractive index of both solvents, D_2O and the equi-molar mixture of D_2O-dDMF, in the temperature range of interest and at ambient pressure were measured with an oscillation U-tube density meter (Anton Paar, DMA 4500 Density Meter) and refractometer (Abbemat® RXA 156).

Pressure-dependent values of density of D_2O were taken from the literature [84,[85]. The values of density of D_2O from Emmet *et al.* [84] were given only for the temperature range of 2-40ºC and the pressure range of 0-1000bar. In order to expand the pressure range up to 2500bar for the temperatures T=9ºC and T=20ºC, the 2nd polynomial fit

$d(P)=A+B_1 \cdot P+B_2 \cdot P^2$ was performed. The pressure-dependent density values at temperatures of T=50ºC and T=70ºC were taken from Lee and Jonas [85] and could be fitted also using 2nd polynomial fit. The resulting values of the coefficients from 2nd polynomial fits for each temperature are given in table 3.4.

Table 3.4. Coefficients from 2nd polynomial fit of pressure-dependent D_2O density: $d(P)=A+B_1 \cdot P+B_2 \cdot P^2$ for temperatures: 9, 20, 50 and 70ºC.

	A $\left[\frac{g}{cm^3}\right]$	B_1 $\left[\frac{g}{cm^3 \cdot bar}\right]$	B_2 $\left[\frac{g}{cm^3 \cdot bar^2}\right]$
9ºC	1.106	$5.497 \cdot 10^{-5}$	$-5.351 \cdot 10^{-9}$
20ºC	1.105	$5.213 \cdot 10^{-5}$	$-4.791 \cdot 10^{-9}$
50ºC	1.095	$4.655 \cdot 10^{-5}$	$-3.478 \cdot 10^{-9}$
70ºC	1.084	$4.501 \cdot 10^{-5}$	$-3.046 \cdot 10^{-9}$

This way obtained pressure-dependent density values were used to calculate refractive index and the scattering length densities according to formulas 3.1. and 3.2., which were further taken into account in the analysis of the experimental data. Temperature- and pressure-dependent values of viscosity of D_2O were taken also from the literature [85,[86] and were also used in the further analysis of the data from light scattering measurement.

The pressure-dependent specific volume values were found in the literature [87,[88] only for the mixture of equi-molar H_2O-DMF (at the temperature of 5, 15 and 50ºC and at pressure ranging from 1 to 1000bar in steps of 200bar). From these values the density at 30, 35 and 40ºC in the same pressure range was calculated. In order to obtain the density values for higher pressures (up to 2000bar) the 2nd polynomial fit was carried out, and these values were then rescaled, so that the density values at ambient pressure for the protonated mixture would be shifted up to overlap with the values for the deuterated mixture. The resulting values of the coefficients from 2nd polynomial fits for each temperature are given in table 3.5.

Table 3.5. Coefficients from 2nd polynomial fit of pressure-dependent density of equi-molar D_2O-dDMF solution for temperatures: 30, 35 and 40ºC.

	A $\left[\frac{g}{cm^3}\right]$	B_1 $\left[\frac{g}{cm^3 \cdot bar}\right]$	B_2 $\left[\frac{g}{cm^3 \cdot bar^2}\right]$
30ºC	1.072	$4.978 \cdot 10^{-5}$	$-7.702 \cdot 10^{-9}$
35ºC	1.066	$5.102 \cdot 10^{-5}$	$-8.077 \cdot 10^{-9}$
40ºC	1.061	$5.227 \cdot 10^{-5}$	$-8.452 \cdot 10^{-9}$

From the density values obtained in this way, the scattering length density and the refractive index of the solvent were calculated, as described above, for the temperature and pressure range of interest. The change of scattering length density will be further taken into account in the fitting procedure of the SANS data and the change of refractive index – in the analysis of the DLS data.

The viscosity of this mixture was measured in the temperature range of 15-50ºC at ambient pressure using the falling ball Micro Viscometer (Anton Paar AMVn) and the data could be easily fitted with 2nd polynomial: η[mPa·s] = 4.049[mPa·s] - 0.095[mPa·s/ºC]·T + $7.623 \cdot 10^{-4}$[mPa·s/ºC^2]·T^2. In order to obtain the pressure-dependent viscosity values, the DLS measurement was performed under high pressure on a dilute colloidal suspension of the sterically stabilized silica particles grafted with octadecyl chains (whose compressibility was proven to be negligible), as described elsewhere [83].

3.2.2. Experimental techniques and set-ups

As the static and dynamic light scattering (SLS and DLS) were used in the experiment, these techniques will be described shortly below. The small angle neutron scattering (SANS) was already described in chapter 2.2.2.1, therefore here only the brief characteristic of the model used for fitting is given in this subsection.

3.2.2.1. Static and Dynamic Light Scattering

An experiment in which the ensemble averaged of scattering intensity is measured is referred as static light scattering (SLS), and the measurement of the actual time dependence of the fluctuating intensity is the dynamic light scattering (DLS). In a SLS experiment the ensemble averaged properties of density fluctuations are probed, whereas in DLS experiment – the dynamics of density fluctuations [89].

In case of N identical particles, the total electric field at the detector $\vec{E}_d$ can be expressed as a sum of the contributions coming from all the particles in the scattering volume:

$$\vec{E}_d(\vec{q}) = \sum_{i=1}^{N} \vec{E}_i \exp(i\vec{q}\cdot\vec{r}_i(t)) = \vec{E}_s \sum_{i=1}^{N} \exp(i\vec{q}\cdot\vec{r}_i(t)) . \qquad \text{(Eq.3.3.)}$$

Detection of the scattered electric field is not accessible in a light scattering experiment, however, the scattered light intensity can be directly measured. The scattered intensity from N identical particles within the scattering volume is proportional to the square modulus of the total electric field at the detector, E_d:

$$I_d(\vec{q}) \propto |E_d|^2 = |E_s|^2 \sum_{i,j=1}^{N} \exp\left(i\vec{q}\cdot\left(\vec{r}_i(t)-\vec{r}_j(t)\right)\right) . \qquad \text{(Eq.3.4.)}$$

From this equation it is clear that the scattered intensity depends on the relative positions of the scatters.

Static Light Scattering (SLS)

In static light scattering experiment the average of the scattered intensity is measured. That is why extracting from the ensemble average of equation 3.4 the part which contains the structural information, the structure factor defined as:

$$S(\vec{q}) \equiv \frac{1}{N} \sum_{i,j=1}^{N} \left\langle \exp\left(i\vec{q}\cdot\left(\vec{r}_i-\vec{r}_j\right)\right)\right\rangle \qquad \text{(Eq.3.5.)}$$

can be obtained. The scattering intensity $I_d(\vec{q})$ is proportional to structure factor. It is a quantity that connects static light scattering measurements with theory, as it contains only information about the average relative positions of particles and can be calculated without recourse to scattering theory. Depending on the conformation of a single particle, its structure factor can be modeled with different functions. For example in case of spherical, optically homogenous particles the structure factor will have a form:

$$S(q) = \left[3\frac{qR_g \cos(qR_g) - \sin(qR_g)}{(qR_g)^3} \right]^2 , \qquad \text{(Eq.3.6.)}$$

where R_g is the particle radius of gyration. This model will be used to describe the solvent-free core of the investigated micelles. The other models used for fitting the data from scattering experiments will be presented in the subchapter 3.2.2.2.

The structure factor accounts for the interference of the scattered electric field from different volume elements within single particle (for example two monomers on the same polymer chain). The interference of electric fields scattered from different Brownian particles (for example two monomers on different polymer chains) will be described as the form factor. However, at low concentrations, where the particles are far away from each other, the interference between them is insignificant.

A special case of static light scattering experiment is small angle light scattering technique performed at angles of a few degrees.

Dynamic Light Scattering (DLS)

As it was said before, in DLS experiment the temporal fluctuations of the scattered intensity are measured and it probes the dynamics of density fluctuations. As the particles move, the differences in the path lengths $\Delta\vec{r}$ between the pair of particles changes and this cause a change of their relative phases at the detector and the intensity of the scattered light fluctuates in time [5]. Thus, the temporal evolution of the scattering intensity fluctuations reflects the stochastic motion of the scatterers. The simplest function that characterizes these temporal fluctuations is the normalized intensity autocorrelation function, which is defined as:

$$\hat{g}_I(\vec{q},t) \equiv \frac{g_I(\vec{q},t)}{\langle I(t)\rangle^2} = \frac{\langle I(\vec{q},t) I(\vec{q},t+\tau)\rangle}{\langle I(t)\rangle^2} , \qquad \text{(Eq.3.7.)}$$

where the brackets have a meaning of temporal average taken over duration time of the experiment. The term that appears in the denominator in Eq.3.7, $\langle I\rangle$, is the mean scattered intensity and is independent of time for an equilibrium system. It is convenient to introduce the normalized temporal autocorrelation function of the scattered electric field:

$$\hat{g}_E(\vec{q},t) \equiv \frac{g_E(\vec{q},t)}{\langle I(t) \rangle} = \frac{\langle E^*(\vec{q},t) E(\vec{q},t) \rangle}{|E|^2}, \qquad \text{(Eq.3.8.)}$$

as it can be simply related to spatial fluctuations in the concentration in a sample:

$$\hat{g}_E(\vec{q},t) = \frac{1}{N} \sum_{i=1}^{N} \left\langle \exp\left[i\vec{q} \cdot \left(\vec{r}_i(t) - \vec{r}_i(0) \right) \right] \right\rangle, \qquad \text{(Eq.3.9.)}$$

The decay time of this correlation function depends on the dynamics of the system (the concentration fluctuations of particles undergoing Brownian motion):

$$\hat{g}_E(\vec{q},t) = \exp\left(-\frac{t}{\tau} \right) = \exp\left(-Dq^2 t \right), \qquad \text{(Eq.3.10.)}$$

where D is the diffusion coefficient:

$$D = \frac{k_B T}{\zeta}. \qquad \text{(Eq.3.11.)}$$

Here k_B is the Boltzmann constant, T – temperature, ζ – the friction constant, which for spherical particles has a form:

$$\zeta = 6\pi\eta R_h, \qquad \text{(Eq.3.12.)}$$

where R_h is the hydrodynamic radius of diffusing particle and η – viscosity of the solution.

In case of scattered fields with Gaussian statistics, both correlation functions can be related by the Siegert relation:

$$\hat{g}_I(\vec{q},t) = 1 + \left| \hat{g}_E(\vec{q},t) \right|^2, \qquad \text{(Eq.3.13.)}$$

and the information about the dynamics of the system can be easily obtained from the decay of the normalized intensity autocorrelation function.

The SLS and DLS experiment at ambient pressure was done using the set up with Ar^+ laser emitting light of wavelength λ=632.8, pseudo cross correlation detector and the ALV-5000E digital correlator. The sample was placed in a temperature cell in the compact goniometer (ALV/SP125). The pressure-dependent DLS measurement was performed using Ar^+ laser (Spectra Physics, 3W) emitting light of wavelength λ=514.5nm and ALV-5000E digital correlator. The sample was kept in a home-built pressure cell described elsewhere [90]. The SALS measurements were performed using home-built set up consisting of: He-Ne laser (Melles Griot, 05-LHP-151, 5mW) emitting light of wavelength λ=632.8nm, home-built pressure cell, achromatic lens (AC f 80, LINOS) and EM-CCD digital camera (C9100 Hamamatsu, Visitron Systems). The scheme of pressure cell designed for SALS set-up is shown in figure 3.2. The principles of its construction and usage are similar to the ones for SANS pressure cell [39]. This cell is much smaller than the one designed for SANS, as in light scattering experiment the cross-section of incident beam is smaller (although the intensity is higher), and therefore it operates in smaller pressure range.

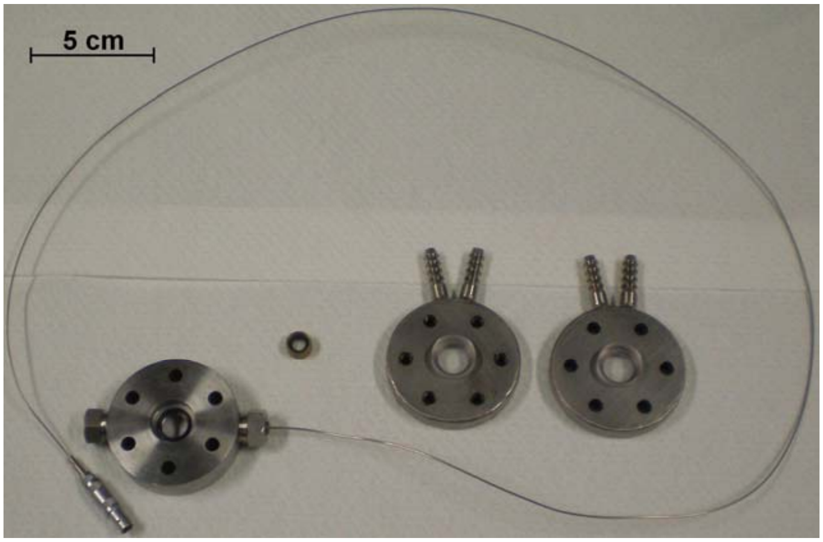

Fig.3.2. Pressure cell for SALS experiment.

3.2.2.2. Small-Angle Neutron Scattering

Small angle neutron scattering (SANS) measurements were performed also at the SANS I device of the SINQ spallation source at the Paul Scherrer Institute in Villigen, Switzerland [38]. The neutrons with a wavelength of λ=6Å were used, with a wavelength spread Δλ/λ of about 0.1,. The pressure-dependent measurements were carried at two different sample-detector distances namely, 18 and 6m, which covered the *q* range from

0.0028 to 0.039Å^{-1} and 0.0098 to 0.0118Å^{-1}, respectively. Here, q is the scattering vector, defined with θ being the scattering angle as $q=(4\pi/\lambda)\sin(\theta/2)$. The pressure cell described elsewhere [39] was used in the measurements. The measurement outside the pressure cell was performed at three different sample-detector distances (1.6, 4.5 and 18m) which give access to a q range of 0.0024-0.409Å^{-1}. The raw SANS data were analyzed using the BerSANS software package [40]. The calibration to absolute scattering intensities was done using a standard water sample. All the samples were measured in the pressure range up to 2500bar: dhPEP5-hPEO120 in D_2O at temperatures of 9, 20, 50 and 70°C; hPEO150 and dhPEP5-hPEO120 in the D_2O-dDMF were measured at T=30°C and 40°C.

Fitting models

The coherent macroscopic scattering cross section measured in a SANS experiment can be obtained from the total scattered intensity by subtracting the scattering of the solvent and incoherent scattering:

$$\left(\frac{d\Sigma}{d\Omega}(q)\right)_{coh}=\left(\frac{d\Sigma}{d\Omega}(q)\right)_{total}-(1-\Phi)\left(\frac{d\Sigma}{d\Omega}(q)\right)_{solvent}-\Phi\left(\frac{d\Sigma}{d\Omega}\right)_{inc}, \qquad \text{(Eq.3.14.)}$$

with the incoherent scattering expressed as [81]:

$$\left(\frac{d\Sigma}{d\Omega}\right)_{inc}=\frac{1}{4\pi}\sigma_H^{inc}\frac{d_{polymer}}{M_{monomer}}N_A\cdot n_H, \qquad \text{(Eq.3.15.)}$$

where $\sigma_H^{inc}=79.7\cdot10^{-24}cm^2$ is the bound incoherent scattering cross-section (taken from [91]), $d_{polymer}$ and $M_{monomer}$ are density and molar mass of the protonated monomer, n_H is the number of hydrogen atoms per monomer, and Φ denotes the volume fraction of the sample.

Core-shell model

In general, the coherent macroscopic scattering cross section has the form:

$$I(q)=\left(\frac{d\Sigma}{d\Omega}(q)\right)_{coh}=N_z\left\langle\left|A(q)\right|^2\right\rangle, \qquad \text{(Eq.3.16.)}$$

where N_z is the number density of scatterers and (assuming that the critical micelle concentration is low) is given by $N_z=\dfrac{\Phi}{N_{agg}\left(V_{dhPEP5}+V_{hPEO120}\right)}$. Here, N_{agg} is the aggregation number, and V_{dhPEP5}, $V_{hPEO120}$ – volumes of the blocks of a single polymer chain. *A(q)* is the scattering amplitude, which for a spherical micelle consisting of a inner compact PEP core and an outer swollen PEO corona can be fitted by a spherical core-shell model [74]:

$$A(q) = \left(\rho_{core} - \rho_0\right) V_{core} A(q)_{core} + \left(\rho_{shell} - \rho_0\right) V_{shell} A(q)_{shell}, \qquad \text{(Eq.3.17.)}$$

where ρ_{core}, ρ_{shell} and ρ_0 denote the scattering length densities of PEP, PEO and the solvent, respectively, volumes of the core and the shell are given as: $V_{core} = N_{agg} V_{dhPEP5}$ and $V_{shell} = N_{agg} V_{hPEO120}$. This is presented schematically in Fig.3.3.

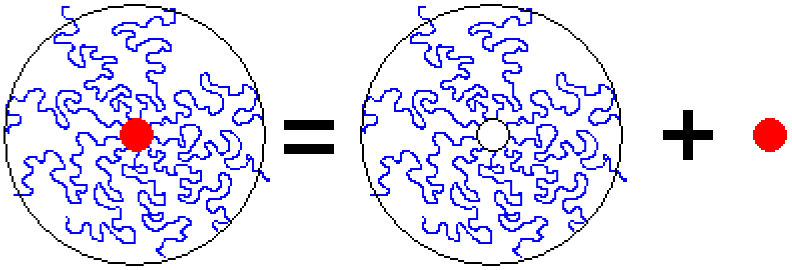

Fig.3.3. Schematic illustration of the core-shell model. The scattering amplitude from a micelle is described as a sum of the respective amplitudes from an inner compact core and an outer shell weighted by their respective (to the solvent) contrasts and volumes.

$A(q)_{core}$ and $A(q)_{shell}$ are the partial scattering amplitudes of the core and the shell, respectively, and can be calculated from the Fourier transform of the radial density distribution, *n(r)*:

$$A(q)_{core,shell} = \frac{1}{C} \int_0^{\infty} 4\pi r^2 n(r) \frac{\sin(qr)}{qr} dr, \qquad \text{(Eq.3.18.)}$$

where $C = \int_0^{\infty} 4\pi r^2 n(r) dr$ is the normalization constant. As the core is assumed to be compact with a constant density profile, *n(r)*=1, and by introducing a Gaussian distribution function (in order to take into account possible surface roughness), the scattering amplitude of the core is given by:

$$A(q)_{core} = \frac{3\left(\sin\left(qR_{core}\right) - qR_{core}\cos\left(qR_{core}\right)\right)}{\left(qR_{core}\right)^2}\exp\left(-\frac{\left(\sigma_{core}q\right)^2}{4}\right), \qquad \text{(Eq.3.19.)}$$

where σ_{core} is the smearing parameter, which was found to be insensitive to the fit quality, and it was set 0 in all cases [73]. The radius of a compact, homogenous core is given by:

$$R_{core} = \sqrt[3]{\frac{3}{4\pi}N_{agg}\frac{M_{core}}{d_{core}N_A}}, \qquad \text{(Eq.3.20.)}$$

where M_{core} is the molecular weight and d_{core} is the density of the core (the density of PEP), and N_A – Avogadro number.

For the shell, the hyperbolic density profile was assumed: $n(r) \sim r^{-x}$, with the power law exponent set as 4/3, which is the theoretical value derived for regular star polymers. Additionally, the Fermi function was introduced in order to warrant the smooth density profile decay:

$$n(r) = \frac{r^{-4/3}}{1 + \exp\left[\left(r - R_M\right)/\sigma_{shell}R_M\right]}, \qquad \text{(Eq.3.21.)}$$

with the smearing parameter, σ_{shell}, and the overall micelle radius, R_M. This can be calculated from:

$$R_M = \sqrt[3]{\frac{3}{4\pi}\frac{N_{agg}}{N_A}\left(\frac{M_{core}}{d_{core}} + \frac{M_{shell}}{d_{shell}}\right)} + d_{shell}^{+}. \qquad \text{(Eq.3.22.)}$$

Here, the extra radius of the shell (compared to compact), d_{shell}^{+}, was assumed as an additive increment on the minimal radius of the shell. An example of the density profile for polymeric stars with additional contribution of Fermi function is presented in figure 3.4. In the inset the same plot is given in logarithmic-linear scale.

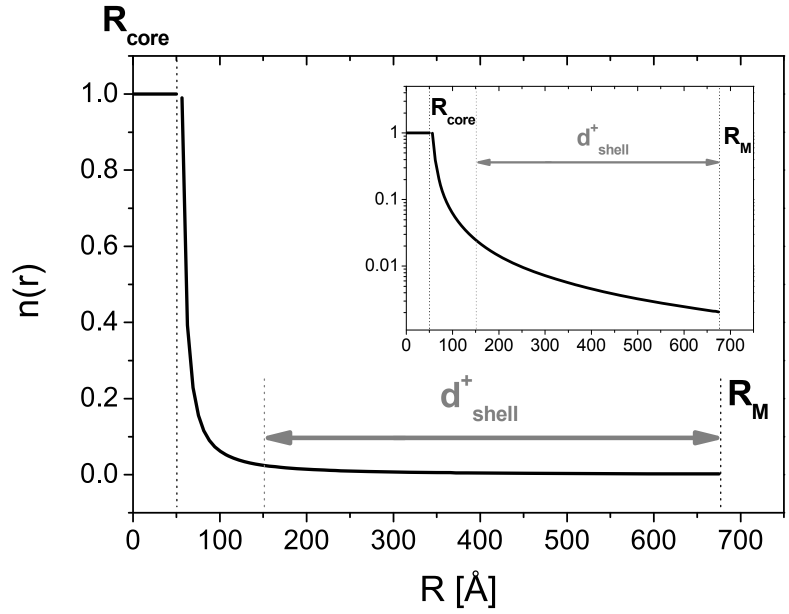

Fig.3.4. Schematic representation of the normalized hyperbolic density profile of a star-like micelle with the power law exponent set as 4/3 and the Fermi function as a cut-off function (Eq.3.15.). Parameters are: R_{core} = 50Å, R_M = 675Å and σ_{shell} = 10Å.

The fit parameters were thus d^{+}_{shell}, the aggregation number, N_{agg}, smearing parameter, σ_{shell}. Parameters such as the volume fraction, Φ, molecular weights, M_{core} and M_{brush}, densities, d_{core} and d_{brush}, and the scattering length densities, ρ_{dhPEP}, ρ_{hPEO} and ρ_0, of the individual components were taken as determined from A. Poppe PhD thesis [81] or calculated.

Beaucage model

The experimental study of the same system PEP-PEO in water done by Lund *et al.* [73] revealed that in the large *q*-range there are no pronounced minima and maxima of scattered intensity. This indicates rather diffuse corona structures characteristic for micelles with a starlike density profile. In this regime scattering comes mainly from the core and the fluctuation (blob) scattering, which was estimated using the additional unified exponential/power-law approach proposed by Beaucage [92]:

$$\frac{d\Sigma}{d\Omega}(q)_{blob} \simeq G\exp\left(-\frac{q^2R_g^2}{3}\right) + B\exp\left(-\frac{q^2R_{sub}^2}{3}\right)\left(\frac{\left[erf\left(qkR_g/\sqrt{6}\right)\right]^3}{q}\right)^P, \qquad \text{(Eq.3.23.)}$$

where G is the Guinier pre-factor, B – a constant pre-factor specific to the type of power-law scattering observed as determined by the regime in which P falls, R_g – the radius of gyration of the large-scale structure, R_{sub} – the sub-structural radius of gyration, and P – the scaling exponent of the power law assigned to the larger structure R_g. The Guinier's law (the first term in Eq.3.17.) contains only information about the average properties of the particle such as the correlation length and the volume. It does not take into account the local structure. This term, however, was omitted (G=0) in the fitting of the SANS data because the overall radius is determined already from core-shell model. The power-law (second term) on the other hand, does carry the information about the local structure. The addition of the blob scattering contribution does not influence the scattering at low q, i.e. does not affect significantly the results for the overall size of the micelle or the aggregation number, but it guarantees good agreement at large q.

Daoud and Cotton [93] developed a model for star-like polymers to describe sub-structures of polymer chain. Their concept assumes that in case of polymer of P branches connected to a single centre the outer structure is treated as a stratified array of blobs such that all blobs in a given sub-layer are of equal size but the blob size increases towards the periphery, as it is schematically represented in figure 3.5. This was extended to star-like micelles by Halperin [94].

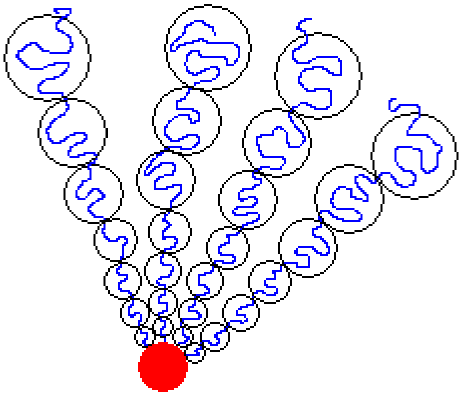

Fig.3.5. Schematic representation of the Daoud-Cotton model of the brush structure of a star-like polymer.

The full expression for the fitting function consisting of core-shell (see Eqs.3.10-3.16) and Beaucage models (Eq.3.23) used to analyze the SANS data has a form:

$$I(q) = \frac{d\Sigma}{d\Omega}(q) = N_z \left\langle \left|A(q)\right|^2 \right\rangle + \frac{d\Sigma}{d\Omega}(q)_{blob}, \qquad \text{(Eq.3.24.)}$$

An exemplary representation of both models is given in figure 3.6. The parameters used to create this plot were taken from fitting of scattering curve obtained from measurement of the investigated sample at ambient conditions (room temperature and atmospheric pressure), see figure 3.7 in next section. The resulting parameters values in core-shell model were: concentration Φ=0.0033, aggregation number N_{agg}=67, molecular weights of polymer building core (PEP) M_{core}=4940g/mol, and shell (PEO) M_{shell}=123000g/mol, densities of PEP d_{core}=0.924g/cm^3, and PEO d_{shell}=1.125g/cm^3 scattering length densities of solvent ρ_0=6.367·10^{10}cm^{-2}, of PEP ρ_{core}=4.10·10^{10}cm^{-2}, and PEO ρ_{shell}=6.37·10^{9}cm^{-2}, smearing parameter of core σ_{core}=0, smearing parameter of shell σ_{shell}=70Å, additional radius of the shell (compared to compact) d^{+}_{shell}=541 Å, core radius R_{core}=52Å, and overall radius R_M=686Å. The resulting parameters values in Beaucage model were: G=0, B=0.0006, R_g=300Å, R_{sub}=4.7Å, k=1.06, and P=1.3333.

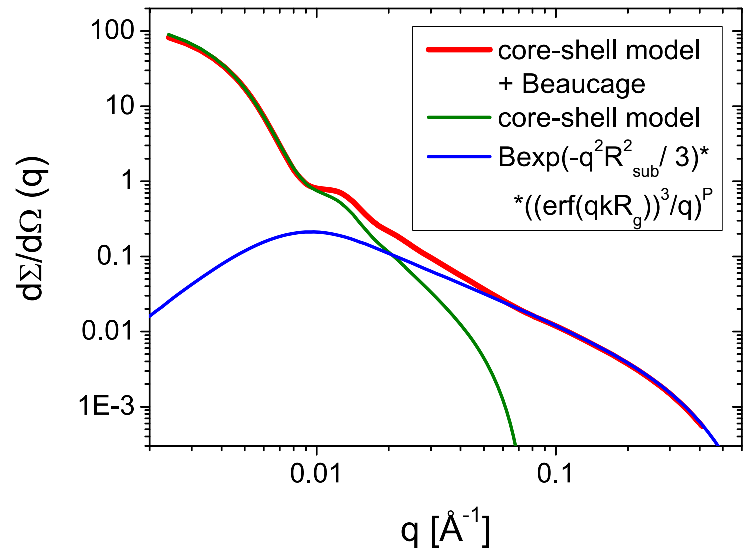

Fig.3.6. Schematic representation of core-shell model and Beaucage functions.

The analysis of the data was done using a program written by Joachim Kohlbrecher, SASfit.

3.3. Results for dhPEP5-hPEO120 in D_2O

In this subchapter, the results for the system dhPEP5-hPEO120 in D_2O are presented. The PEO is soluble in water in the investigated temperature range, and no phase separation was expected to be observed. In this case, the change of the micellar size in the function of temperature and pressure was investigated.

3.3.1. SANS results

Firstly, we present the results of the SANS measurement taken outside the pressure cell in ambient conditions (T=20°C, at ambient pressure) in order to cover a wider q-range and to determine the background correction that should be applied to the pressure-dependent data, as the solvent itself was not measured separately in the pressure cell. The scattered intensity was corrected for the scattering of D_2O and incoherent scattering coming from the protonated PEO chains according to Eq.3.14 and the result with the fits of the core-shell model, represented by the solid lines: red – with addition of the Beaucage functions, and green – without, is given in Figure 3.7.a.

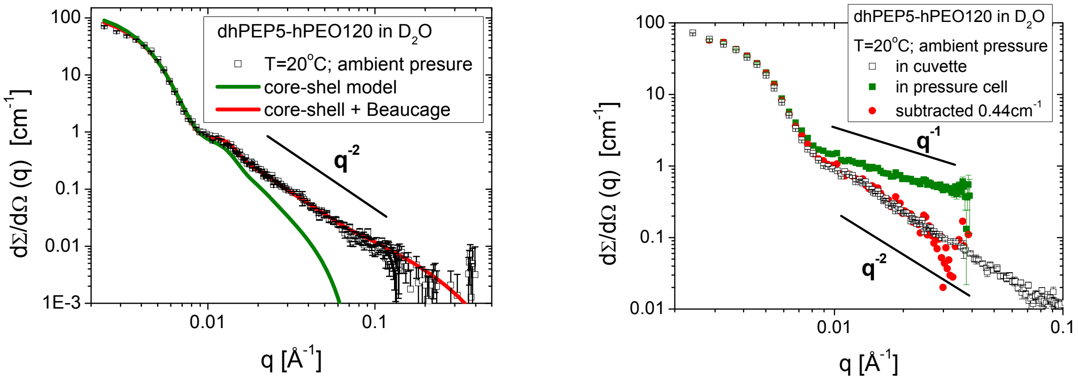

(a) (b)

Fig.3.7. (a) Results of fitting the dhPEP5-hPEO120 in D_2O at T=20ºC and ambient pressure with the core-shell model (green line), as well as those with the addition of the Beaucage function contribution (red line). (b) Comparison of the results for the dhPEP5-hPEO120 in D_2O at T=20ºC and ambient pressure: outside the pressure cell (black hollow squares), and inside the pressure cell – without (green squares) and with the subtraction of the additional background of 0.44cm^{-1} (red circles).

As it can be easily seen, the addition of the Beaucage contribution improves the fit quality in the high q-regime. In the small q-region it results in a slightly smaller aggregation number, which lowers the core radius somewhat. Without the Beaucage function the fit gives the aggregation number N_{agg}=77, core radius R_{core}=55Å, d_{shell}^{+}=536Å, which results in the overall micellar radius of R_M=687Å. On the other hand using the Beaucage contribution the fit gives N_{agg}=67, R_{core}=52Å, d_{shell}^{+}=540Å, and R_M=686Å. Concluding, we can say that addition of the Beaucage function in fitting procedure does not influence the result of the overall micellar radius.

In Figure 3.7b the comparison of the measurement in- and outside the pressure cell at ambient conditions (T=20°C, ambient pressure for the measurement outside the pressure cell and P=30bar – inside the pressure cell) is given. The result of the measurement carried in the pressure cell (green squares) shows a big difference in the higher q-region comparing to the one taken in 1mm thick quartz cuvette (black hollow squares). The scattering intensity in the higher q-region has a slope of around -1 in case of the measurement using pressure cell, and -2 in the other one. The reason of this difference lies in the background correction: the proper background subtraction was done for the measurement in the cuvette but not in the pressure cell. The scattering of pure solvent was not measured separately and that is why it was not subtracted from scattering intensity of the sample. Therefore a constant value of the background ($0.44cm^{-1}$) was subtracted from the pressure-dependent measurement (red circles) for further data analysis in order to receive the sample slope as for the data taken from the measurement without using pressure cell.

In Fig.3.8 the scattering curves at varying pressure for this system are shown. For each temperature the sample was measured in the pressure range of 30-2500bar. The data has been normalized by a factor $C = N_A / \left(\Delta\rho^2 \Phi\right)$, where $\Delta\rho^2$ is the effective excess scattering length density, using the temperature- and pressure-dependent values of scattering length density of D_2O and the bulk density of PEO to calculate its scattering length density. There is a shift to higher *q* values of the decay of the scattering curves with increasing temperature (Fig.3.8e) and pressure (Fig.3.8a-d), which indicates the decrease of the size (radius) of the micelle. Also a slight increase of the intensity at low *q* was observed while heating up and pressurizing (Fig.3.8.f), which is especially pronounced at *T*=9°C.

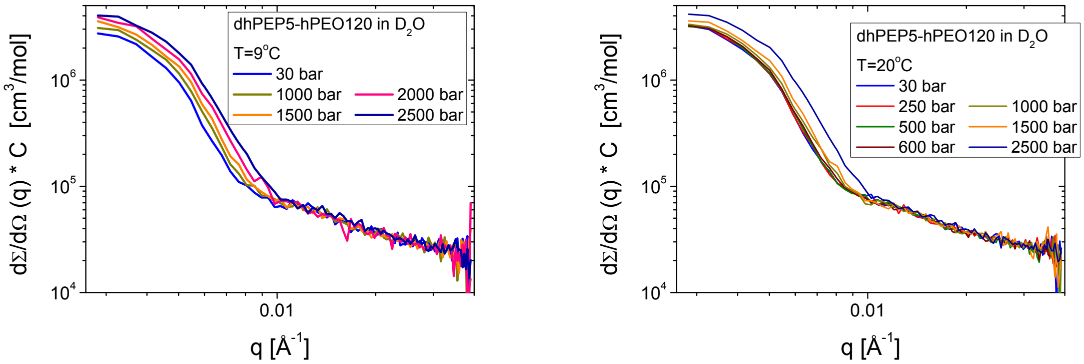

(a) (b)

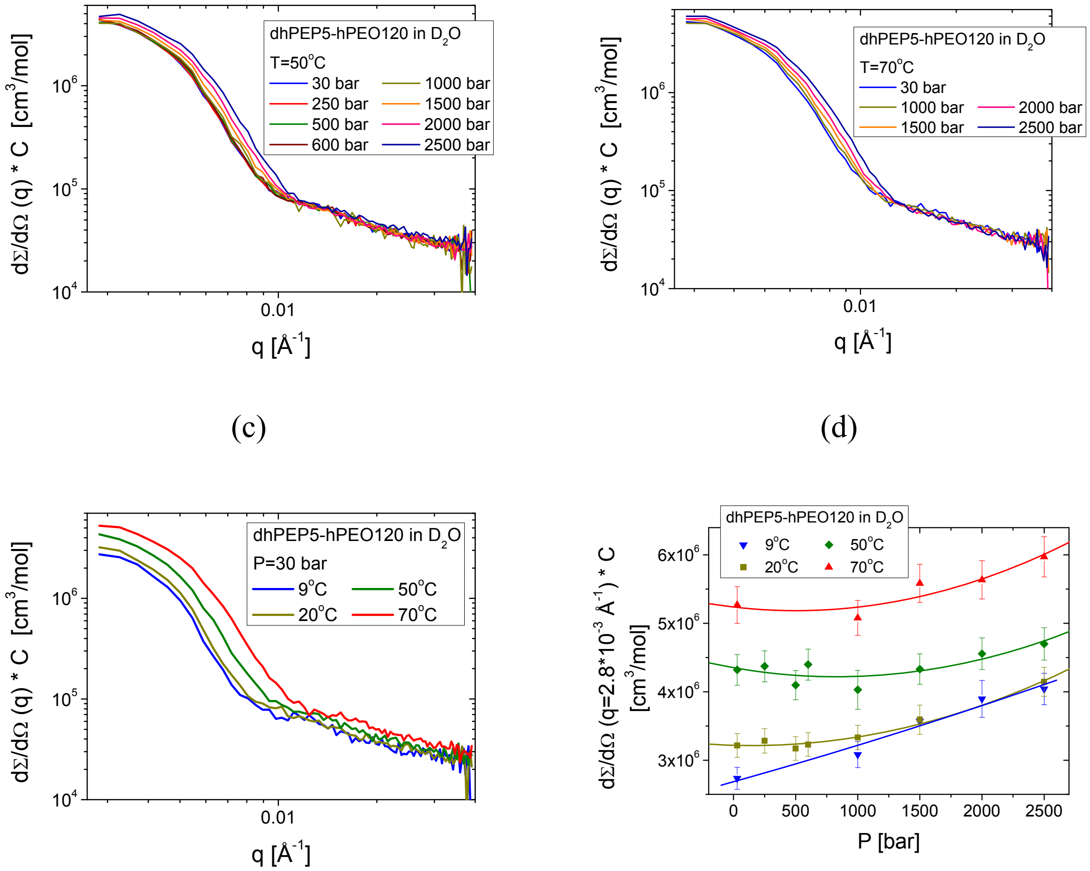

(c) (d)

(e) (f)

Fig.3.8. *I(q)* vs *q* for dhPEP5-hPEO120 in D_2O at: (a) *T*=9ºC, (b) *T*=20ºC, (c) *T*=50ºC, (d) *T*=70ºC, (e) *P*=30bar for all the measured temperatures; (f) $I(q=0.0028Å^{-1})$ vs pressure for at all measured temperatures.

The data was fitted with both models described above: core-shell and Beaucage (see Eq.3.24). In the fitting procedure the temperature and pressure dependent change of the density (see table 3.4) and scattering length density of the solvent, described in the subchapter 3.2.1, was taken into account. The aggregation number and additional thickness of the shell were obtained, from which core and overall radii were calculated (Eq.3.20 and 3.22). The results are shown in Figure 3.9.

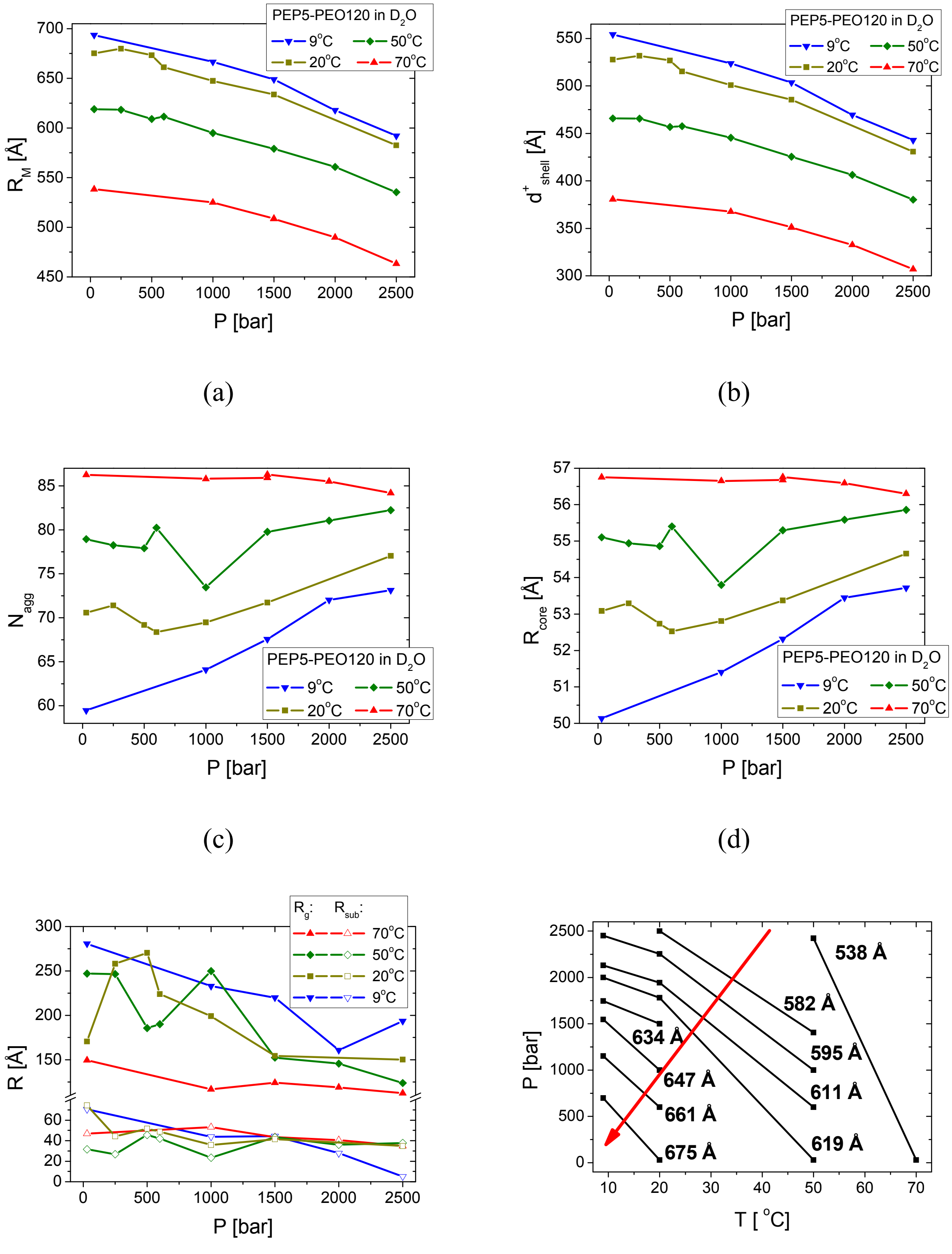

(a) (b)

(c) (d)

(e) (f)

Fig.3.9. Results of fitting with the core-shell model with the constant background and the additional contribution of the Beaucage function for the dhPEP5-hPEO120 in D_2O: (a) overall radius, (b) additional thickness of the shell coming from the presence of the solvent among polymer chains in the micellar

corona, (c) aggregation number, (d) core radius, (e) radius of gyration of the large and the sub-structure obtained from fitting with the Beaucage function, (f) temperature-pressure conditions for the equal-radii.

The results from fitting with core-shell model show clearly the decrease of the overall micellar radius with the increase of temperature and pressure, which is mainly caused by the decrease in the additional radius of the shell (d^{+}_{shell}). In the core-shell model this parameter represents the presence of the solvent in the micellar shell. Application of pressure from 30 to 2500bar causes an increase of 20% at T=9°C, 18% at T=20°C, 19% at T=50°C and T=70°C (Fig.3.9.b).

Interestingly and in contrast to the shell behavior, the pressure dependence of the aggregation number changes for different temperatures, see Fig.3.9c. At higher temperatures it remains rather constant (at 70°C it decreases around 2% and at 50°C it varies in value of about 11%, however, showing no consistent trend). Whereas at lower temperatures $dN_{agg}/dP>0$ was found. The aggregation number increases around 9% at T=20°C, and at T=9°C its change is even more pronounced, it enhances around 19% (it raises from 59 at P=30bar to 73 at P=2500bar). These changes are too small to affect the core radius or the overall micellar radius, as N_{agg} is related to them as a cubic root (Eq.3.20 and 3.22).

Using Beaucage function gives two types of gyration radii: one of the large-scale structure, R_g, and the sub-structural radius of gyration, R_{sub} (marked in Fig.3.9e with filled and hollow symbols, respectively). For the temperature of 9°C values of both radii show decreasing tendency. R_g drops down from 280Å at 30bar to 160Å at 2500bar, and R_{sub} – from 70Å to 5Å. At T=20°C R_g varies from 150Å to 270Å showing slightly decreasing tendency, and R_{sub} from 35Å to 74Å. At T=50°C R_g varies from 123Å to 250Å, and R_{sub} from 23Å to 45Å. For the temperature of 70°C values of both radii stay rather constant, R_g stays in the range of 112-150Å and R_{sub} in the range of 35-53Å. The shell of micelles consists of PEO. Therefore, one can roughly estimate the radius of gyration of such polymer chain in water using a relation proposed by Devanand and Selser [80]: $R_g = 0.215 M_w^{0.583\pm0.031}$ Å. This way for PEO of molecular weight of around 120kg/mol, $R_g \approx 200$Å is expected. This can be attributed roughly to values of R_g obtained for temperatures 9°C-50°C. The values of R_g correspond approximately to the half of

d^{+}_{shell}, hence the large-scale structures in Beaucage model are most probably the PEO chains building the micellar corona. Sub-structural radius of gyration values from the range 5Å -75Å, according to Devanand and Selser empirical expression [80], correspond to the size of a coil composed from several (5) to several hundreds (522) of monomers. The results of using Beaucage function are taken with a dose of scepticism, as they are carrying uncertainty coming from the not proper background.

In the last figure (3.9.f) the temperature and pressure conditions, at which micelle has the same radius are shown. Form this picture it is clear that there is no simple linear *dP/dT* relation, as it was found for the dispersion of the polymer grafted silica spheres in toluene, described in the previous chapter. Moreover, in this case both, applying (increasing) pressure and heating the sample, cause shrinking of the micellar corona, whereas in previous case of silica spheres, the *dP/dT* relation was negative, which means that applying pressure corresponds to cooling the sample.

3.3.2. SLS and DLS results

Here, the results of the static and dynamic light scattering experiment will be presented. These measurements were performed in order to confirm the SANS results. Firstly, the experiment taken outside the pressure cell at ambient conditions (T=20°C and no additional pressure) will be described. Then the pressure-dependent data will be shown. The values of the gyration and hydrodynamic radii obtained from these measurements will be then compared with the results of the neutron scattering experiment.

In figure 3.10 the results of SLS and DLS at ambient conditions are given. Apart from the sample of volume fraction of 0.33%, which was investigated with SANS technique, a 5 times dilution was also prepared and measured, as the more concentrated sample was not absolutely transparent. This is not a problem using neutrons, however, it limits the light scattering experiments, as it causes multiple scattering.

The scattering intensity was corrected for the scattering of the solvent (D_2O) and normalized by the scattering intensity of the reference sample (in this case toluene) according to:

$$I_{sample}(q)=\frac{I_{total}-(1-\Phi)I_{solvent}}{I_{reference}}. \qquad \text{(Eq.3.25.)}$$

The scattering curves from SLS experiment for both samples were fitted using Guinier approximation (first term in the Beaucage function – see equation 3.23), which is shown as the red line in the figure below. For the sample of the volume fraction of 0.33% it was difficult to perform the fit, therefore the result for its 5 times dilution (Φ=0.066%) is presented. The radius of gyration R_g=521.5Å from static light scattering measurement is smaller than the overall micellar radius R_M=686Å from SANS experiment.

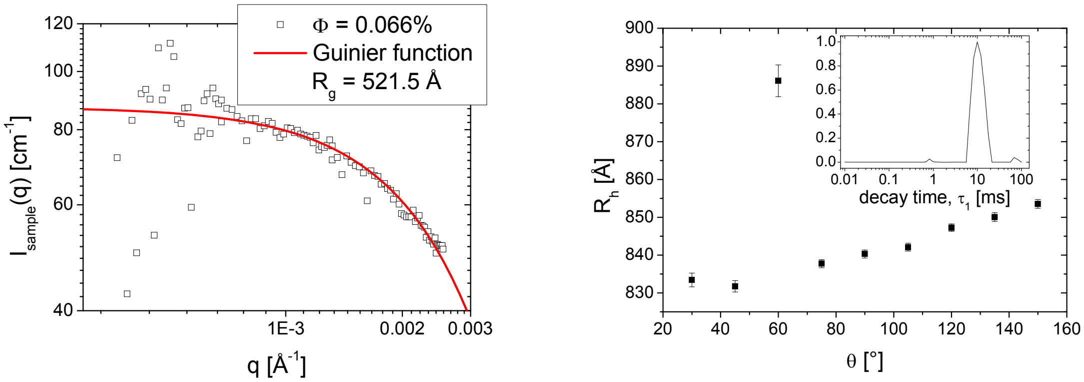

(a) (b)

Fig.3.10. Results of the static and dynamic light scattering experiment at ambient conditions for the dhPEP5-hPEO120 in D_2O solution of Φ=0.066%: (a) scattering intensity versus q fitted with Guinier function (first term in the Beaucage function – see Eq.3.23.), which is marked with red line, (b) hydrodynamic radius obtained from measurements at different angles; inset – distribution function of decay times of an exemplary correlation function (measured at θ=30°).

The DLS measurement was taken at different angles in the range 30°-150° in steps of 15°. Each run lasted 1.5 hour in order to obtain proper statistics, as the dispersion is not perfectly monodisperse, despite filtration of the sample. Also the possible presence or absence of aggregates was planned to be proven with this measurement, hence the duration time of the experiment was long. The resulting values of the hydrodynamic radius measured at different angles are plotted in figure 3.10.b. In the inset in this figure, the distribution function of the decay times of one of the correlation functions (in this particular case, measured at scattering angle θ=30°) is given. The picture of the decay time distribution for a measurement at a small angle was chosen as an example because it is sensitive for possible aggregates or any bigger objects (for example dust in the sample). It was found that the decay time distribution at θ=30° looks similarly to the ones for higher scattering angles. Therefore, one can claim the absence of aggregates. At small scattering angles the hydrodynamic radius of dhPEP5-hPEO120 micelles dissolved in water in volume fraction of 0.066% has the value of around 835Å, which is bigger than the radius of gyration from SLS and SANS technique. This is in accordance with the expectations that for micellar systems $R_h > R_g$. For spherical systems the relation between both radii is predicted to be $\frac{R_h}{R_g} = \sqrt{\frac{5}{3}} \approx 1.29$ [95]. Here, the ratio of both radii from light scattering experiments $\frac{R_h}{R_g} \approx 1.6$ was obtained. On the other hand, the ratio of R_h from DLS and R_M from SANS $\frac{R_h}{R_M} \approx 1.22$, which is in good agreement with the predicted value within less than 10% error.

Both experiments, SANS and DLS, with temperature and pressure as variables were done in similar manner. They were taken at the same temperatures and pressure was applied gradually. The difference was that the available pressure range for the pressure cell used in the DLS set up is limited to 1500bar, whereas with the pressure cell designed for SANS set up one can apply higher pressures, and pressures up to 2500bar were applied. The other problem was the condensation appearing on the windows of the pressure cell while running measurement at low temperatures. The construction of the pressure cell used in SANS experiment allows removing it by constant blowing of air on the cell windows during the measurement. It is impossible in the DLS cell. That is why the DLS measurement was not carried out at T=9°C. As it was said before, change in the refractive index and viscosity of the solvent while varying temperature and pressure (described in chapter 3.2) was taken into account in data analysis. For each applied temperature and pressure at least 3 measurements were done and they were averaged. This data set was fitted with two-exponential decay function and in figure 3.11 the values of hydrodynamic radii, R_{h1} (marked with full symbols) and R_{h2} (hollow symbols), coming from both decay times are presented.

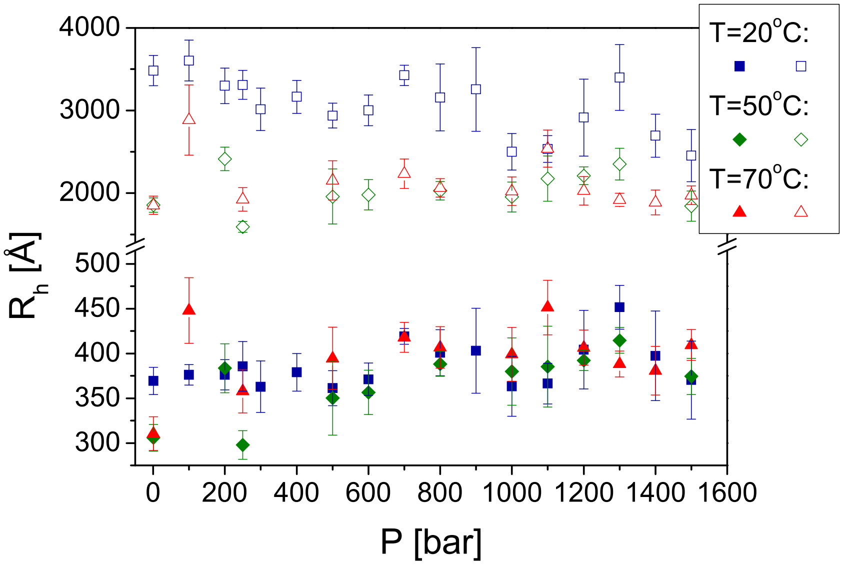

Fig.3.11. The hydrodynamic radii. Error bars correspond to statistical uncertainty.

In contrast to findings from SANS experiment, DLS data does not show any change in micellar hydrodynamic radius, R_{h1}, in the investigated temperature and pressure range. All the values lie in the range 300-450Å, while the error coming from statistical uncertainty are up to 50Å (more than 10%). A possible reason of the big error from averaging can come from the presence of different size objects in the sample (aggregates), because of which fitting with the single-exponent decay function could not be done. Another explanation is that here the sample of Φ=0.33% was used, and as it was said already before, it appears slightly turbid. This causes multiple scattering and spoils the analysis of data. In figure above also the resulting hydrodynamic radius, R_{h2}, of the bigger (than the single micelles) objects is given and its value is of an order of magnitude bigger than R_{h1}. For these aggregates there is a slight change with pressure in their hydrodynamics observed at T=20°C, where the R_{h2} value drops down from R_{h2}≈3500Å at ambient pressure to R_{h2}≈2500Å at P=1500bar. But at 50°C and 70°C no change in the radius induced by pressure was observed. Moreover, the hydrodynamic radius for both temperatures stays in the same range around 2100Å. This is in contrary to the results from SANS, where the drop in the micellar radius of around 20% with pressure at each temperature was found. However, the size of aggregates at 50°C and 70°C is smaller than at 20°C, which confirms the scenario of shrinking of the micelles while increasing temperature due to exposing the system to poor solvent conditions.

To sum up, no temperature- and pressure-dependency of micellar hydrodynamic radius was found here, unlike in previously described SANS results. It is difficult to analyze this data set because of possible presence of aggregates and problems with the sample turbidity.

3.4. Phase separation of dhPEP5-hPEO120 and hPEO150 systems in D_2O-dDMF solution

In this subchapter the results for the same block copolymer dhPEP5-hPEO120 and the homopolymer hPEO150 in the equi-molar mixture of D_2O and dDMF are presented. For the system in this solvent, unlike for its water dispersion, no change in the micellar radius induced by pressure was observed, but the macroscopic phase transition appeared. Firstly, the investigation of the phase separation induced by changing temperature at ambient pressure will be described, and then the pressure-dependent measurements will be presented.

3.4.1. Observation of phase separation at ambient pressure conditions

The small angle light scattering technique was used to study the phase behaviour at ambient pressure of the investigated dhPEP5-hPEO120 micellar system in equi-molar D_2O-dMF solution. The experiment was performed in the following manner: the sample was kept at 30°C for at least half an hour before cooling it in order to have homogenous solution before starting each measurement. It was cooled down to the desired temperature value and in the moment when the system reached this temperature, the measurement was started. For temperatures higher than 30°C the system was expected to be homogenous, therefore no time-dependent measurement was performed. In this case temperature was increased gradually and each measurement was taken around 10-15 minutes after the system reached the wanted temperature value.

In figure 3.12 the exemplary results of the time-dependent measurement taken at *T*=18°C are shown.

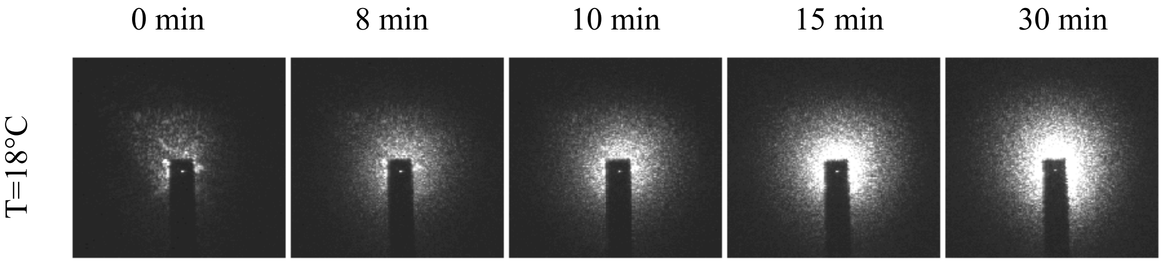

Fig.3.12. Time evolution of phase separation of dhPEP5-hPEO120 micelles in D_2O-dDMF solution at *T*=18°C.

When the system undergoes the phase separation the scattering intensity increases. For temperatures lower than 18°C the phase separation took place immediately after cooling down the sample, whereas in the temperature range 18-24°C it appeared after some time, and the tendency was observed that the higher the temperature, the longer it took for the system to phase separate (see Fig.3.13.e, below). For temperatures higher than 24°C even after one hour the system remained homogenous. The phase separation was easily visible as the denser phase of milky color appeared at the bottom of the sample and the lower transparent (just like the homogenous solution) phase was placed above.

The analysis was done using a home-written IDL program and the exemplary resulting azimuthal averaged curves are shown in Fig.3.13. Comparing figures 3.13.a-c one can see that the forward scattering intensity is not only increasing with decrease of temperature but also with time. At *T*=25°C, where the system stayed homogenous, the forward scattering intensity value remained at $8{\cdot}10^4$ and no phase separation takes place.

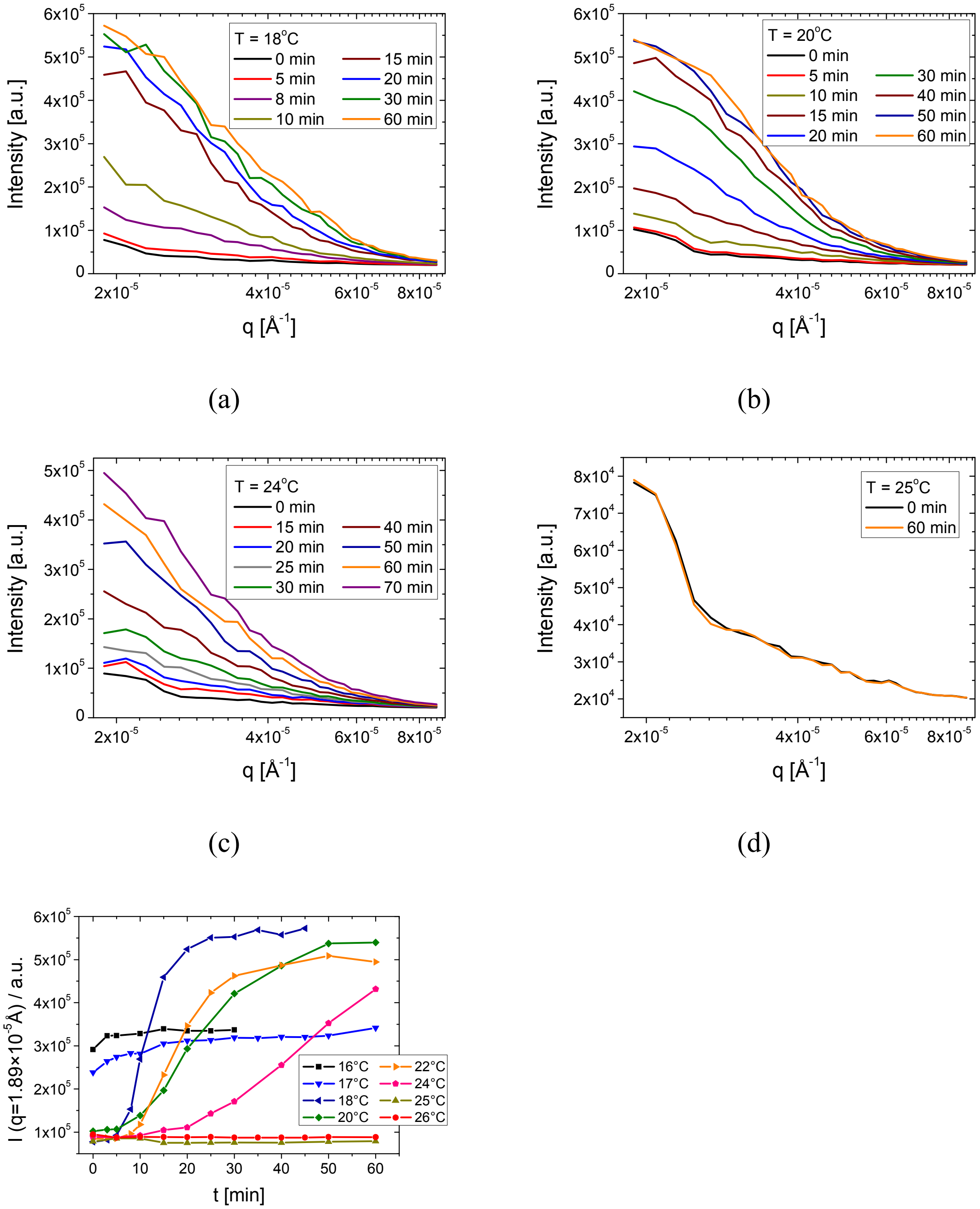

(a)

(b)

(c)

(d)

(e)

Fig.3.13. Exemplary scattering curves obtained from the time-dependent measurements run at temperature: (a) 18°C, (b) 20°C, (c) 24°C and (d) 25°C. (e) Forward scattering intensity vs time.

In figure 3.13.e the intensity at lowest measured angle is plotted versus time. For temperatures lower than 18°C the phase separation appeared immediately after cooling the sample, therefore it is concluded that in this temperature regime spinodal decomposition is taking place. However, in the temperature range 18-24°C an induction time is required for phase separation. That is why in this temperature regime the system is expected to be in the meta-stable state. At higher temperatures the sample stays homogenous in the time frame of the experiment. As it can be seen from the slope of the curves in Fig.3.13.e, at T=24°C it takes more than one hour for the system to reach its final state, for lower temperatures 20-22°C the system decomposes faster (around 30-40 min). At T=18°C the system requires around 20 min to phase separate. In the temperature regime 18-24°C, just after lowering temperature (t=0) the sample was stable for first 5-10min. The value of scattered intensity is the same as for the homogenous sample measured at 25°C and 26°C. At low temperatures 16-17°C the scattered intensity value is higher than for the homogenous sample from the beginning of the measurement, however, it does not reach the value of the final state obtained in the temperature range 20-22°C.

3.4.2. Observation of pressure induced phase separation

In order to study pressure induced phase separation, the measurements were performed for temperatures higher than 30°C because for these temperatures at ambient pressure conditions the system remains homogenous, and therefore possible phase separation will be then a pure effect of pressurizing. The pressure-dependent measurements were done using both, SANS and DLS techniques. In this subchapter their results will be presented.

3.4.2.1. SANS results

In figure 3.14 the scattering curves for this system are shown. The sample was measured at two temperatures: 30°C and 40°C. As can be seen directly from the raw data (see figure 3.14.b), at T=40°C no change in the size of the micelles was observed, as all the scattering curves overlap. At T=30°C, on the other hand, the macroscopic phase separation was observed after applying pressure of around 800bar. A sequential decrease of pressure to 750bar did not stop the progressing aggregation.

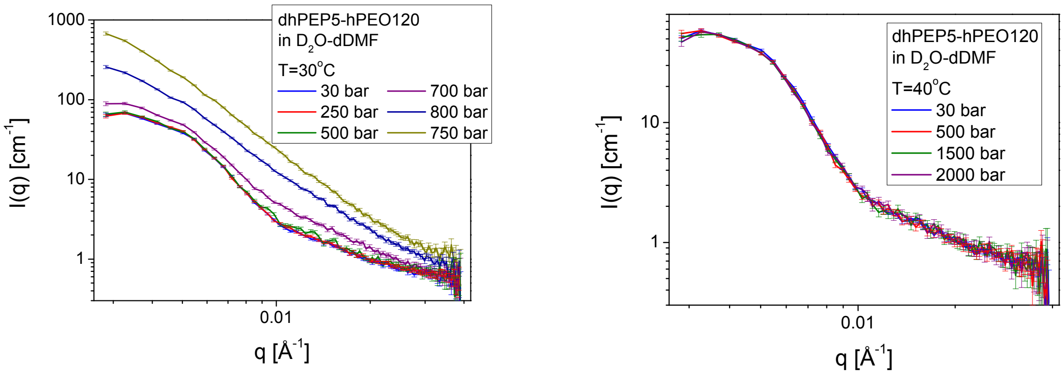

(a) (b)

Fig.3.14. *I(q)* vs *q* for dhPEP5-hPEO120 in D$_2$O-dDMF at: (a) *T*=30ºC, (b) *T*=40ºC.

In this case the core-shell model without any additional contribution was used, as the fit was performed only for the *q*-range up to 0.0095Å, since a proper background correction could not be done (as the scattering of the solvent was not measured). Similarly to the previous fitting procedure, the change of the scattering length density of the solvent due to the change in temperature and pressure was taken into account and the aggregation number, additional radius of the shell (compared to compact) and the smearing parameter of the shell were fitted. The results are given in the figure below.

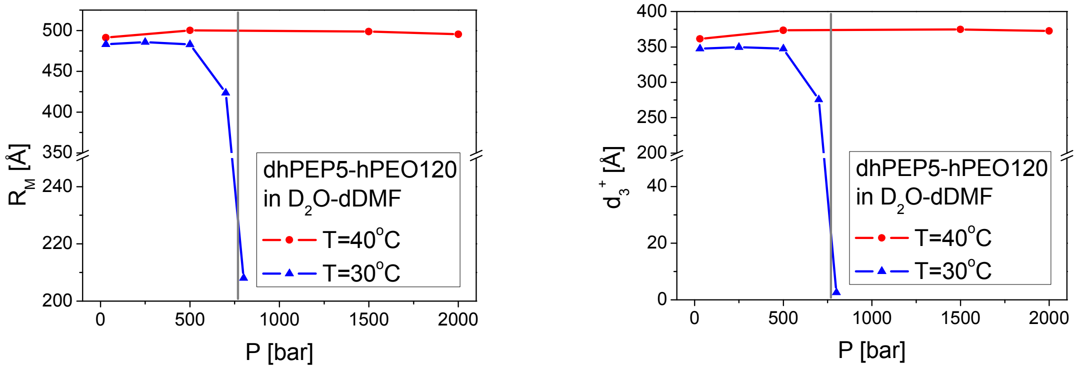

(a) (b)

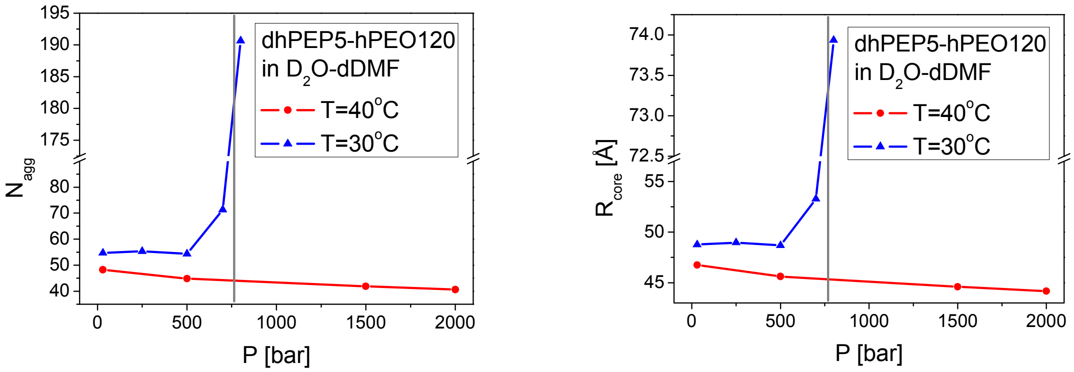

(c) (d)

Fig.3.15. Results of fitting with the core-shell model with the constant background for the dhPEP5-hPEO120 in D_2O-dDMF: (a) overall radius, (b) additional thickness of the shell coming from the presence of the solvent among polymer chains in the micellar corona, (c) aggregation number, (d) the core radius. The locus of the phase separation is marked with a gray line.

No change in the size of the micelle is observed at *T*=30°C up to around 600bar and at *T*=40°C for the full pressure range. Although the aggregation number and the core radius are slightly bigger at 30°C, the overall radius (due to bigger contribution of the additional thickness of the shell, d^{+}_{shell}, to the overall radius) is insignificantly smaller. Application of pressure of around 800bar (at 30°C) induces a phase separation, which is marked in the plots with a gray line.

3.4.2.2. DLS results

The correlation functions for this sample obtained by DLS are presented in figure 3.16. The experiment was done at 35°C, 30°C and 29°C (in this order). At *T*=29°C after applying pressure of 800bar the macroscopic phase separation was observed. The sample became opaque, however not uniformly in the whole volume, as it can be seen from Fig.3.16d. Interestingly, the particles did not start to aggregate immediately after increasing pressure but after around 2 min (which can be seen in Fig.3.16b). Time values are given only as an approximation, as no proper time-dependent measurements were taken. At this point further studies are required. A slight shift toward longer decays times in the correlation functions at temperatures 30°C and 35°C observed within the investigated pressure range is due simply to change of the viscosity and refractive index of the solvent. The difference of one degree in the temperature, at which the phase separation appears in SANS and DLS lies in the error range and also might come from the fact that two different pressure cells are used in both experiments: the thermoelement mounted in the cell for the light scattering is much closer to the sample (and gives the uncertainty of temperature measurement of ΔT=0.5°C) than the one used in the cell for SANS experiment (which gives the error of around 1°C).

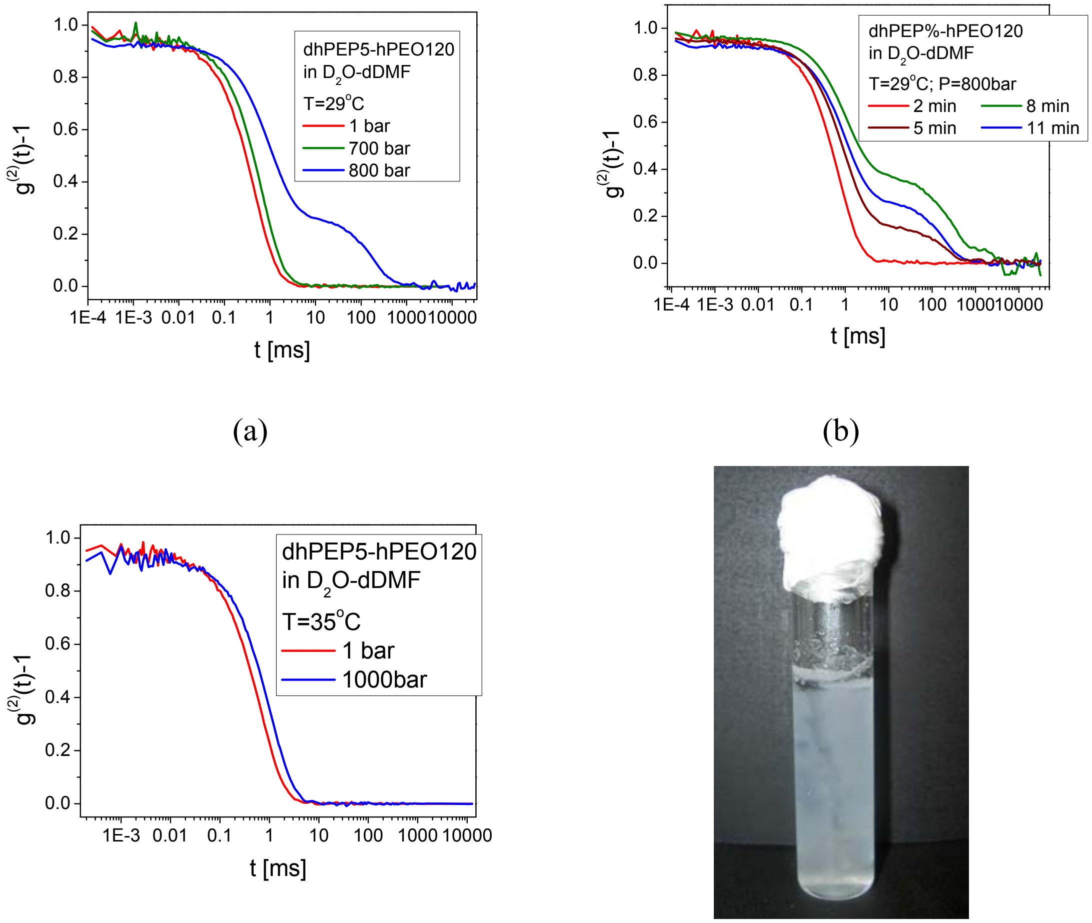

(a) (b)

(c) (d)

Fig.3.16. The correlation functions for dhPEP5-hPEO120 in D_2O-dDMF at: (a) and (b) T=29ºC, (c) T=35ºC; (d) picture of the sample after applying 800bar at T=29ºC.

In order to calculate the hydrodynamic radius of the micelles, the changes in the refractive index and viscosity of the solvent due to the application of pressure were taken into account. All the correlation functions obtained for the homogenous solution were easily fitted with one-exponential decay function. In figure 3.17 the resulting hydrodynamic radius is plotted versus pressure for each temperature.

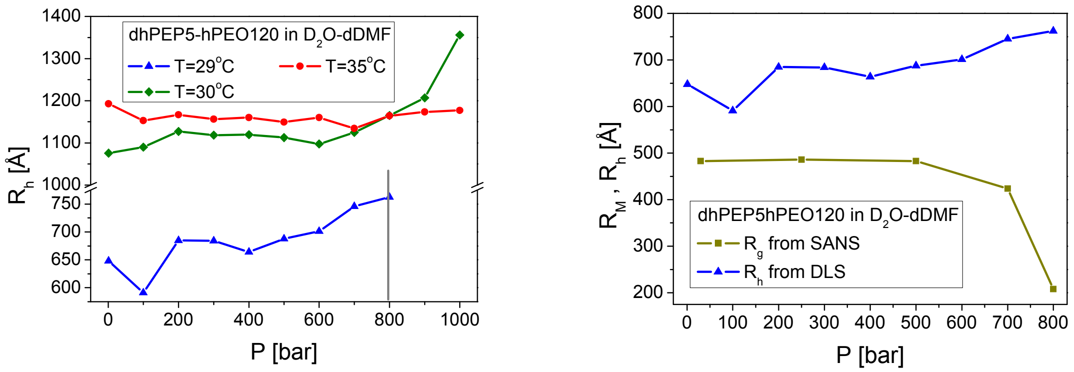

(a) (b)

Fig.3.17. (a) The hydrodynamic radius, R_h, received from the DLS measurement, (b) comparison of R_h (at T=29°C) with R_M (at T=30°C) obtained from fitting the SANS data. The gray line indicates the pressure (for T=29°C) at which the phase separation appears.

First observation similar in both, DLS and SANS, results is that while lowering temperature, the radius of micelles decreases. Here, the hydrodynamic radius decreases from R_h≈1160Å at T=35°C to R_h≈1120Å at T=30°C, and eventually to 650Å at T=29°C.

When it comes to pressure-dependency of hydrodynamic radius, at temperatures higher than 30°C no change in the micellar size was observed in both experiments. This is similar to the findings for polystyrene of R. L. Cook *et al.* [75], that the radius of gyration is invariant with pressure for the polymeric solution in the organic solvents. At T=30°C applying of pressure up to P=600bar does not change the radius. Further increase of pressure causes increase of R_h up to around 1350Å at P=1000bar. At even lower temperature (29°C) increase of the pressure entails the increase of the radius until the aggregation appears.

Comparing this with the SANS results (see Fig.3.17.b) it can be seen that pressure application does not influence the size of the micelle. It does induce, however, phase separation, which appears in the DLS experiment as aggregation of micelles (radius becomes bigger while pressurizing at *T*=29°C). In the SANS measurement it appeared as a collapse of the micelle (radius becomes smaller while pressurizing at *T*=30°C). Due to the limits in the *q*-range in the SANS experiment, it was not possible to determine the size of the aggregates. Comparing the values of hydrodynamic radius at *T*=29°C and overall micellar radius of gyration at *T*=30°C, both at ambient pressure, gives the ratio $\frac{R_h}{R_g} \approx 1.34$, which is close to predicted value of 1.29 for spherical systems.

3.4.3. Observation of pressure induced phase separation in solution of homopolymer PEO150 in D_2O-dDMF

In order to understand the structural and phase behaviour of a micelle the structural evidence for the pure polymers that builds the aggregate is needed. Here the results of measurement of the homopolymer PEO (of a similar molecular weight to the one in the copolymer that forms micelles) are presented. In figure 3.18 the SANS scattering curves for the polymer hPEO150 in D_2O-dDMF are shown. The sample was measured at the same temperatures: 30°C and 40°C. Similarly to the previous results for the dhPEP5-hPEO120 micelles in the same solvent, it can be seen directly from the raw data that all the scattering curves overlap at *T*=40°C and so no change in the size of the polymer coils was observed. At *T*=30°C, on the other hand, the macroscopic phase separation was observed after applying pressure of around 800bar. Visual inspection through the pressure cell windows showed that a “needle”-shaped object was formed from the aggregating polymers.

The experiment was done as follows: first the sample was measured at *T*=40°C, then it was cooled down to *T*=30°C and the first set of measurements was taken; when the phase separation appeared, pressure was deceased to *P*=500bar, the sample was held at this pressure level and warmed up to 40°C. It took around 10min to increase the temperature, and then it was staying at 40°C for the next 20 min. After that, the temperature was again decreased (within around 10min) to 30°C in order to repeat the measurement. The sample was held at these conditions (T=30°C, P=500bar) for the next half an hour in order to make sure that we reached the state at the beginning of the measurement. As it can be seen from Figure 3.18c, after 26min of warming up the sample reached its beginning state. The difference between first and the second set of measurements can be seen for at P=800bar: in the first one – the increase of the pressure form 700 to 800bar results in the increase of the intensity at small q from around 0.9 to 5.8cm^{-1}. In the second one the increase of the pressure form 750 to 800bar results in the increase of the intensity at small q from around 0.9 to 1.3cm^{-1}. This difference can be explained by the time dependency of the phase separation process that was observed for the micellar system in the same solvent using DLS (see Fig.3.16.b)

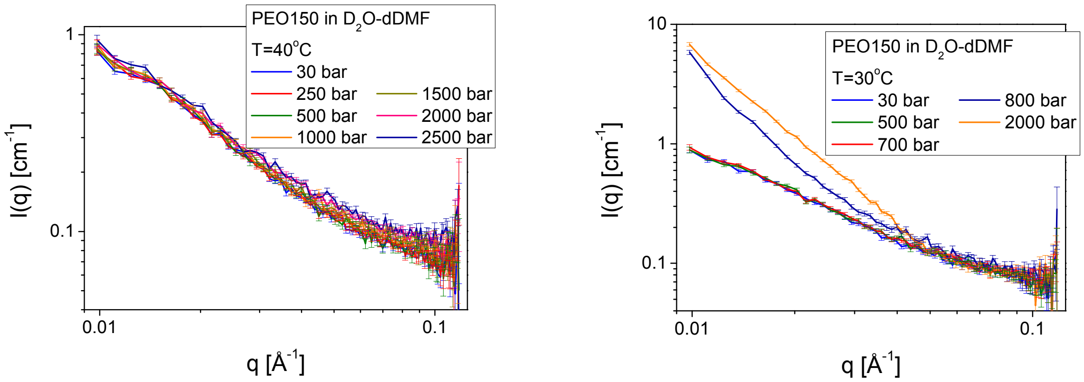

(a) (b)

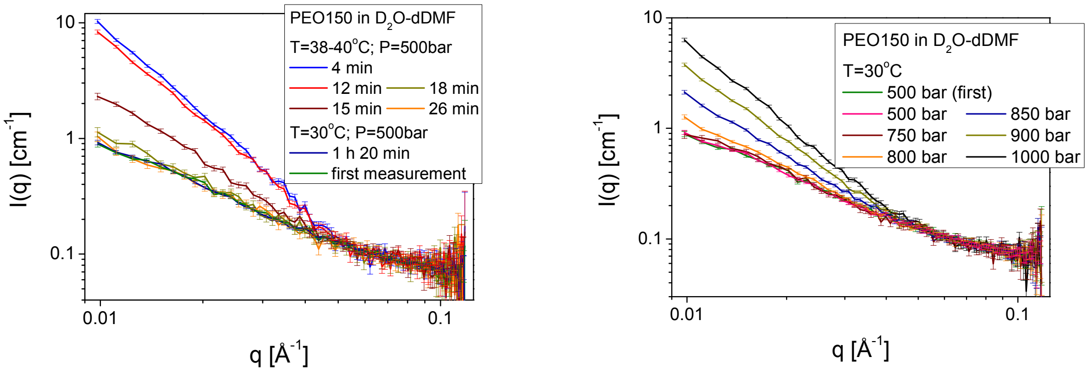

(c) (d)

Fig.3.18. I(q) vs q for hPEO150 in D$_2$O-dDMF at: (a) T=40ºC, (b) and (d) T=30ºC, (c) warming up of the sample.

Here, the determination of the radius of gyration will be given. It can be obtained simply using the Zimm approximation:

$$\frac{1}{I(q)}=\frac{1}{I(q=0)}\left(1+\frac{R_g^2q^2}{3}\right), \qquad \text{(Eq.3.26.)}$$

where both parameters, forward scattering intensity $I(q=0)$ and radius of gyration R_g were fitted.

On the other hand, this can be compared with:

$$\frac{1}{I(q)}=\frac{M}{cK^2V^2}\left(1+\frac{R_g^2q^2}{3}\right)\left(1+2A_2Mc\right), \qquad \text{(Eq.3.27.)}$$

where: c is the concentration of the polymer solution, K – the contrast (the difference in scattering length density between the particle and the solvent), V – the polymer volume [96]. Assuming no interactions between particles (second virial coefficient, A_2=0; very dilute solution), one can estimate $I(q=0)$. This way it is possible to check if the data reduction and the fitting were done properly. For the investigated PEO solution, the value of intensity at q=0 from Eq.3.27 it is expected to be around 1.47cm^{-1}, taking the molecular weight of around 130kg/mol, obtained from GPC, the polymer density of 1.125g/cm^3, and the scattering length densities ρ_{hPEO}=6.37·10^{9}cm^{-2} of the polymer and ρ_0=6.34·10^{10}cm^{-2} of the solvent. Fitting the scattering curves from SANS experiment with the Zimm function (Eq.3.26) gave us the value of *I(0)* always around the expected one, which ensures that the fitting procedure was done correctly and moreover, the values of radius of gyration obtained from the fitting procedure are correct.

The results are shown in figure 3.19. Although it was still possible to fit the data for P=800bar at T=30°C with the Zimm function, it cannot be taken into account, as here the phase separation appeared and the approximation A_2=0 is not valid anymore, and the $I(q=0)$ was twice bigger than the one predicted from Eq.3.27. Similarly to the results for the dhPEP5-hPEO120 micelles in the same solvent, there is no change in the radius of gyration until the phase separation occurs.

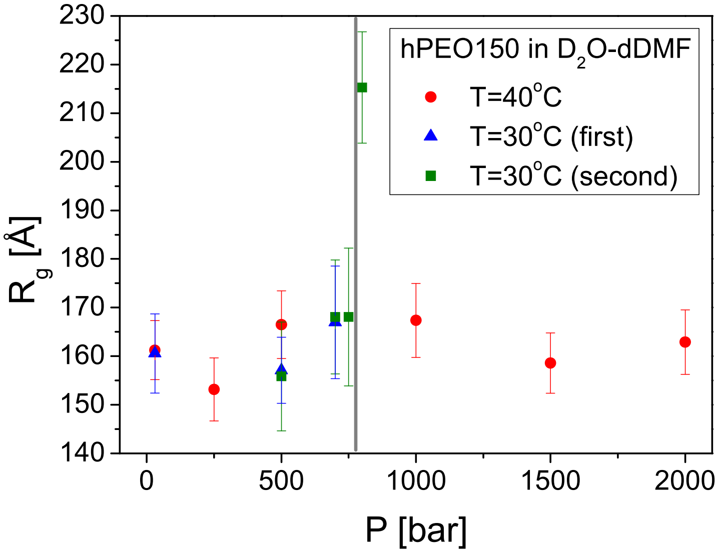

Fig.3.19. The radius of gyration, R_g, plotted versus pressure. The gray line indicates the pressure (for T=30°C) at which the phase separation appears.

3.5. Discussion

In this subchapter the discussion of the results for the temperature- and pressure-dependent behaviour the dhPEP5-hPEO120 micelles in both solvents will be given for, respectively, the water dispersion and the water-DMF mixture.

3.5.1. Temperature- and pressure-induced shrinkage of dhPEP5-hPEO120 in D_2O

For the investigated water dispersion, the gyration and hydrodynamic radii were estimated using light and neutron scattering techniques at ambient conditions (T=20°C, atmospheric pressure). The results are summed up in the table below.

Table 3.6. The values of gyration and hydrodynamic radii of dhPEP5-hPEO120 micelles in D_2O at T=20°C and ambient pressure obtained from SANS, SLS and DLS experiments.

experimental technique	radius of gyration, R_g [Å]	hydrodynamic radius, R_h [Å]	volume fraction, Φ [%]
SANS	686	–	0.33%
SLS	521	–	0.066%
DLS	–	835	0.066%

The difference in the resulting values of gyration radius from SANS and SLS is due first of all to different fitting models that were used. SANS data was modeled with core-shell and Beaucage functions, and SLS data was fitted using Guinier approximation (first term in Beaucage model, see Eq. 3.23). The other reason lies in different origin of scattering process while using light and neutrons as incident beams. Light is scattered due to local fluctuations in the dielectric constant of particles, whereas neutrons are scattered at the nuclei of atoms. What differs both techniques is also the issue of contrast between the polymer chains and the solvent. In light scattering experiment contrast comes from the difference in refractive indices of particles and solvent. When this difference is too small, no (or very weak) intensity fluctuations will be recorded, but in case it is too big, sample appears opaque, which spoils the experiment. At ambient conditions the refractive index of the polymer (PEO) is 1.4539 and the refractive index of solvent (D_2O) is 1.3284. It was found out that the dilution was required in order to receive transparent sample. On the other hand, in neutron scattering experiment the contrast is determined by the difference in scattering length densities of solute and solvent. At ambient conditions the values of scattering length density are $6.37 \cdot 10^{9}$cm^{-2} for PEO and $6.37 \cdot 10^{10}$cm^{-2} for D_2O.

This difference of one order of magnitude is an advantage in neutron scattering experiment and therefore makes this technique more suitable for investigation of this system, and the results more trustworthy.

The relation of both radii, gyration and hydrodynamic, from light scattering experiments was found to be $\frac{R_h}{R_g} \approx 1.6$, and comparison of hydrodynamic radius with the overall micellar radius from SANS gives the ratio $\frac{R_h}{R_M} \approx 1.22$. The later is close to the expected value (around 1.29) for spherical objects.

Comparing these results with previous findings of Willner *et al.* [97] for exactly the same polymeric micelles, one sees big discrepancy, although the same model (core-shell geometry) was used to fit the SANS data, see table 3.7. The aggregation number is an order of magnitude smaller than the one obtained by Willner *et al.* [97], and both radii, R_{core} and R_M are around twice smaller. The possible explanation of such a big disagreement lies in the aging of the sample (one has to note that here exactly the same diblock copolymer was used 10 years after experiments performed by Willner *et al.* [97]), however, the recent GPC test did not reveal sufficient change in molecular weight of the block copolymer.

Table 3.7. Comparison of the micellar characteristic with the results of Willner *et al.* [97].

N_{agg}	R_{core} [Å]	R_M [Å]	source
67	52	686	here
870	120	1170	Willner *et al.* [97]

Coming to the temperature- and pressure-dependence of the investigated system in water, a decrease in the overall micellar radius, R_M, was found using SANS technique. The biggest contribution to the overall radius is due to the additional thickness of the shell, d^{+}_{shell}, which represents the thickness of the shell compared to the compact one. In other words, it includes presence of the solvent among polymer chains building the micellar corona. Its temperature- and pressure-dependent behaviour is in agreement with the previous findings [51-[60] about breaking of hydrogen bonds between water molecules and the oxygen atoms in the polymer chains while heating up or pressurizing the sample, which causes coiling of the polymer. Further increasing temperature to LCST (around 100°C) would cause phase separation. Cooling the system below the room temperature (the measurement at T=9°C) still leads to swelling of the micellar corona, but the difference between the values of R_M and d^+_{shell} measured at 9°C and 20°C is not significant. This is in agreement with the reduction of the solvent quality of water for PEO below room temperature, as reported in [59]. It can be assumed that for even lower temperatures the swelling of PEO chains will be suspended and eventually the phase separation will be observed after crossing the upper critical solution temperature (UCST). Contrary to the micellar radius and d^+_{shell}, the aggregation number increases while heating up and at lower temperatures (9°C) it increases also with pressurizing. The core radius, which depends solely on N_{agg} (see Eq.3.20), does not change significantly with temperature (from 50Å at T=9°C to 57Å at T=70°C) and pressure, as it depends on aggregation number as a cubic root. However, a small increase while heating can be observed, and at lower temperatures (9°C) it increases also with pressurizing. This is in a contradiction with previous studies [73,[98,[99], which have shown that the PEP-PEO micelles in water are kinetically frozen (no unimer exchange between micelles was noted even at high temperatures and for long time observations). Here it was found that the value of N_{agg} in the temperature range 9-70°C varies of around 30%. This inconsistency can be decided by performing SANS experiment in so-called core contrast, where the mixture of the protonated and deuterated solvents (in this case H_2O and D_2O) is prepared that the scattering length densities of polymer building the corona block and the solvent are equal ($\rho_{hPEO} = \rho_{solvent}$). Under these conditions the scattering signal comes only from the micellar core and its possible change in size and composition induced by the variation of temperature and pressure can be obtained straightforwardly.

Another feature of the temperature- and pressure-dependent behaviour of this dispersion is that there is no straightforward dP/dT relation as it was observed for the sticky hard sphere system investigated by Vavrin *et al.* [17]. To test the dP/dT proportionality, a 2nd polynomial fit, $R_M = A + B_1 \cdot P + B_2 \cdot P^2$ was performed for the values of the overall micellar radius measured at each temperature, which is shown in Fig.3.20 as red lines.

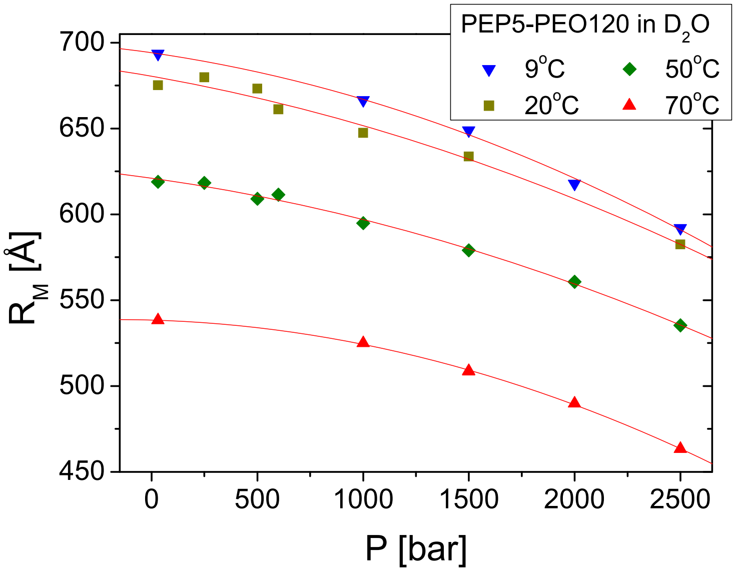

Fig.3.20. The 2nd polynomial fit (red lines) of the pressure-dependency of the overall micellar radius.

The resulting values of the coefficient B_1 and B_2 are given in the table below. At intermediate temperatures (20 and 50°C) the absolute value of B_2 coefficient is smaller than at 9°C and 70°C. On the other hand, the absolute value of the coefficient B_1 increases while lowering temperature from 70°C to 20°C, and then decreases again while cooling below room temperature.

Table 3.8. Coefficients from 2nd polynomial fit of the pressure-dependent R_M values for temperatures: 9, 20, 50 and 70ºC.

	A [Å]	B_1 [Å/bar]	B_2 [Å/bar^2]
9ºC	694.14025	-0.01779	$-9.3937 \cdot 10^{-6}$
20ºC	680.36538	-0.02171	$-6.97517 \cdot 10^{-6}$
50ºC	621.05358	-0.01736	$-6.72136 \cdot 10^{-6}$
70ºC	538.51134	-0.00374	$-10.4969 \cdot 10^{-6}$

The complex *dP/dT* relation can be also seen in Figure 3.9.f, where the temperature and pressure conditions at equal micellar radius are given. Also here, there is no linear relation. The micelles, unlike the octadecyl grafted silica particles, are more complex system, and its response will come from the reaction of both polymers, PEP and PEO, to the change of temperature and/or pressure. One should distinguish two contributions to the temperature and pressure behavior. Firstly, at higher temperatures and elevated pressure water becomes a poorer solvent for PEO, which causes coiling of this polymer, and hence a decrease in the micellar radius. Secondly, interfacial tension between PEP and water increases, which then results in bigger N_{agg} and formation of bigger micellar core, and hence R_{core} increases. As the PEO chains are much longer than PEP in this system, the effect of folding of PEO and its influence on the overall micelar radius will be more pronounced. Hence, the first contribution dominates the behaviour of PEP-PEO. Applying pressure acts as increasing temperature, causing a decrease of the micellar radius.

On the other hand, the shrinking of the micelles was not observed in the DLS measurement, but there are difficulties with interpreting this data set as the solution is highly polydisperse so that the resulting values of hydrodynamic radii were obtained with uncertainty of more than 10%.

3.5.2. Temperature- and pressure- induced phase separation of dhPEP5-hPEO120 and hPEO150 in D_2O-dDMF

The temperature at which phase separation occurs at ambient pressure conditions was determined by performing SALS experiment. It was found that for temperatures lower than 18°C the sample undergoes a demixing process immediately after cooling, while in temperature range 18-24°C it appears after certain time, and the higher the temperature is, the longer it takes for the system to phase separate. At 25°C the system becomes stable. The measurement at atmospheric pressure was done in order to find the temperature range in which the system is stable, so that the pressure-dependent experiment will be run in this regime. Then the possibly observed phase separation will be induced solely by pressure.

In pressure-dependent SANS and DLS experiments for the investigated systems in equi-molar D_2O-dDMF mixture we observe firstly, that the overall radius of micelles in this solvent is smaller than in water solution, which is related to the compatibility of both polymers, PEP and PEO, with DMF. Secondly, until the phase separation no change in radius of micelle or polymer coil occurs while applying pressure. For both systems, PEP-PEO micelles and PEO homopolymer, phase separation sets in at the same temperature and pressure conditions. Moreover, pressure induced phase separation does not set in immediately, as it was shown with the DLS measurement (Fig.3.16.b), where the second decay of the correlation function, corresponding to the diffusion time of formed aggregates, appears only a few minutes after applying pressure. Finally, the other feature obtained from the SANS measurement (see Fig.3.14.a) is that once phase separation sets in, lowering of pressure will not reverse the demixing process. The sample was brought back to the homogenous state by raising the temperature. In this subchapter, the comparison of the results of the both systems, PEP-PEO micelles and PEO homopolymer, will be given, and the observation of the phase separation will be discussed.

As already mentioned in chapter 3.1, the addition of DMF results in a substantial decrease of the interfacial tension between PEP and the solvent. This causes reduction of the aggregation number as compared to that in pure water [73]. For the micelles in water-DMF the aggregation number in the range of N_{agg}=40-50 was found at T=40°C and $N_{agg}\approx55$ at T=30°C (before the phase separation set in). Micelles in pure water have the aggregation number in the range of N_{agg}=70-80 in the temperature range of 20-50°C. This is in agreement with the results of Lund *et al.* [73]. The previous studies [73,[98,[99] on the PEP-PEO system in water-DMF mixtures reveal the unimer exchange process at higher temperatures, during which the equilibrium structure was maintained [98]. However, in the experimental conditions applied here, the presence of exchange process is not expected and therefore, no change in the aggregation number should be observed. As expected, N_{agg} is only slightly smaller at T=30°C than at 40°C, which is due to small decrease of the interfacial tension between PEP and the solvent with increasing temperature. It stays unaffected by the application of pressure until phase separation sets in.

On the other hand, the addition of DMF causes also the shrinking of the corona comparing to the one in pure water solution [73]. The theory of starlike micelles predicts the dependence of the corona thickness $D = R_M - R_{core}$ on aggregation number:

$$D \sim {N_{agg}}^{1/5} {N_A}^{3/5}. \qquad \text{(Eq.3.28.)}$$

Compensating the reduction in corona size for the reduction in N_{agg} (which was done by scaling D by ${N_{agg}}^{1/5}$ according to Eq.3.28), revealed the relative shrinkage of about 20% for the PEP1-PEO20 micelles [73]. For the system investigated here, which is even more asymmetric while the fraction of PEO compared to PEP chains is even higher, the drop in $D / N_{agg}^{1/5}$ from pure water to water-DMF solution is also expected. One cannot make a direct comparison as both samples were measured at different temperature conditions. Nevertheless, for micelles in pure water at ambient pressure $D / N_{agg}^{1/5}$ stays in the range of 265-235Å in the temperature range of 20°C-50°C, whereas for the same system in water-DMF mixture $D / N_{agg}^{1/5}$ has the value of 195-208Å in the temperature range 30°C-40°C. On average it gives also the drop in $D / N_{agg}^{1/5}$ of around 20% from pure water to equi-molar water-DMF solution. The contribution to the overall micellar radius coming from PEO chains does not change the overall micellar radius with pressure, which means that pressurizing of the sample up to 2500bar at 40°C and up to 700bar at 30°C does not influence the conformation (size) of the PEO coils. This was confirmed by the reference measurement of the PEO homopolymer of similar molecular weight to the one in the block copolymer. It proved that the PEO polymer size stays unchanged under the pressure up to 2500bar at 40°C and up to 700bar at 30°C.

Second remark is related to the unchanged radii of PEP-PEO micelles and PEO homopolymer under action of pressure until phase separation sets in. This is different from the observation of micellar radius in water solution, where the decrease in the radius was observed while approaching LCST. This difference is probably due to the micellar conformation in both solvents. In water, which is good solvent for PEO, the micellar corona is swollen. Hence, changes in solvent quality will be easily seen in the decrease of the corona thickness and therefore, in the micellar radius. In water-DMF solution, which is poorer solvent for PEO than water, the micellar corona is more compact. That is why any change in its thickness or overall micellar radius is harder to be observed.

For the homopolymer we observed the phase separation at exactly the same temperature and pressure conditions as for the micelle system, which means that phase transition of the micellar system is governed by PEO behaviour. In future, the kinetics of the phase separation can be studied more extensively, as it was shown here that it does not appear immediately after pressurizing. Because it takes a few minutes after applying pressure, it is rather hard to investigate it in details with SANS technique, as within this time interval data is usually accumulated and thus averaged. In order to have better time resolution, the so-called pressure jump technique can be used. In this mode after applying pressure, scattered intensity is recorded in short time-slices. This procedure is repeated several times and eventually the signal from each short time range is averaged from all repetitions.

3.6. Conclusions

To conclude, the behaviour of the PEP5-PEO120 micellar system in pure water and equi-molar water-DMF mixture is governed mostly by the contribution coming from the reaction of PEO chains to the change of temperature, pressure or solvent composition.

Temperature- and pressure-dependent shrinking of micelles in water is attributed to a decrease of the solvent quality of water for PEO. As the investigated micelles are highly asymmetric and consist mainly of PEO, its reaction to the variation of temperature and pressure shields the contribution coming from PEP behaviour in water.

The micellar radius of the same system in the water-DMF solution did not change while pressurizing until a phase separation appeared. We think this is due to the fact that addition of DMF to the solvent caused formation of smaller and very compact micelles.

This has two causes: firstly, the interfacial tension between PEP and the D_2O-dDMF solution is much smaller than for pure water, and secondly, presence of DMF decreases the solvent quality for PEO and result in coiling of the polymer. The phase separation did not take place immediately after applying certain pressure but it occurred after a few minutes.

In the case of PEP-PEO micelles in water applying pressure has similar effect as increasing temperature, although there is no simple linear dP/dT relation. In the case of PEP-PEO micelles in water-DMF solution applying pressure acts as lowering of temperature.

In future work the attention could be paid to the kinetics of phase separation under pressure and the attempt to determine the dP/dT relation could be made. Having characterized the effect of temperature and pressure on the form of single micelles, we can now also start to study the effect of these parameters on concentrated solutions.

PART II

4. The temperature dependence of the poly(ethylene-*co*-propylene) (PEP) copolymer macroscopic viscosity studied by Fluorescence Correlation Spectroscopy (FCS)

4.1. Introduction

There is an ongoing discussion on the problem of nano- and macroviscosity of polymer solutions. The type of measured viscosity depends on the size of the particles probing polymer solutions: while diffusing, small objects (of sub-nanometer size) are expected to experience the viscosity of a solvent in which the polymer is dispersed, whereas the diffusion of objects larger than the polymer size is supposed to depend on the macroscopic viscosity of the whole solution. As it was found by Holyst *et al.* [100], the length scale at which the crossover from nano- to macroscopic viscosity is observed is related to the polymer radius of gyration.

The goal of these experiments was to find the correlation between temperature dependency of: the polymer macroscopic viscosity and the diffusion time of a nanoscopic probe diffusing between the polymer chains, using a temperature cell combined with the Fluorescence Correlation Spectroscopy (FCS) setup. In the work of Holyst *et al.* [100] the viscosity of the polymer dispersion was changed by varying the polymer concentration. It can be also done using temperature as variable. In FCS technique the self diffusion time of fluorescent (or fluorescently labeled) particles is measured. Determining the size of the confocal volume by measuring diffusion time of a standard sample (for example rhodamine), the diffusion coefficient of the investigated sample can be obtained. If the Stokes-Einstein (Eq.3.11 and 3.12) relation is valid for a measured system, the diffusion time obtained in FCS experiment can be used to calculate the dispersion viscosity.

Here, the temperature dependent diffusion times of a fluorescent dye, rubrene, dissolved in a poly(ethylene-*co*-propylene) copolymer were investigated. In this case there is no solvent used, rubrene is diffusing only among polymer chains. Therefore the variation of diffusion times with temperature is expected to depend solely on the temperature induced changes in the macroscopic viscosity of the polymer.

4.2. Experimental section

4.2.1. Materials

The poly(ethylene-*co*-propylene) copolymer PEP6, provided by Lutz Willner and Jürgen Allgaier, was used. The number denotes approximated molecular weight in kg/mol. The details of the synthesis procedure were published elsewhere [79]. This particular polymer was chosen because of its low glass transition temperature, $T_g = -62°C$. The fluorescent dye rubrene (5,6,11,12-tetraphenylnaphthacene; Sigma Aldrich R2206), which structure is schematically shown in Fig.4.1.a, was used in the experiment. The absorption and fluorescence spectra of 20μM solution of rubrene in cyclohexane at room temperature taken from Bayrakçeken [102] are given in Fig.4.1.b as an example. The size of rubrene (the length of the tetracene backbone) molecule is of order of 1nm.

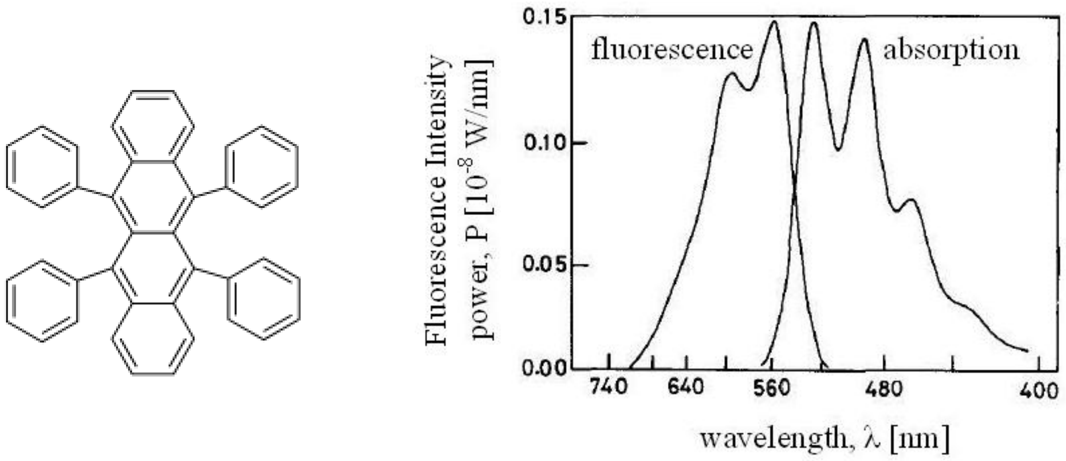

(a) (b)

Fig.4.1. (a) Rubrene structure [101]; (b) absorption and fluorescence spectra of Rubrene in cyclohexane at room temperature [102].

In order to prepare the 1nM solution of rubrene in PEP6 first 1g of PEP6 was dissolved in toluene and 0.053g of rubrene, which would correspond to 0.1mM concentration in PEP6, was also dissolved in toluene. The solution of rubrene in toluene was then diluted gradually to obtain the amount of rubrene that would correspond to 1nM concentration. This final solution of rubrene in toluene was then added to PEP6 in toluene and mixed using magnet stirrer while keeping the sample on heating plate in order to let the toluene evaporate. In order to remove the toluene properly, the sample was kept in a vacuum oven (Heraeus vacutherm).

4.2.2. Viscosity measurement

The viscosity measurements of: the investigated sample consisting of PEP6 polymer with addition of 1nM concentration of the fluorescent dye rubrene, and the pure polymer PEP6 were performed using the commercial rheometer Physica MCR 501 (Anton Paar). The viscosity was measured in the temperature range 0-70°C in steps of 5°C at shear rates of 0.01-1s^{-1}, at 3 points per decade. This low shear rate range was chosen in order to obtain the zero shear viscosity, defined by:

$$\eta_0 = \lim_{\omega \to 0} \frac{G''}{\omega}, \qquad \text{(Eq.4.1.)}$$

where G'' is the dynamic loss modulus and ω – the angular frequency.

Caution has to be taken concerning the measuring time. In order to be sure that the viscosity reaches a stationary value the measuring time per data point has to be long enough. Here it was set to 60 seconds. The temperature scan was done both ways: by warming up and cooling down the samples in order to check if any change in viscosity depending on the way of varying temperature will be observed. Before starting any new measurement there was given 10 minutes of a waiting time for the sample to equilibrate after each change of the temperature. The results are presented in Fig.4.2.

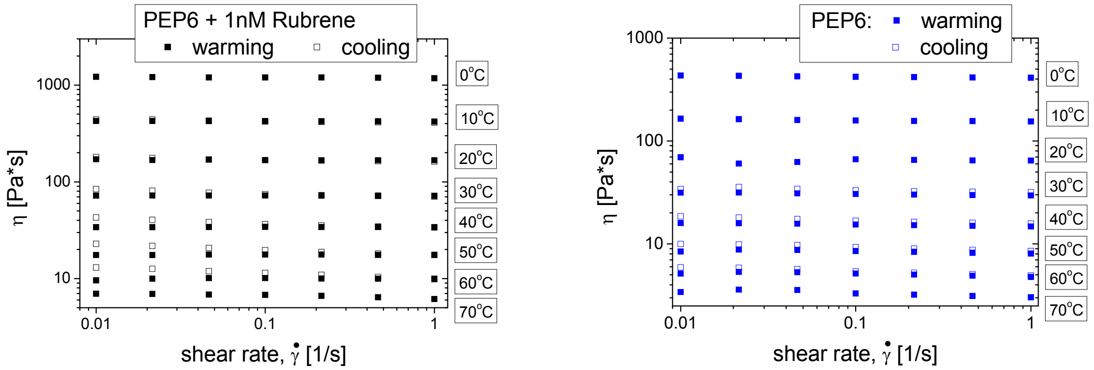

(a) (b)

Fig.4.2. Results of the zero shear viscosity measurement of: (a) the sample consisting of PEP6 and rubrene used in diffusion time measurement (using FCS technique) and (b) the pure polymer PEP6.

In the chosen shear rate regime the values of the viscosity at each temperature are constant. This is the proof of obtaining zero shear viscosity values.

4.2.3. Fluorescence Correlation Spectroscopy (FCS)

In FCS experiments the temporal fluctuation of the fluorescence intensity, *δI(t)*, are measured. These fluctuations arise from the fluctuations in the quantum yield of a dye or from the constant motion of fluorescent molecules in the observation (confocal) volume. Here, the later will be discussed. The fluctuations of the fluorescence intensity at any arbitrary time t are analyzed with respect to its self-similarity after the lag time, τ, in the form of autocorrelation function:

$$G(\tau) = \langle I(t)I(t+\tau) \rangle = \lim_{T\to\infty} \frac{1}{2T} \int_{-T}^{T} \langle I(t)I(t+\tau) \rangle dt \qquad \text{(Eq.4.2.)}$$

Here, *I(t)* denotes the collected fluorescence intensity, <*I*> its mean value and *δI(t)* the deviation from the mean value. The definition of the autocorrelation function is given for one particular interval τ, but the complete autocorrelation function specifies *G(τ)* for every τ. The fluorescence intensity at certain time t can be written as $I(t) = I + \langle \delta I(t) \rangle$, therefore the autocorrelation function:

$$G(\tau) = \langle I \rangle^2 + \langle \delta I(t) \delta I(t+\tau) \rangle \qquad \text{(Eq.4.3.)}$$

has a constant term $\langle I \rangle^2$ and a time dependent part, which contains information about the kinetics of a chromophore in an investigated sample. In the fitting program for data analysis the autocorrelation function is given in the normalized form:

$$\hat{G}(\tau) = \frac{G(\tau)}{\langle I \rangle^2} = 1 + \frac{\langle \delta I(t) \delta I(t+\tau) \rangle}{\langle I \rangle^2}. \qquad \text{(Eq.4.4.)}$$

Assuming the separation of fluorescence time τ_F and translational diffusion time τ_D ($\tau_F \ll \tau_D$, which usually is the case), the contribution of the translational self diffusion to the autocorrelation function is described as:

$$\hat{G}(\tau) = 1 + \frac{1}{N}\left(1 + \frac{4D\tau}{\omega_{xy}^2}\right)^{-1}\left(1 + \frac{4D\tau}{\omega_z^2}\right)^{-1/2}, \qquad \text{(Eq.4.5.)}$$

where ω_{xy} and ω_z denote the distances from the centre of the laser beam focus in the radial and axial direction, respectively, at which the detected fluorescence intensity drops by a factor of e^2 compared to its peak value. The ratio ω_z/ω_{xy} describes the shape of the observation volume and is called the structure parameter. In Eq.4.5, N is the mean number of labeled particles within the observation volume (equal to $\pi^{3/2}\omega_{xy}{}^2\omega_z$), and D stands for the translational self diffusion coefficient of the fluorescent molecules equal to:

$$D = \frac{\omega_{xy}^2}{4\tau_D}, \qquad \text{(Eq.4.6.)}$$

where τ_D is the self diffusion time (the decay time of the autocorrelation function). Here, the rotational diffusion is omitted because it plays a role for rod-like particles and the fluorescent dye used in the experiment, rubrene, has a round shape. Analysis of the rotational diffusion can be found elsewhere [103].

So far, it was assumed that the fluorescent properties of the chromophore do not change while traversing the laser focal volume, which does not hold for real dyes and higher excitation powers, as the molecules can enter and leave their triplet state. The chromophore needs comparably long time to relax back from the triplet to the ground state. During this time, the dye cannot emit any fluorescent light and appears dark. The intra- and intermolecular reactions giving rise to fluorescence fluctuations happen in the time-scales much faster than the diffusion of particles. Therefore, a simple separation of the dynamics is possible, and it leads to the autocorrelation function form of:

$$G_{total}(\tau) = G_D(\tau)\left[1 - T + T\exp\left(-\frac{\tau}{\tau_T}\right)\right], \qquad \text{(Eq.4.7.)}$$

where $G_D(t)$ is expressed by Eq.4.5, T refers to the fraction of particles that are in the triplet state, and τ_T is the triplet state life-time. The more detailed description can be found elsewhere [104]. The presence of triplet states was taken into account in the fitting procedure in the FCS data analysis.

The experiments were performed using a commercial FCS spectrometer ConfoCor 2 (Zeiss, Jena, Germany). It is shown schematically in Fig.4.3, and the main modules it consists of are: the laser unit, the avalanche photodiode detector box, the detection unit with the high numerical aperture objective and a PC with the software controlling the machine operation, collecting and analyzing data. The three lasers give the possibility of choosing excitation length: the argon-ion laser (Spectra Physics, emission lines at 458nm, 488nm and 514nm, maximal power 25mW, water cooled) and two helium-neon lasers (Spectra Physics, λ=543nm, 5mW and Spectra Physics, λ=633nm, 15mW). The helium-neon laser was used in the experiment with the wavelength of λ=543nm and 70% excitation transmission. Detection unit contains the main parts for illumination with laser light and for the detection of the fluorescence light. A parallel beam from collimator is reflected by the main beam splitter and guided to the microscope to the high aperture objective, which collects also the fluorescent light emitted by molecules in the sample. The focal spot size is in the femtoliter volume range. Fluorescent light (marked with red lines in Fig.4.3) with a longer wavelength than the excitation light (marked with blue lines in Fig.4.3) can pass the main beam splitter (dichroic mirror), which blocks all reflected excitation light. The pinhole optics (a high corrected lens) focuses the fluorescent light from the focus image of the sample onto the pinhole which acts as the field diaphragm. This type of confocal setup discriminates all out-of-focus originating signals. Therefore only the light coming from the confocal focus volume in the sample enters the fibre guide to the ADP detector (SPCM-AQR-13-FC, EG&G, Canada). The more detailed description was given by Jankowski and Janka [105].

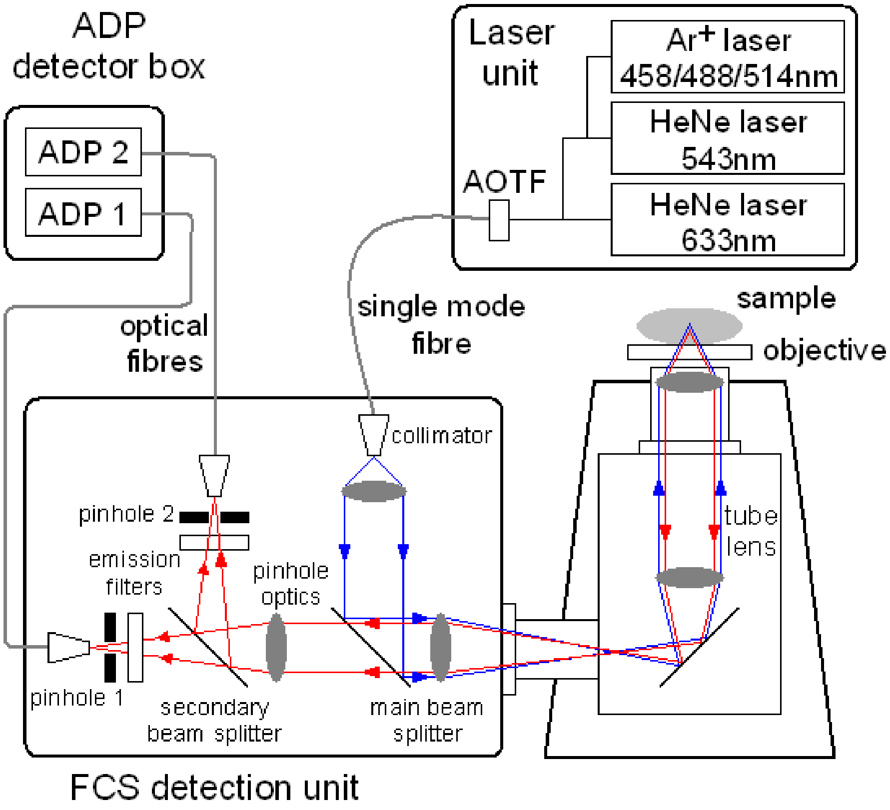

Fig.4.3. Schematic representation of the experimental setup for Fluorescence Correlation Spectroscopy – ConfoCor 2.

The sample was situated in the home-built temperature cell connected to the 330 Autotuning Temperature Controller (Lake Shore), which sets the temperature with accuracy of 0.05°C. The scheme of the temperature cell is shown in figure 4.4. Before starting any new measurement there was given at least 15min of a waiting time for the sample to equilibrate after each change of the temperature.

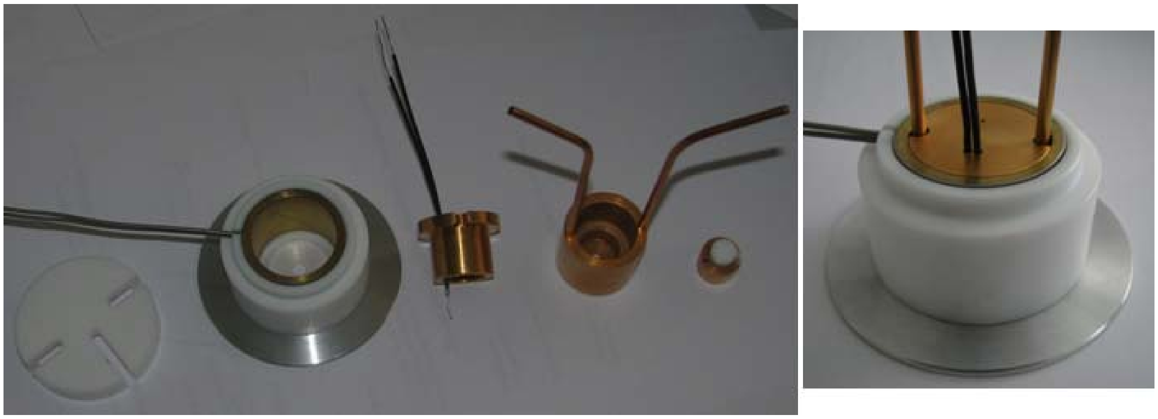

Fig.4.4. Temperature cell used in the FCS experiment.

4.3. Results and discussion

The data from FCS experiment were analyzed using a program written by Jacek Gapiński, FCS_fit, which allows fitting autocorrelation functions using Eq.4.7. A single decay fitting model was used (second amplitude, A2, was always set as 0), however, taking into account bleaching effect and presence of triplet state. The fixed parameters were structure parameter $SP = \frac{\omega_z}{\omega_{xy}}$ (set as 20) and base line (set as 1).

The reason to put such a high value for the structure parameter is that the 40x0.6 dry objective was used in the experiment. This objective was chosen because of its long working distance 3.65mm. An objective used in this experiment cannot approach the sample container due to the shape of the temperature cell and its isolating cover. On the other hand, using dry objectives for the observation of wet specimens has a disadvantage of aberrations due to the refractive index mismatch. This results in a focal shift between the nominal focal position (defined as the geometrical focus in a perfectly matched system) and the actual focal position. The difference between the refractive indices of the immersion and embedding media is larger than for other objectives, and that is why focusing even a few micrometers into the sample will also cause in a severe drop of intensity and resolution. This can be avoided by adjusting the correction collar [106].

In order to determine the size of the confocal volume (in other words, structure parameter) obtained using the 40x dry Olympus objective of (NA=0.6, WD=3.65mm), the model system, like for example rhodamine 6G dispersed in water, can be measured. Using standard water immersion C-Apochromat objective from Zeiss for investigation of water dispersions gives the structure parameter value of around 5. However, using a dry objective results in elongated shape of the confocal volume in *z*-axis direction due to aberrations caused by refractive index mismatch. The autocorrelation function of rhodamine 6G dispersed in water measured with this objective is given in figure 4.5.

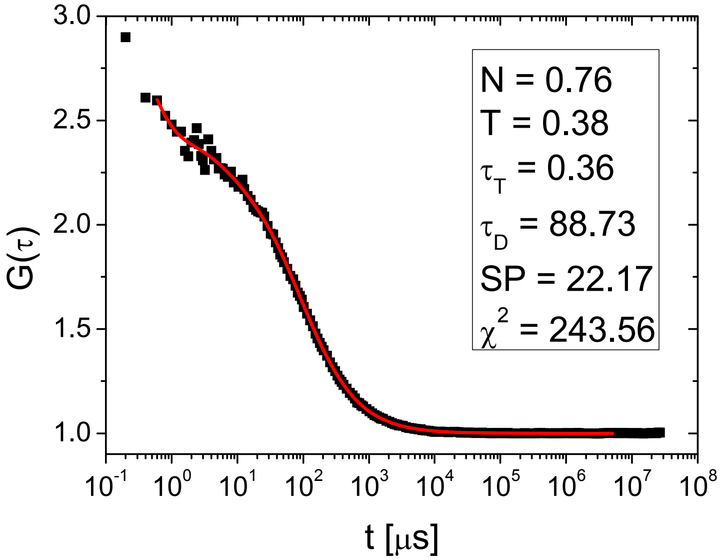

Fig.4.5. Exemplary autocorrelation function of Rhodamine 6G in water obtained from measurement, in which the 40x, NA=0.6 dry objective (Olympus) was used.

Red line represents fit of the autocorrelation function and the values of fitted parameters are given in the inset. It gave the value of SP around 20 and it will be used as a fixed parameter in fitting of the autocorrelation functions of the investigated system. Moreover, substituting Eq.4.6 to Eq.4.5:

$$\hat{G}(\tau) = 1 + \frac{1}{N}\left(1 + \frac{\tau}{\tau_D}\right)^{-1}\left(1 + \frac{\tau}{\tau_D}\left(\frac{\omega_{xy}}{\omega_z}\right)^2\right)^{-1/2} = \\ = 1 + \frac{1}{N}\left(1 + \frac{\tau}{\tau_D}\right)^{-1}\left(1 + \frac{\tau}{\tau_D} SP^{-2}\right)^{-1/2}, \qquad \text{(Eq.4.8.)}$$

shows that when structure parameter *SP* is large, the expression in the second bracket in Eq.4.8 goes to zero, but the diffusion time τ_D and therefore diffusion coefficient remains unchanged as long as the horizontal radius of the confocal volume ω_{xy} is not affected by aberrations due to the refractive index mismatch.

The exemplary autocorrelation functions of the rubrene in PEP solution with their fits (marked with red lines) obtained at three different temperatures: 40, 70 and 90°C are shown in figure 4.6.

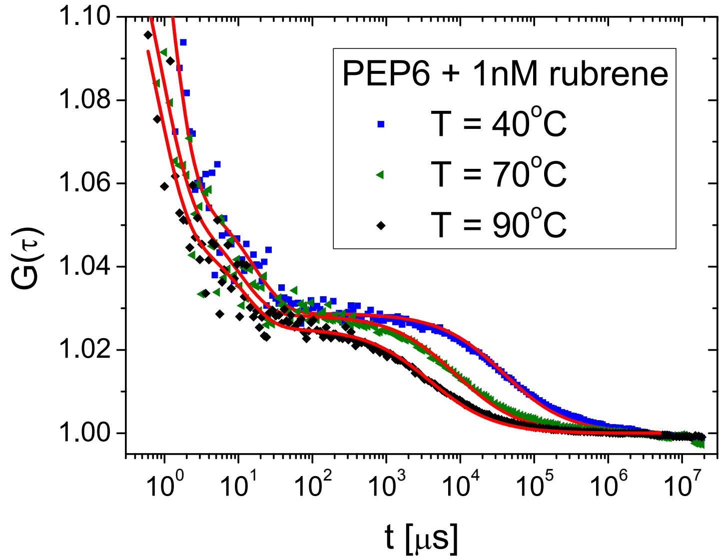

Fig.4.6. The exemplary autocorrelation functions from FCS obtained from measurements done at T=40°C, 70°C and 90°C with fits marked as red lines.

In this figure one can see the shift of the autocorrelation function decays to longer times while decreasing the temperature. This represents the slowing down in the motion of the rubrene particles in the suspension of PEP while cooling. Moreover, plotting the sample viscosity and diffusion times values versus temperature (see Fig.4.7) the same tendency (slope of the curves) can be observed. This simply means that the slowing down of the rubrene motion is solely due to the increase of the polymer viscosity while lowering temperature.

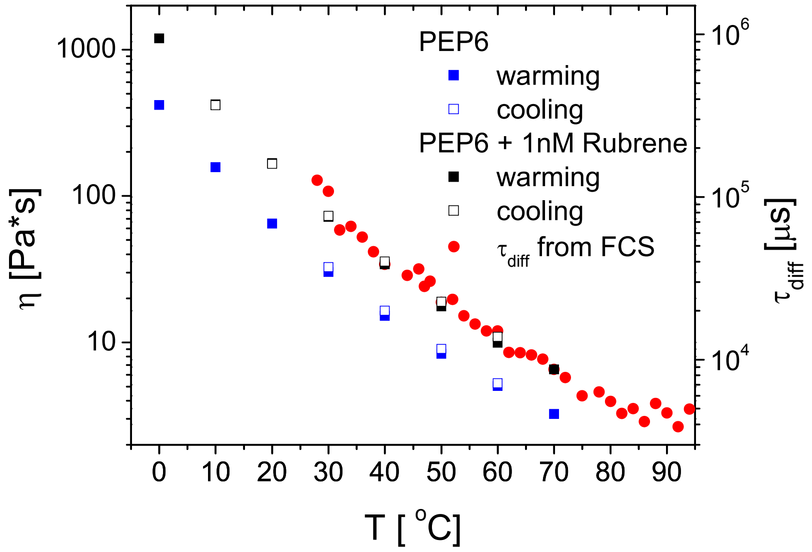

Fig.4.7. Results of the viscosity and the diffusion time measurements.

Further on, in figure 4.8 logarithm of the viscosities of: pure PEP6 (blue squares), 1nM rubrene in PEP6 solution (black squares) and logarithm of the diffusion time (red dots) versus temperature are plotted. For these curves fitting with the 2nd polynomial function $A+B_1\cdot T+B_2\cdot T^2$ (green lines) was done. This gives quantitative estimation of the slope of all of the curves.

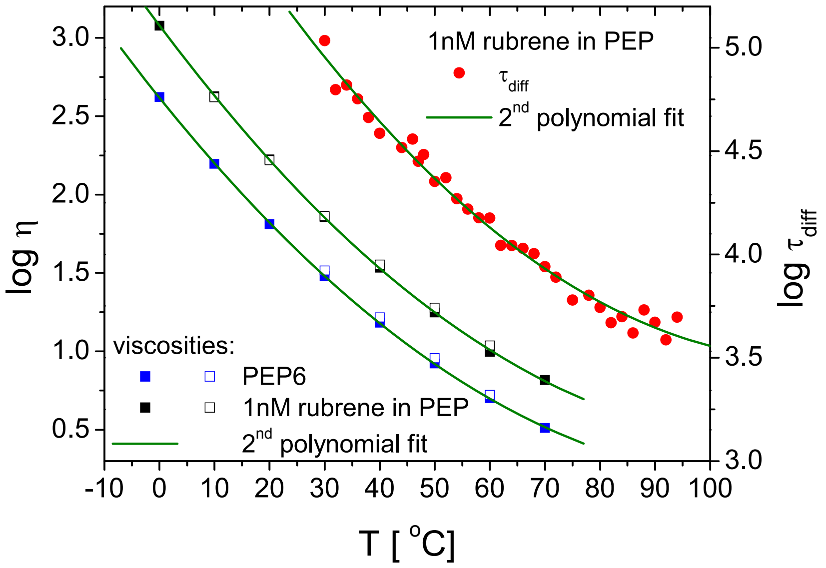

Fig.4.8. Logarithm of viscosities of pure PEP6 and 1nM rubrene in PEP6 and logarithm of diffusion time of rubrene in PEP6 versus temperature with their 2nd polynomial fits.

The obtained values of the 2nd polynomial function coefficients are summed up in the table 4.1. As it can be seen, the values of B_1 are around -0.044, and the values of B_2 are around $2 \cdot 10^{-4}$ for all of the curves, which is a proof of the same tendency in temperature behaviour of both, diffusion time of rubrene and the viscosity of PEP polymer.

Table 4.1. Coefficients from 2nd polynomial fit of temperature-dependent PEP6 and 1nM rubrene in PEP6 viscosity: $\eta(P)$=A+$B_1 \cdot T$+$B_2 \cdot T^2$. Coefficients from 2nd polynomial fit of temperature-dependent diffusion time of rubrene in PEP: τ_{diff} = A+$B_1 \cdot T$+$B_2 \cdot T^2$.

viscosity			
sample:	A $[Pa \cdot s]$	$B_1 \left[\frac{Pa \cdot s}{°C}\right]$	$B_2 \left[\frac{Pa \cdot s}{°C^2}\right]$
PEP6	2.61668	-0.0438	$1.96978 \cdot 10^{-4}$
1nM rubrene in PEP6	3.07794	-0.04706	$2.09242 \cdot 10^{-4}$
diffusion time			
sample:	A $[\mu s]$	$B_1 \left[\frac{\mu s}{°C}\right]$	$B_2 \left[\frac{\mu s}{°C^2}\right]$
1nM rubrene in PEP6	6.11511	-0.04431	$1.87349 \cdot 10^{-4}$

Additionally, the difference between the viscosity of the 1nM rubrene in PEP6 and the viscosity of the pure polymer was observed. This can be caused by the sample preparation procedure because the sample was held in vacuum conditions in order to remove toluene in which both components were dissolved primarily to distribute the dye uniformly in the polymer suspension. Probably the remains of solvents after polymerization process were also removed this way, and that causes higher viscosity of the PEP6 with rubrene solution than the polymer itself. Nevertheless, the tendency of increasing viscosity while decreasing temperature for both samples is the same: black and blue points, corresponding to viscosities of 1nM rubrene in PEP6 solution and pure PEP6, respectively, form curves of the same slope, which can be seen in Fig.4.7 and 4.8.

5.4. Conclusions and outlook

To conclude, the correlation between the temperature dependence of: the poly(ethylene-co-propylene) (PEP) macroscopic viscosity and the diffusion time of a nanoscopic probe represented by rubrene molecules diffusing between polymer chains was found. The macroscopic viscosities of pure polymer PEP and the investigated sample consisting of 1nM rubrene in PEP dispersion were determined by rheological measurement at zero shear viscosity conditions. The temperature-dependent values of diffusion time of rubrene were obtained from FCS measurement using the home-built temperature cell. Both quantities, polymer viscosity and rubrene diffusion time, show the same tendency with temperature (see Fig.4.8), which means that the temperature dependency of rubrene diffusion depends solely on macroscopic viscosity of the polymer, in which it is dissolved, as it was predicted based on findings of Holyst *et al.* [100].

Also the home-built temperature cell for FCS set up was tested here as well. It requires using long working distance dry objective due to the details of its construction and therefore the correction collar has to be properly adjusted in order to overcome the drop of intensity and resolution. Also the size of the confocal volume changes due to the refractive index mismatch and it has to be examined using a standard model sample (for example rhodamine) so that the proper value of the structure parameter will to be given in fitting of resulting autocorrelation functions.

The next step in future work could be use of the pressure cell designed for microscopy. This would be especially important in studies of systems for which increase of pressure correspond to increase of temperature (like for example described in previous part PEP-PEO polymeric micelles in water, which shrink while heating and under action of pressure). There is an upper limit in temperature range that can be set in the cell because it is placed near objective, which components (lenses) are glued and therefore it has to be protected from exposition to high temperatures. In order to avoid overheating of the cell surrounding, pressure can be used as a variable for such systems.

References:

[1] J. K. G. Dhont, G. Gomper "Introduction: Soft Matter", Lecture Notes from 39th IFF Spring School 2008

[2] D. Vlassopoulos, G. Fytas: From Polymers to Colloids: Engineering the Dynamic Properties of Hairy Particles, *Advances in Polymer Science* **236**, 1-54 (2010)

[3] C. N. Likos: Effective interactions in soft condensed matter physics; *Physics Report*s **348**, 267-439 (2001)

[4] H. Löwen: Melting, freezing and colloidal suspensions; *Physics Reports* **237**(5), 249-324 (1994)

[5] J. K. G. Dhont "An Introduction to Dynamics of Colloids", Elsevier Science B. V., Amsterdam 1996

[6] A. Vrij, J. W. Jansen, J. K. G. Dhont, C. Pathmamanoharan, M. M. Kops-Werkhoven, H. M. Fijnaut: Light-scattering of colloidal dispersions in non-polar solvents at finite-concentrations – silica spheres as model particles for hard-sphere interactions; *Faraday Discussions* **76**, 19-35 (1983)

[7] W. B. Russel, D. A. Saville, W. R. Schowalter "Colloidal Dispersions", Cambridge Univeristy Press, Cambridge 1992

[8] D. Frenkel: Soft condensed matter; *Physica A: Statistical Mechanics and its Applications* **313**(1-2), 1-31 (2002)

[9] J. F. Gohy: Block Copolymer Micelles; *Advances in Polymer Science* **190**, 65-136 (2005)

[10] R. O. Watts, D. Henderson, R. J. Baxter: Hard Spheres with Surface Adhesion: The Percus-Yevick Approximation and the Energy Equation; *Advances in Chemical Physics* **21**, 421-430 (1971)

[11] Y. C. Chiew, E. D. Glandt: Percolation behaviour of permeable and of adhesive spheres; *Journal of Physics A: Mathematical and General* **16**, 2599-2608 (1983)

[12] S. A. Safran, I. Webman, G. S. Grest: Percolation in interacting colloids; *Physical Review A* **32**(1), 506-511 (1985)

[13] N. A. Seaton, E. D. Glandt: Aggregation and percolation in a system of adhesive spheres; *Journal of Chemical Physics.* **86**(8), 4668-4677 (1986)

[14] W. G. T. Kranendonk, D. Frenkel: Simulation of the adhesive-hard-sphere model; *Molecular Physics* **64**(3), 403-424 (1988)

[15] N. A. M. Verhaegh, D. Asnaghi, H. N. W. Lekkerkerker, M. Giglio, L. Cipelletti: Transient gelation by spinodal decomposition in colloid-polymer mixtures; *Physica A* **242**, 104-118 (1997)

[16] M. A. Miller, D. Frenkel: Competition of Percolation and Phase Separation in a Fluid of Adhesive Hard Spheres; *Phys. Rev. Lett.* **90**(13), 135702 (2003); M. A. Miller, D. Frenkel: Phase diagram of the adhesive hard sphere fluid; *Journal of Chemical Physics* **121**(1), 535-545 (2004)

[17] R. Vavrin, J. Kohlbrecher, A. Wilk, M. Ratajczyk, M. P. Lettinga, J. Buitenhuis, G. Meier: Structure and phase diagram of an adhesive colloidal dispersion under high pressure: A small angle neutron scattering, diffusing wave spectroscopy, and light scattering study; *Journal of Chemical Physics* **130**, 154903 (2009)

[18] K. N. Pham, A. M. Purtas, J. Bergenholtz, S. U. Egelhaaf, A. Moussaïd, P. N. Pusey, A. B. Schofield, M. E. Cates, M. Fuchs, W. C. K. Poon: Multiple Glassy States in a Simple Model System; *Science* **296**, 104-106 (2002)

[19] F. Cardinaux, T. Gibaud, A. Stradner, P. Schurtenberger: Interplay between Spinodal Decomposition and Glass Formation in Proteins Exhibiting Short-Range Attractions; *Physical Review Letters* **99**, 118301 (2007)

[20] S. F. Edwards, K. E. Evans: Dynamics of highly entangled rod-like molecules; *Journal of the Chemical Society - Faraday Transactions II* **78**, 113-121 (1982)

[21] V. Trappe, V. Prasad, L. Cipelletti, P. N. Segrè, D. A. Weitz: Jamming phase diagram for attractive particles; Nature (London) **411**, 772-775 (2001)

[22] S. Roke, O. Berg, J. Buitenhuis, A. van Blaaderen, M. Bonn: Surface molecular view of colloidal gelation; *The Proceedings of the National Academy of Sciences U.S.A.* **103**(36), 13310-13314 (2006)

[23] S. Roke, J. Buitenhuis, J. C. van Miltenburg, M. Bonn, A. van Blaaderen: Interface-solvent effects during colloidal phase transitions; *Journal of Physics: Condensed Matter* **17**(45), S3469-S3479 (2005)

[24] R. J. Baxter: Percus-Yevick Equation for Hard Spheres with Surface Adhesion; *Journal of Chemical Physics* **49**(6), 2770-2774 (1968)

[25] C. Robertus, W. H. Philipse, J. G. H. Jootsen, Y. K. Levine: Solution of the Percus-Yevick approximation of the multicomponent adhesive spheres system applied to the small angle x-ray scattering from microemulsions, *Journal of Chemical Physics* **90**(8), 4482-4490 (1989)

[26] R. Fantoni, D. Gazzillo, A. Giacometti: Stability boundaries, percolation threshold, and two-phase coexistence for polydisperse fluids of adhesive colloidal particles; *Journal of Chemical Physics* **122**, 034901 (2005)

[27] H. Verduin, J. K. G. Dhont: Phase Diagram of a Model Adhesive Hard-Sphere Dispersion; *Journal of Colloid and Interface Science* **172**, 425-437 (1995)

[28] S. Buzzaccaro, R. Rusconi, R. Piazza: "Sticky" Hard Spheres: Equation of State, Phase Diagram, and Metastable Gels; *Physical Review Letters* **99**(9), 098301 (2007)

[29] P. J. Lu, E. Zaccarelli, F. Ciulla, A. B.Schofield, F. Sciortino, D. A. Weitz: Gelation of particles with short-range attraction; *Nature* **453**, 499-503 (2008)

[30] C. P. Royall, S. R. Williams, T. Ohtsuka, H. Tanaka: Direct observation of a local structural mechanism for dynamic arrest; *Nature materials* **7**, 556-561 (2008)

[31] H. E. Stanley "Phase Transitions and Critical Phenomena", Clarendon, Oxford, 1971

[32] W. Söber, A. Fink, E. Bohn: Controlled growth of monodisperse silica spheres in the micron size range; *Journal of Colloid and Interface Science* **26**(1), 62-69 (1968)

[33] A. van Blaaderen, A. Vrij: "Synthesis and Characterization of Colloidal Model Particles Made from Organoalkoxysilanes" in *The Colloid Chemistry of Silica*, Advances in Chemistry Series Vol. 234, edited by H. E. Bergna, American Chemical Society, Washington, DC, 1994

[34] A. K. van Helden, J. W. Jansen, A. Vrij: Preparation and characterization of spherical monodisperse silica dispersions in nonaqueous solvents; *Journal of Colloid and Interface Science* **81**(2), 354-368 (1981)

[35] J. Kohlbrecher, J. Buitenhuis, G. Meier, M. P. Lettinga: Colloidal dispersions of octadecyl grafted silica spheres in toluene: A global analysis of small angle neutron scattering contrast variation and concentration dependence measurements; *The Journal of Chemical Physics* **125**, 044715 (2006)

[36] D. J. Pine, chapter: "Light scattering and rheology of complex fluids driven far from equilibrium" in "Soft and fragile matter. Nonequlibrium Dynamics, Metastability and Flow" ed. M. E. Cates, M. R. Evans, 2000

[37] J. S. Higgins, H. C. Benoît, "Polymers and Neutron Scattering" Clarendon Press, Oxford 1994

[38] J. Kohlbrecher, W. Wagner: The new SANS instrument at the swiss spallation source sinq, *Journal of Applied Crystallography* **33**, 804-806 (2000)

[39] J. Kohlbrecher, A. Bollhalder, R. Vavrin, G. Meier: A high pressure cell for small angle neutron scattering up to 500MPa in combination with light scattering to investigate liquid samples; *Review of Scientific Instruments* **78**, 125101 (2007)

[40] U. Keiderling: The new 'BerSANS-PC' software for reduction and treatment of small angle neutron scattering data; *Applied Physics A: Materials Science and Processing* **74** [Suppl.], S1455-S1457 (2002)

[41] D. A. Weitz, D. J. Pine, chapter 16: "Diffusing-wave spectroscopy" in "Dynamic Light Scattering", pages 652-720, Oxford University Press, 1993

[42] S. Romer, F. Scheffold, P. Schurtenberger: Sol-Gel Transition of Concentrated Colloidal Suspensions; *Physical Review Letters*, **85**(23), 4980-4983 (2000)

[43] F. Scheffold, S. E. Skipetrov, S. Romer, P. Schurtenberger: Diffusing-wave spectroscopy of nonergodic media; *Physical Review E*, **63**(6), 061404 (2001)

[44] I. Daniel, P. Oger, R. Winter: Origins of life and biochemistry under high-pressure conditions; *Chemical Society Reviews*, **35**, 858-875 (2006)

[45] X. Chu, A. Faraone, C. Kim, E. Fratini, P. Baglioni, J. B. Leao, S. Chen: Proteins Remain Soft at Lower Temperatures under Pressure; *The Journal of Physical Chemistry B Letters*, **113**, 5001-5006 (2009)

[46] V. V. Mozhaev, K. Heremans, J. Frank, P. Masson, C. Balny: High Pressure Effects on Protein Structure and Function; *Proteins: Structure, Function, and Genetics* **24**(1), 81-91 (1996)

[47] K. Heremans, L. Smeller: Protein structure and dynamics at high pressure; *Biochimica et Biophysica Acta* **1386**, 353-370 (1998)

[48] B. B. Boonyaratanakornkit, C. B. Park, S. D. Clark: Pressure effects on intra- and intermolecular interactions within proteins; *Biochimica et Biophysica Acta* **1595**, 235-249 (2002)

[49] S. H. Cheng, *CRC Handbook of Lubrication*; E. R. Booser (Ed.); CRC Press: Boca Raton, FL, Vol. II, 139 (1984)

[50] P. L. Bondor, G. J. Hirasaki, M. J. Tham: Mathematical simulation of polymer flooding in complex reservoirs; *Society of Petroleum Engineers Journal* **12**(5), 369 (1972); G. Chauveteau: Fundamental Criteria in Polymer Flow Through Porous Media; *Advances in Chemistry* **213**, Chapter 14, 227-267 (1986)

[51] G. N. Malcolm, J. S. Rowlinson: The Thermodynamic Properties of Aqueous Solutions of Polyethylene Glycol, Polypropylene Glycol and Dioxane; *Transactions of the Farady Society* **53**, 921-931 (1957)

[52] S. Saeki, N. Kuwahara, M. Nakata, M. Kaneko: Upper and lower critical solution temperatures in poly(ethylene glycol) solutions; *Polymer* **17**, 685-689 (1976)

[53] Y. C. Bae, S. M. Lambert, D. S. Soane, J. M. Prausnitz: Cloud-Point Curves of Polymer Solutions from Thermooptical Measurements; *Macromolecules* **24**, 4403-4407 (1991)

[54] Y. C. Bae, J. J. Shim, D. S. Soane, J. M. Prausnitz: Representation of Vapour-Liquid and Liquid-Liquid Equilibria for Binary Systems Containing Polymers: Applicability of an Extended Flory-Huggins Equation; *Journal of Applied Polymer Science* **47**, 1193-1206 (1993)

[55] R. L. Cook, H. E. King, Jr., Dennis G. Peiffer: Pressure-Induced Crossover from Good to Poor Solvent Behavior for Polyethylene Oxide in Water; *Physical Review Letters* **69**(21), 3072-3075 (1992)

[56] T. Sun, H. E. King, Jr.: Discovery and Modeling of Upper Critical Solution Behavior in the Poly(ethylene oxide)/Water Systems at Elevated Pressure; *Macromolecules* **31**, 6383-6386 (1998)

[57] B. Hammouda, D. Ho, S. Kline: SANS from Poly(ethylene oxide)/Water Systems; *Macromolecules* **35**, 8578-8585 (2002)

[58] A. Matsuyama, F. Tanaka: Theory of Solvation-Induced Reentrant Phase Separation in Polymer Solutions; *Physical Review Letters* **65**(3), 341-344 (1990)

[59] S. Bekiranov, R. Bruinsma, P. Pincus: Solution behavior of polyethylene oxide in water as a function of temperature and pressure; *Physical Review E* **55**(1), 577-585 (1997)

[60] H. S. Ashbaugh, M. E. Paulaitis: Monomer Hydrophobicity as a Mechanism for the LCST Behavior of Poly(ethylene oxide) in Water; *Industrial & Engineering Chemistry Research* **45**, 5531-5537 (2006)

[61] Molyneux, P. (ed.): *Water-Soluble Synthetic Polymers: Properties and Uses*; CRC Press, Boca Raton 1983

[62] C. R. Cox, E. H. Dunlop, A. M. North: Role of molecular aggregates in liquid drag reduction by polymers; *Nature* **249**, 243-245 (1974)

[63] G. E. Gadd: Effects of Drag-reducing Additives on Vortex Stretching; *Nature* **217**, 1040-1042 (1968)

[64] J. A. de Witt, T. G. M. van de Ven: The effect of neutral polymers and electrolyte on the stability of aqueous polystyrene latex; *Advances in Colloid Interface Science* **42**, 41-64 (1992)

[65] D. H. Napper: Steric stabilization; *Journal of Colloid and Interface Science* **58**(2), 390-407 (1977)

[66] Th. F. Tadros, B. Vincent: The influence of electrolytes on the adsorption of poly(vinyl alcohol) on polystyrene particles and on the stability of the polymer-coated particles; *Journal of Colloid and Interface Science* **72**(3), 505-514 (1979)

[67] Y. Layec, M-N. Layec Raphalen: Instability of dilute poly(ethylene-oxide) solutions; *Journal de Physique Lettres* **44**(3), L121-L128 (1983)

[68] N. S. Berman: Drag Reduction by Polymers; *Annual Review of Fluid Mechanics* **10**, 47-64 (1978)

[69] M. J. Schick (ed.), *Nonionic Surfactants*; Marcel Dekker, New York, 1967

[70] S. Zaplinsky, J. M. Harris: Introduction to Chemistry and Biological Applications of Poly(ethylene glycol); *ACS Symposium Series* **680**, 1-13 (1997)

[71] J. H. Lee, B. H. Lee, J. D. Andrade: Blood Compatibility of Polyethylene Oxide Surfaces; *Progress in Polymer Science* **20**(6), 1043-1079 (1995)

[72] C. Allen, D. Maysinger, A. Eisenberg: Nano-engineering block copolymer aggregates for drug delivery; *Colloids and Surfaces B* **16**, 3-27 (1999); G. S. Kwon, T.

Okano: Polymeric micelles as new drug carriers; *Advanced Drug Delivery Review* **21**(2), 107-116 (1996)

[73] R. Lund, L. Willner, J. Stellbrink, A. Radulescu, D. Richter: Role of Interfacial Tension for the Structure of PEP-PEO Polymeric Micelles. A Combined SANS and Pendant Drop Tensiometry Investigation; *Macromolecules* **37**, 9984-9993 (2004)

[74] A. Poppe, L. Willner, J. Allgaier, J. Stellbrink, D. Richter: Structural Investigation of Micelles Formed by an Amphiphilic PEP-PEO Block Copolymer in Water; *Macromolecules* **30**, 7462-7471 (1997)

[75] R. L. Cook, H. E. King Jr., D. Peiffer: High-Pressure Viscosity of Dilute Polymer Solutions in Good Solvents; *Macromolecules* **25**, 2928-2934 (1992)

[76] P. L. Fox, A. L. Kelly "The caseins" in *Proteins in food processing*, edited by R. Y. Yada, Woodhead Publishing Limited and CRC Press LLC, Cambridge, Boca Raton, 2004

[77] N. Osaka, M. Shibayama: Pressure-Induced Phase Transitions of Hydrophobically Solvated Block-Copolymer Solutions; *Physical Review Letters* **96**, 048303 (2006); N. Osaka, S. Okabe, T. Karino, Y. Hirabaru, S. Aoshima, M. Shibayama: Micro- and macrophase separations of hydrophobically solvated block copolymer aqueous solutions induced by pressure and temperature; *Macromolecules* **39**(17), 5875-5884 (2006); N. Osaka, S. Miyazaki, S. Okabe, H. Endo, A. Sasai, K. Seno, S. Aoshima: Pressure-induced reentrant micellization of amphiphilic block copolymers in dilute aqueous solutions; *Journal of Chemical Physics* **127**(9), 094905

[78] D. Y. Ryu, D. J. Lee, J. K. Kim, K. A. Lavery, T. P. Russell, Y. S. Han, B. S. Seong, C. H. Lee: Effect of Hydrostatic Pressure on Closed-Loop Phase Behavior of Block Copolymers; *Physical Review Letters* **90**(23), 235501 (2003)

[79] J. Allgaier, A. Poppe, L. Willner, D. Richter: Synthesis and Characterization of Poly[1,4-isoprene-*b*-(ethylene oxide)] and Poly[ethylene-*co*-propylene-*b*-(ethylene oxide)] Block Copolymers; *Macromolecules* **30**, 1582-1586 (1997)

[80] K. Devanand, J. C. Selser: Asymptotic Behavior and Long-Range Interactions in Aqueous Solutions of Poly(ethylene oxide); *Macromolecules* **24**, 5943-5947 (1991)

[81] A. Poppe: Selbstassozation amphiphiler Blockcopolymere in Wasser: Strukturuntersuchungen und Untersuchungen zur Kinetik der Mizellbildung; PhD Thesis 1998

[82] K. Vedam, P. Limsuwan: Piezo- and elasto-optic properties of liquids under high pressure. II. Refractive index vs density; *Journal of Chemical Physics* **69**(11), 4772-4778 (1978)

[83] G. Meier, R. Vavrin, J. Kohlbrecher, J. Buitenhuis, M. P. Lettinga, M. Ratajczyk: SANS and dynamic light scattering to investigate the viscosity of toluene under high pressure up to 1800 bar; *Measurement Science and Technology* **19**, 034017 (2008)

[84] R. T. Emmet, F. J. Millero: Specific Volume of Deuterium Oxide from 2º to 40ºC and 0 to 1000 Bars Applied Pressure; *Journal of Chemical and Engineering Data*, **20**(4), 351-356 (1975)

[85] Y. Lee, J. Jonas: Density Effects on the Dynamic Structure of Liquid Deuterium Oxide; *Journal of Chemical Physics* **57**(10), 4233-4240 (1972)

[86] N. Matsunaga, A. Nagashima: Transport Properties of Liquid and Gaseous D_2O over a Wide Range of Temperature and Pressure; *Journal of Physical and Chemical Reference Data* **12**(4), 933-962 (1983)

[87] G. I. Egorov, A. M. Kolker: Effect of pressure and temperature on volume properties of water-N,N-dimethylformamide mixtures; *Journal of Molecular Liquids* **106**, 239-248 (2003)

[88] G. I. Egorov, A.A. Syrbu, A. M. Kolker: p-V_m-x Properties of Water-Dimethylformamide System at 288.15 K over the Pressure Range 0.1-100MPa; *Russian Journal of General Chemistry* **73**(7), 1016-1020 (2003)

[89] D. J. Pine "Light scattering and rheology of complex fluids driven far from equilibrium" in *Soft and Fragile Matter. Nonequilibrium Dynamics, Metastability and Flow*, Scottish Universities Summer School in Physics and Institute of Physcis Publishing, edited by M. E. Cates, M. R. Evans, Bristol and Philadelphia, 2000

[90] G. Meier, H. Kriegs: A high pressure cell for dynamic light scattering up to 2kbars with conservation of plane of polarization; *Review of Scientific Instruments* **79**, 013102 (2008)

[91] J. S. Higgins, C. Benoît "Polymers and Neutron Scattering", Oxford University Press, Oxford, 1996

[92] G. Beaucage: Approximations Leading to a Unified Exponential/Power-Law Approach to Small-Angle Scattering; *Journal of Applied Crystallography* **28**, 717-728 (1995)

[93] M. Daoud, J. P. Cotton: Star shaped polymers: a model for the conformation and its concentration dependence; *Journal de Physique* **43**(3), 531 (1982)

[94] A. Halperin: Polymeric Micelles: A Star Model; *Macromolecules* **20**(11), 2943-2946 (1987)

[95] M. D. Lechner, K. Gehrke, E. H. Nordmeier "Makromolekulare Chemie. Ein Lehrbuch für Chemiker, Physiker, Materialwissenschaftler und Verfahrenstechniker", Basel 1993

[96] C. Branca, A. Faraone, S. Magazù, G. Maisano, P. Migliardo, A. Triolo, R. Triolo, V. Villari: Anomalous conformational properties of PEO in H_2O and D_2O by SANS, PCS and Raman scattering; *Journal of Applied Crystallography* **33**, 709-713 (2000)

[97] L. Willner, A. Poppe, J. Allgaier, M. Monkenbusch, P. Lindner, D. Richter: Micellization of amphiphilic diblock copolymers: Corona shape and mean-field to scaling crossover; *Europhysics Letters* **51**(6), 628-634 (2000)

[98] L.Willner, A. Poppe, J. Allgaier, M. Monkenbusch, D. Richter: Time-resolved SANS for the determinationof unimer exchange kinetics in block copolymer micelles; *Europhysics Letters* **55**(5), 667-673 (2001)

[99] R. Lund, L. Willner, D. Richter, E. E. Dormidontova: Equilibrium Chain Exchange Kinetics of Diblock Copolymer Micelles: Tuning and Logarithmic Relaxation; *Macromolecules* **39**, 4566-4575 (2006)

[100] R. Holyst, A. Bielejewska, J. Szymański, A. Wilk, A. Patkowski, J. Gapiński, A. Żywociński, T. Kalwarczyk, E. Kalwarczyk, M. Tabaka, N. Ziębacz, S. A. Wieczorek: Scaling from viscosity at all length-scales in poly(ethylene glycol) solutions studied by fluorescence correlation spectroscopy and capillary electrophoresis; *Physical Chemistry Chemical Physics* **11**, 9025-9032 (2009)

[101] http://en.wikipedia.org/wiki/Rubrene

[102] F. Bayrakçeken: A new type of delayed fluorescence of rubrene in solution; *Journal of Luminnescence* **54**, 29-33 (1992)

[103] S. R. Aragón, R. Pecora: Fluorescence Correlation Spectroscopy and Brownian Rotational Diffusion; *Biopolymers* **14**(1), 119-138 (1975)

[104] J. Widengren, Ü. Mets, R. Rigler: Fluorescence Correlation Spectroscopy of Triplet States in Solution: A Theoretical and Experimental Study; *Journal of Physical Chemistry* **99**(36), 13368-13379 (1995)

[105] T. Jankowski, R. Janka: ConfoCor2 – The Second Generation of Fluorescence Correlation Microscopes; in R. Rigler, E.S. Elson: Fluorescence Correlation Spectroscopy, Theory and Applications, Wiley 2000

[106] A. Egner, S. W. Hell: “Abberations in confocal and multi-photon fluorescence microscopy induced by refractive index mismatch” in “Handbook of biological confocal microscopy”, James B. Pawley (editor), Springer Science+Business Media, LLC, New York, 2006

Acknowledgements

First and foremost I would like to thank Jan Dhont for all his courage, support, patience and help during my stay in Forschungszentrum Jülich, and for accepting to referee this thesis.

I would like to acknowledge the extended independence granted to me by my supervisor, Gerd Meier. Sincere thanks to you and Pavlik Lettinga for proof-reading my thesis. I would like to express my special gratitude to Pavlik for encouraging and supporting me.

Also, I would like to give my acknowledgement to Prof. Stefan Egelhaaf for accepting to review my thesis.

I would like to express my thanks to my colleagues from work, especially my office-mates, for their nice companion that I enjoyed a lot.

Last but not least, I would like to thank my family, Lejdis and friends for being always there for me.

Die hier vorgelegte Dissertation habe ich eigenständig und ohne unerlaubte Hilfe angefertigt. Die Dissertation wurde in der vorgelegten oder in ähnlicher Form noch bei keiner anderen Institution eingereicht. Ich habe bisher keine erfolglosen Promotionsversuche unternommen.

Düsseldorf, den 18.05.2011

Karolina Tomczyk